uOttawa

L'Université canadienne
Canada's university

FACULTÉ DES ÉTUDES SUPÉRIEURES ET POSTOCTORALES

uOttawa
L'Université canadienne
Canada's university

FACULTY OF GRADUATE AND POSDOCTORAL STUDIES

Ahmad Al-Jarrah
AUTEUR DE LA THÈSE / AUTHOR OF THESIS

Ph.D. (Mechanical Engineering)
GRADE / DEGREE

Department of Mechanical Engineering
FACULTÉ, ÉCOLE, DÉPARTEMENT / FACULTY, SCHOOL, DEPARTMENT

A Novel Energy Based Design Methodology of Sliding Mode Controllers for Tracked Autonomous Guided Vehicles

TITRE DE LA THÈSE / TITLE OF THESIS

Atef Fahim
DIRECTEUR (DIRECTRICE) DE LA THÈSE / THESIS SUPERVISOR

CO-DIRECTEUR (CO-DIRECTRICE) DE LA THÈSE / THESIS CO-SUPERVISOR

EXAMINATEURS (EXAMINATRICES) DE LA THÈSE / THESIS EXAMINERS

N. Baddour	J. Sasiadek
F. Karray (absent)	
P. Payeur	

Gary W. Slater
Le Doyen de la Faculté des études supérieures et postdoctorales / Dean of the Faculty of Graduate and Postdoctoral Studies

A Novel Energy Based Design Methodology of Sliding Mode Controllers for Tracked Autonomous Guided Vehicles

By

Ahmad Mohammad Al-Jarrah

A thesis submitted to the Faculty of Graduate and Postdoctoral studies in partial fulfilment of the requirements for the degree of

Doctoral of Philosophy

in Mechanical Engineering

Ottawa-Carleton Institute for Mechanical and Aerospace Engineering
University of Ottawa
Ottawa, Canada

Library and
Archives Canada

Published Heritage
Branch

395 Wellington Street
Ottawa ON K1A 0N4
Canada

Bibliothèque et
Archives Canada

Direction du
Patrimoine de l'édition

395, rue Wellington
Ottawa ON K1A 0N4
Canada

Your file Votre référence
ISBN: 978-0-494-34119-3
Our file Notre référence
ISBN: 978-0-494-34119-3

NOTICE:
The author has granted a non-exclusive license allowing Library and Archives Canada to reproduce, publish, archive, preserve, conserve, communicate to the public by telecommunication or on the Internet, loan, distribute and sell theses worldwide, for commercial or non-commercial purposes, in microform, paper, electronic and/or any other formats.

The author retains copyright ownership and moral rights in this thesis. Neither the thesis nor substantial extracts from it may be printed or otherwise reproduced without the author's permission.

AVIS:
L'auteur a accordé une licence non exclusive permettant à la Bibliothèque et Archives Canada de reproduire, publier, archiver, sauvegarder, conserver, transmettre au public par télécommunication ou par l'Internet, prêter, distribuer et vendre des thèses partout dans le monde, à des fins commerciales ou autres, sur support microforme, papier, électronique et/ou autres formats.

L'auteur conserve la propriété du droit d'auteur et des droits moraux qui protège cette thèse. Ni la thèse ni des extraits substantiels de celle-ci ne doivent être imprimés ou autrement reproduits sans son autorisation.

In compliance with the Canadian Privacy Act some supporting forms may have been removed from this thesis.

While these forms may be included in the document page count, their removal does not represent any loss of content from the thesis.

Conformément à la loi canadienne sur la protection de la vie privée, quelques formulaires secondaires ont été enlevés de cette thèse.

Bien que ces formulaires aient inclus dans la pagination, il n'y aura aucun contenu manquant.

Canada

Abstract

Tracked Autonomous Guided Vehicles (TAGVs) are becoming an important tool for surveillance and security operations so as to mitigate harm to human who otherwise have to conduct such operations. To accomplish steering of such tracked vehicles, skid steering is used. This entails varying the speed of the individual tracks to impose a turning moment on the vehicle. In skid steering, the interaction between the tracks and the terrain is in the form of slippage and soil shearing during the process of turning. These phenomena of slippage and soil shearing are highly nonlinear and difficult to quantify. As such they result in inaccurate kinematics/dynamics of the vehicle. Achieving good path tracking performance of the vehicle in the presence of such inaccuracies requires a robust controller design.

Sliding mode Controllers (SMCs) are insensitive to system parameter uncertainties, modeling errors, and disturbances. Such controllers are considered to be robust. Consequently, they have been proposed as the proper choice for this work. One of the major drawbacks of the published approaches of designing SMCs is the need to assume the values of some of the controller parameters. In this thesis, a novel design methodology of SMCs is developed based on the system total energy. This approach provides a relationship between the SMC parameters and some limits on these parameters. However, the choice of the value of these parameters is still wide enough such that the approach of sensitivity analysis is carried out to tighten these limits. Using SMCs result in undesirable chattering. To reduce or eliminate chattering, the boundary layer technique is employed.

The new design methodology of the SMC is exemplified first on a DC motor model where the model is a Single-Input-Single-Output (SISO) system. Since the TAGV is a special case of a Multi-Input-Multi-Output (MIMO) system, an extension of the new SMC approach is developed. Inverted pendulum systems are popular examples in many control text because of the many practical applications they can model, particularly in the field of robotics. The inverted pendulum is a Single-Input-Multi-Output (SIMO) system similar to the TAGV, and is selected to test the new approach. SMC with hyper sliding surface is also introduced. Simulation results of the motor and pendulum show very good performance of the SMC especially when it is compared to that of proportional and proportional-derivative controllers.

Simulation results of the TAGV using SMCs both decoupled and hyper sliding surfaces based on the proposed design methodology show very good performance when compared to that of proportional controllers.

Acknowledgments

I would like to express my sincere appreciation and deepest gratitude to my supervisor Professor Atef Fahim for his guidance, encouragement and continuous support throughout the course of this research.

The financial support granted by the Hashemite University, Jordan, is gratefully acknowledged.

I am also indebted to my friends Cagri Ayranji, Ali Abbas, Dave Roussel, Ahsan Ahmad, Majdi Rawashdeh, Samer Samara and Seddeg Alsari for their moral support.

I would like also to thank my parents, Mohammad and Nawal, my brothers, Hamzeh and Ali, and sisters, Nazik and Batool, for their consistent patience and prayers. Special thanks are extended to my father-in-law, Dr. Ali Diabi, and to my mother-in-law, Wardah Badawi, for their unlimited support and prayers. The support of my brothers-in-law, Mohamed Cherif and Abdelfettah, and my sister-in-law, Amira, is highly appreciated. I must also forward a very special thanks to my dearest wife Zineb who patiently endured my hard work and gave me her support for the last two years. The smiles of my daughter Bayan must also be recognized since it gave me the inspiration to finish this work successfully.

Finally, above all, I must thank almighty Allah for making this work possible.

Table of Contents

List of Figures

List of Tables

Chapter 1

Introduction

1.1 Motivation

Mobile robots or vehicles have a broad set of applications. They can be used for manufacturing or assembly operations, food and medication transport throughout hospitals, or even autonomous cleaning vehicles. A mobile robot intended task influences to a large extent the selection of the robot's method of locomotion and is an important aspect of the mobile robot design. Mobile robot's locomotion mechanisms must be selected in a way to enable the robot to move easily throughout its work environment.

There are a large variety of possible ways for the robot to move. Mobile robots generally locomote either using rolling mechanisms, a well known technology for vehicles, or using a small number of articulated legs, the simplest of the biological approaches to locomotion. Mobile robots equipped with tracks instead of wheels are called tracked vehicles. Locomotion based on tracks is a good selection for applications where terrain conditions are difficult or unpredictable. Tracked vehicles have larger ground contact patches which improve significantly their maneuverability on loose terrain compared to conventional wheeled vehicles. A large contact area provides better traction on all types of surfaces. Hence, tracked vehicles are widely used in industries such as forestry, agricultural, mining and planetary exploration. They are also used in military vehicles (tanks and armed vehicles) where navigation over very rough terrain is required.

In the last few years, tracked mobile robots have been receiving a great deal of attention from researchers. This attention is directly related to the recent demand for increase security, surveillance, and bomb-disposal. A typical example of these mobile robots is the Vanguard robot. Some specifications of the Vanguard are listed in Chapter 3. The Vanguard can be used indoors and outdoors for security, surveillance, and bomb disposal purposes. It is designed as a teleoperated machine with a remote laptop computer-based command and a control unit to control motion and the robotic arm on top of the robot. A command is given to the robot by the unit to move the robot towards the desired position by the use of a joystick or directional keys. However, it is realized that the Vanguard is unable to execute any surveillance job autonomously. Hence, the idea of the proposed research of controlling a tracked autonomous guided vehicle is being developed.

1.2 Objective

The most common configuration of tracked mobile robots is that of a robot equipped with two tracks on each side of the vehicle. While for wheeled vehicles steering can be simply accomplished by making the aft or rear wheels steerable, this approach can not work for tracked vehicles. Another less employed approach for steering wheeled vehicles is that of differential steering. In this approach the wheel speeds on either side of the vehicle are precisely varied so as to impose a turning moment on the vehicle and hence steer it in the desired direction. This approach, commonly used for tracked vehicles, is referred to as skid steering. The steering of a tracked vehicle using this approach is achieved by individually varying the thrust of the tracks. Consequently, a turning moment is created to overcome the moment of turning resistance due to skidding of the tracks on the ground and the rotational inertia of the vehicle. In other words, the skid steering approach is based on varying the relative velocities of the two tracks, which in turn will result in slippage and soil shearing in order to achieve the steering. These phenomena of slippage and soil shearing are highly nonlinear and difficult to reliably quantify, and cause inaccurate tracked vehicle kinematics and dynamics. The problem is further aggravated by the fact that as the vehicle navigates over differing terrain the magnitude of these nonlinear quantities vary significantly. Within a navigational mission for a surveillance vehicle the changes tend to be rapid and frequent. These inaccuracies make it difficult to predict the exact motion of the tracked vehicles and increase the complexity of the task of controlling their motion. Controlling the motion of a tracked vehicle in the presence of such inaccuracies requires a robust control system that can deal with the magnitude and frequency of change of these inaccuracies.

While the main objective of this work is to contribute to the fundamental understanding of the dynamics, kinematics and motion control of a tracked autonomous guided vehicle where skid steering is used, the control aspect took on a disproportionate attention for two reasons. The first was the necessity of finding a robust and accurate controller to deal with the problem of rapidly and drastically varying track/ground interaction. The second was that once the type of controller was identified, a variable structure controller (sliding mode controller), it was discovered that the design process of this type of controller seemed to be ad-hoc and not methodically carried out.

In spite of the difficulties of skid steering mentioned earlier, a kinematic/dynamic model can be developed and used in a control system to precisely control the motion of the vehicle. The effects of skid steering, lateral and longitudinal load transfer are taken into account while deriving the dynamic equations of the vehicle.

A navigational system based on computer vision is proposed in this work to guide the vehicle along a marked path. The navigational system includes a path planning module to guide the robot between the current and the desired poses, and a controller module to cause the robot to move along the path. Previous work on controller designs of such systems is generally based on the system kinematic models. However, recently controller designs based on the vehicle dynamics have been investigated.

A variable structure controller is used here to improve the robustness of the system in the presence of uncertainties, modeling errors, and disturbances. Since there is no well defined procedure reported in the literature to design variable structure controllers, a new design methodology of variable structure controllers is developed in this thesis. The design procedure is based on system energy. The design methodology is developed and exemplified on a DC motor model first. The motor example is that of a Single-Input-Single-Output (SISO) system whereas the tracked vehicle control system is a Single-Input-Multi-Output (SIMO) system. Consequently, the design methodology is extended so as to deal with SIMO systems. An inverted pendulum system is then selected to test the new design methodology since it is a SIMO boundary stable nonlinear system. The system is also acknowledged to be a difficult one to control because it is boundary stable and can tend towards instability rapidly. Furthermore, it has been dealt with extensively in the literature. For comparison purposes, proportional and proportional-derivative controllers are applied to the DC motor, the inverted pendulum, and the tracked vehicle systems. The advantages of variable structure controllers over the other types are shown through the simulation results.

Applying the new design methodology of variable structure controllers to the motor and the pendulum systems is carried out for theoretical reasons. However, it should be noted that the use of variable structure controllers results in undesirable chattering. Since the purpose of the new design approach is to implement it on a real tracked vehicle, chattering should be eliminated. Hence, the boundary layer technique is used.

1.3 Thesis Outline

This thesis consists of seven chapters. The first, an introduction, provides a general idea of tracked mobile robots and the motivation for the work. The structure of the thesis is as follows:

A literature review dealing with the kinematics, dynamics and control of mobile robots, especially tracked mobile robots, is presented in Chapter 2. The chapter also includes a literature survey on path planning techniques of mobile robots. Since variable structure controllers are used in this work, an extended review of the literature dealing with this type of controller is also presented. Chattering phenomenon is a common problem of variable structure controllers, consequently a section is dedicated to a survey of literature aimed at of minimizing chattering.

Chapter 3 deals with the kinematics and dynamics modeling of mobile robots. The chapter starts by deriving the kinematics of wheeled mobile robots. Wheeled mobile robots can be differentially steered similar to tracked vehicles. Issues of skid steering kinematics of tracked vehicles are then discussed. Tracked vehicle dynamics resulting from skid steering are then presented. Since the tracked vehicle used as a model in this thesis is powered by permanent magnet DC motors, a full model of such motors is included in the chapter. The chapter ends by presenting the proposed navigational system for use with this Tracked Autonomous Guided Vehicle (TAGV).

A new approach for designing variable structure controllers (sometimes called sliding mode controllers) is presented in Chapter 4. The chapter starts with an introduction to variable structure controllers and different approaches that have been proposed for their design. An energy based design procedure for Sliding Mode Controllers (SMCs) is derived in detail in this chapter. The design approach is exemplified on a DC motor. This example is particularly useful since this type of motor is used as a prime mover for the TAGV. Simulation results for controlling the DC motor are also presented in this chapter.

Since the TAGV is a special case of Multi-Input-Multi-Output (MIMO) control systems, an extension of the proposed SMC design approach is presented in Chapter 5. The design approach is tested on an inverted pendulum system. Simulation results for the SMC designed using the proposed approach controlling the inverted pendulum are then presented. Different controller schemes are also tested and compared through simulation results.

Chapter 6 starts by presenting the navigational system used to control the path tracking action of the TAGV. The application of the proposed design approach of SMCs for SIMO systems on the TAGV is explained in this chapter. Simulation results including path tracking performance of the TAGV while controlled by different controller schemes are then presented. The results are shown for different operating conditions.

Chapter 7 concludes with a summary and general discussion of the results and main contributions of this work. An outline of some recommendations for future research is also presented.

Chapter 2

Literature Survey

2.1 Introduction

The area of TAGVs is multi-disciplinary. It includes technologies from different disciplines such as mechanical engineering, electrical engineering, computer science and artificial intelligence. For mechanical engineering, research and studies were carried out primarily on the dynamics and kinematics of the tracked vehicles and on the design of a suitable controller to follow a desired path. In this chapter, the literature survey is divided into three parts. The first deals with modeling issues of the TAGVs, and includes the formulation of the kinematics and dynamics of the TAGVs. In the second part, several path planning techniques for the TAGVs are presented. Finally the third part deals with path-following controller designs of TAGVs. In this part, the sliding mode controllers will be studied in depth.

2.2 TAGV Kinematics

Reported literature on autonomous tracked vehicles [1] shows that their kinematic and dynamic models are similar to those of tracked vehicles. Both have special features distinguishing them from regular vehicles, namely; the steering mechanism and the terramechanics. Due to limited availability of literature on these aspects of TAGV mechanics and terramechanics, literature on the general category of tracked vehicle will be reviewed. Wong [2] developed a theoretical background of the mechanics of vehicle-terrain interaction-terramechanics as well as the modeling and steering of tracked vehicles. Wong proposed two approaches to steering; the articulated steering and the skid steering approaches. The articulated steering approach is primarily used for vehicles consisting of two or more units or segments. The steering is accomplished by forcing one unit to rotate with respect to the other to make the vehicle follow a predefined path. The skid steering approach is for vehicles consisting of a single unit. The latter approach is the more popular and is widely used for tracked vehicles since it is simpler and has a faster response [1]. In this approach, the steering of the tracked vehicle is achieved by individually varying the thrust of the tracks. Consequently, a turning moment is created to overcome the moment of turning resistance due to skidding of the tracks on the ground and the rotational inertia of the vehicle in yaw. In other words, skid steering is based on varying the relative velocities of the two tracks which in turn will result in slippage and soil shearing in order to achieve the steering. These phenomena of slippage and soil shearing are highly nonlinear and difficult to reliably quantify and cause inaccurate tracked vehicle kinematics. The kinematic inaccuracies make it difficult to predict the exact motion of the tracked vehicle and increase the complexity of the task of controlling the motion of the tracked vehicle. In order to overcome this problem, Wong proposed a slip (or skid) parameter which depends on the thrust forces of the left and right tracks, vehicle weight, and the nature of the terrain. He included this parameter, which can be found experimentally, in the kinematic equations of the tracked vehicle to account for the track-ground interaction. Le et al [3] used the Extended Kalman Filter (EKF) to estimate the slip (or skid) parameters during simulated motion of the tracked vehicle when maneuvering on different terrains. During the motion, the EKF receives the tracks angular speeds and the pose of the vehicle from the model as observations, then the EKF estimates the position of the vehicle, and computes the slip (or skid) parameters of both tracks.

Martinez et al [1] used skid steering for directional control of mobile robots. But, they proposed a different kinematic approach than those used in [2, 3] for tracked mobile robots in order to improve the robot motion control and localization. Their basic approach involves finding the best model of the vehicle kinematics by obtaining a geometric analogy to a tracked vehicle with a corresponding wheeled one. They assumed a tracked vehicle using skid steering where the motion of each of the two tracks is to be considered separately. This would result in two additional degrees of freedom consisting of the track's roll. The motion of a point on the tread surface is the vectorial sum of the motion of the vehicle and that of the track roll. Hence, the instantaneous center of rotation (ICR) of a track on the plane is different from that of the entire vehicle. Comparison of the ICR of a tracked vehicle with that of a wheeled vehicle using a differential drive shows the ICR of the wheels to be constant and coincident with the ground contact points, whereas the ICRs of the tracks are dynamic and lie outside the track's centerlines. Martinez et al concluded that the slippage phenomenon is the contributing factor to the change in the positions of the tracks ICRs. The analogy between a tracked vehicle and a wheeled vehicle has been considered to approximate a dynamics-free tracked kinematic model. In their approach they used a genetic algorithm for identifying optimized constant values for the tracks ICRs that are equivalent to those of a corresponding wheeled vehicle given a set of working conditions. They contend that this would allow conventional path tracking methods to be applied effectively without any modifications.

The skid steering kinematic approach proposed by Wong is used in this thesis. Wong's approach is more accurate since he based it on experimental observations, while the other approaches are approximation approaches based primarily on simulations.

2.3 TAGV Dynamics

An accurate dynamic model of the TAGV is required for the development of the control algorithm. The model can be based on Newton's dynamics where force and moment equations dependent on soil mechanics and vehicle dynamics are involved as explained by Martinez, Wong, Le, and Ferretti & Girelli [1-4]. Forces on the vehicle are divided into tracks thrust and resisting forces acting on the tracks and vehicle. These can be further divided into internal resistance forces, resistance due to vehicle-terrain interaction, and aerodynamic resistance forces. The moments on the TAGV result from the difference between the thrust forces of the tracks and from the resisting moment exerted on the vehicle tracks from the ground.

In [2] and [3], it has been explained that during vehicle turning, a moment of turning resistance will be exerted on the tracks of the vehicle by the ground. This moment depends on the vehicle steering speed, soil type, design of the vehicle track, turning radius, and on the vehicle weight. Wong [2] and Le [3] have also included in the dynamic model general longitudinal and lateral resistance forces acting on the vehicle tracks during maneuvering. The longitudinal resistance is directly related to the vehicle weight and the longitudinal friction coefficient, whereas the lateral resistance depends on the vehicle weight, the lateral friction coefficient, and the track length.

Martinez et al [1] included in the moment equation the gyroscopic effects of the set of internal moving parts of the vehicle. The resisting forces from the ground on the tracks are due to the pressure field perpendicular to the contact plane and oppose the weight of the vehicle. Another source accounting for the resisting forces is the friction forces parallel to the contact plane. Martinez et al used the resisting forces in modeling the track-soil interaction; furthermore, they took into account the motion resistance caused by the compaction effect that the vehicle produces on the ground.

Ferretti and Girelli [4] model of an agricultural tracked vehicle is similar to that of Wong [2] with the exception that they neglected the aerodynamic resistance. The resisting forces of the agricultural tracked vehicle are split into internal and external. The internal resistance has been modeled by a linear viscous friction torque acting around the sprocket shaft. Whereas the external resistance is mainly due to vehicle-terrain compaction.

It can be seen from the above mentioned publications that some researchers include nonlinear dynamic terms in the system model while others simplify or simply ignore them. Since a precise dynamic model is important for the controller design, both preceding approaches have advantages and disadvantages. The advantages and disadvantages depend on the controller type that is employed for the system. Developing the dynamic model of a system close to reality increases the degree of nonlinearity and uncertainty of the system model to such an extent that it might complicate the controller design. However, some controller designs, like the sliding mode controller, are very robust and have the capability to overcome the system nonlinearities and uncertainties. Hence, having a simple model of a system might be more robust than a complex one with the choice of a sliding mode controller.

2.4 TAGV Path Planning Techniques

For a mobile robot or vehicle controller design, it is important to consider the ability of the vehicle to reach the final pose and the strategy used to accomplish the task. The motion of a TAGV is carried out subject to many constraints, among them are; kinematic constraint, track-terrain interaction, motor power-velocity curves, and tracked vehicle dynamics. Given the necessary information about the current TAGV pose and the required final pose, the transition from the former to the latter can be accomplished by using a suitable path planning technique or algorithm.

Path planning can be classified into three categories; the first is high level path planning approaches [5, 6] that can be carried out off-line to obtain the optimum path between any given two points in the robot environment, the second is the obstacle avoidance approaches [7, 8] that require knowledge of the start point and the end point, and the third is online analytical approaches [9] where initial conditions of the start pose and the end pose are known. The following sections elaborate on scientific literature dealing with the three approaches.

Fraichard and Mermond [5] developed a path planning approach for a car-like robot with position and orientation uncertainties. Landmarks are assumed to exist, and the path consists of a sequence of jumps from one landmark to the next until the goal is reached. This approach utilizes a two-phase path planner approach. The first phase is a learning one where a Probabilistic Path Planner algorithm (PPP) is used. PPP builds feasible and robust paths or roadmaps in the robot work space by generating and interconnecting a large number of robot configurations. These roadmaps are used for answering path planning queries. In other words, the roadmaps respect the nonholonomic constraints of the robot to ensure that it will reach its goal by following these roadmaps. The second phase is the query phase where an initial and final configuration of the robot are given. PPP algorithm connects the initial and final configurations to the roadmap and then searches the roadmap in order to build a complete solution path.

If path planning is to be carried out in real time, the technique used must be fast and efficient. Razavian et al [6] proposed a Cognitive Based Adaptive Path Planning Algorithm (CBAPPA) for autonomous guided vehicles. They based it on the observed capability of biological systems which ignore any inappropriate information and quickly process efficient paths. CBAPPA works by taking the existing knowledge of the environment and then determines the path planning that guides the robot through a path that avoids obstacles. They hypothesized that in order to plan a draft path from source to destination, three simple steps may be followed: The first is to determine the heading and direction of travel, the second is to account for known obstacles based on an understanding of the environment, and the third is to plan a draft path before moving towards the destination. CBAPPA consists of two stages: The primary path stage, and the refined path stage. The primary path starts with a straight line from the starting position to the goal position where some obstacles are known. Circular rings are formed around the known obstacles in the environment. When the primary path intersects a ring, it follows the curve of the ring to go around the obstacle and back to the straight-line path on the other side of the obstacle. While the robot is moving in the environment, some other obstacles might show up. The CBAPPA performs the second stage after updating the database with the new information about the new obstacles. In a manner similar to that of the primary path approach, the refined path uses the new information about the obstacles to re-create the robot refined path to overlay on the primary path.

Khatib [7] proposed the idea of potential fields to solve the path planning problem in the presence of obstacles. He used the phenomena of an electrostatic field to develop his method. The obstacles generate a repulsive field whereas the desired destination emits an attractive field. Hence, the robot will move by following the attractive field just as a ball would roll downhill. Also, Louste and Liegeois [8] used the idea of potential field methods to come up with a yet newer approach for path planning. In that technique they proposed using a potential viscous fluid field which is based on Stoke's equations for incompressible viscous fluids.

It is known that nonholonomic systems are governed by constraints that are nonintegrable differential expressions. Y. Wang [9] proved that the problem of steering systems with nonholonomic constraints between any two arbitrary configurations can be converted into a polynomial fitting problem. Therefore, the complicated nonholonomic path planning problem can be dealt with easily using standard techniques like "curve fitting". Assume a car-like robot in an environment with *xy*-world coordinate, the approach of polynomial fitting can be accomplished by converting the nonholonomic motion planning problem into a problem of finding a function $y=f(x)$ which satisfies the nonholonomic constraints and the boundary conditions of the robot. The boundary conditions can be the initial and the final configurations of the robot. A suitable polynomial can be chosen based on the constraints and boundary conditions. In this paper, a quintic polynomial was used and compared with a cubic polynomial for the same constraints and boundary conditions. The results showed that the algorithm is efficient and that the generated path is quite similar to that followed by a real car used on roads.

For the purposes of this thesis, an analytical approach is used to guide the TAGV over a predefined path.

2.5 TAGV Control

Motion control of skid steered tracked vehicles is a relatively new area of research. As it has been explained earlier, skid steering results in complex track-terrain interactions which makes the modeling of a tracked vehicle, for the purposes of motion control, very difficult. Published literature dealing with motion control of TAGVs are scarce. Only one paper directly dealing with this subject has been found to date [10]. However, some publications on non autonomous motion control of tracked vehicles are available.

Saeedi and Lawrence [10] described a vision-based control system for a tracked mobile robot. The system comprises several controllers in a hierarchal architecture to move the tracked vehicle from a starting position to a goal position for a given predefined path plan. The first level controller is a fuzzy logic path-tracking algorithm which estimates the rotational and translational velocities of the tracked vehicle based on a given path. The resulting information is used in the inverse kinematics equations of motion to calculate the corresponding left and right track reference speeds. The reference speeds are adjusted using a coefficient determined based on the occurrence of track slippage. The second level controller is the cross coupling motion controller. This is primarily a proportional-integral (PI) controller. First the linear output positions of the tracks are multiplied by fixed gains. The difference between the left and right track modified positions is then passed to the PI-controller. This controller ensures that the vehicle has zero steady state orientation angle error. The cross coupling controller outputs are the controlled individual tracks speeds used in the track-motor subsystem model to produce the rotational velocities of the tracks. The track-motor subsystem was experimentally modeled as a first order transfer function with a delay term. The high level controller is a vision-based tracking system used to correct for track slippage problems. If the track motion calculations based on the speedometer readings exceed the track motion calculations from the vision system, a slippage value is calculated for the slippage controller. The slippage controller uses this slippage value to compute the earlier mentioned scaling coefficient factor to correct for the left and right track reference speeds.

The following sections highlight published literature on the motion control of non autonomous tracked vehicles. Ahmadi et al [11] proposed a path following control algorithm for a tracked vehicle to guide the vehicle from one pose to another. They used the dynamic model of the vehicle including friction in the control algorithm. The controller is based on feedback linearization of the track-soil interaction equations with feedforward friction compensation. The input control signal to the system is selected to be the thrust forces. The corresponding angular velocities of the tracks can be calculated based on feedback linearization of the thrust force-slip model equations of the tracked vehicle.

G. Wang et al [12] proposed a robust controller for a tracked vehicle using the Quantitative Feedback Theory (QFT). The tracked vehicle is modeled as a two-input/two-output system. The two inputs to the tracked vehicle are the throttle and steering whereas the measured outputs are the rotational and longitudinal vehicle's speeds. The model is highly nonlinear and time varying; hence, it was linearized by designing a set of time invariant linear single loop systems using the QFT. The Nichols chart approach was then used to design the individual single loop controllers separately for a certain system operating regions.

Fan et al [13] classified the system error as internal and external errors. Internal errors relate to internal drive errors and can be sensed by sensors like wheel encoders. External errors are divided into systematic external errors and non systematic external errors. The systematic external error might be caused by factors such as different wheels diameters or wheels misalignment. The non systematic external errors relate primarily to track slippage and can be detected by absolute motion measurement sensors such as a vision system. Fan et al considered the largest components of external errors to be due to systematic errors. In order to correct for these errors, a hybrid control technique has been designed and implemented for a tracked mobile robot. Two control algorithms were employed. The first is a cross coupling control algorithm, and the second is an adaptive control algorithm. The cross coupling algorithm is similar to the one used by Saeedi and Lawrence [10]. Fan et al used cross coupling to compensate for the internal errors and the adaptive control algorithm to compensate for the external errors. The combinations of these two control algorithms form the hybrid motion control.

Although various controller design approaches have been proposed, control problems associated with system uncertainties, presence of high-order dynamics, and system inherent nonlinearities remain big challenges. SMC opened up a wide area of development for controller design. It provides robustness in the presence of modeling uncertainties, nonlinearities, and disturbances. One of the publications on wheeled vehicles using a sliding mode controller was proposed by Yang and Kim [14]. They introduced a SMC for trajectory tracking of nonholonomic wheeled mobile robots. The proposed control algorithm used the computed torque method for feedback linearization of the dynamic equations coupled with the theory of SMCs. Two control inputs were applied to the vehicle to give the required angular and translational velocities of the vehicle. The control inputs are calculated based on the error of the robot pose in polar coordinates and the sliding surfaces equations. By applying the SMC, it was shown that the behavior of the vehicle is robust against initial condition errors and external disturbances such as noise in the control signals.

The fundamental theory of SMC is explained in the following sections.

2.6 Sliding Mode Controller (SMC)

There is no single control algorithm design solution to different control system problems. Some methods may be more attractive for certain control problems, while others may also be acceptable. One of the most attractive controller designs is the SMC which has broadened the horizon of development for a control engineer.

SMC is based on the theory of Variable Structure Systems (VSS) which first appeared in the late fifties in Russia as a special class of nonlinear systems [15]. SMC is characterized by a discontinuous control action which changes the structure of the controller when a predetermined switching surface is reached. This surface is known as the sliding surface. In other words, in VSS the controller is allowed to change its structure, that is, to switch at any instant from one to another member of a set of possible continuous functions of the state based on a predefined switching logic [16]. This nature of the VSS can result in a very robust control system and thus provides the possibility of achieving the desired goals. Some promising features of SMC are listed below [16]:

- The equation of SMC dynamics can be designed to be linear despite the fact that the original system might be governed by nonlinear equations.
- The sliding mode depends on the selection of its parameters, and that is primarily a design

consideration that is done by the designer.

- Once the sliding motion happens, the system disturbances and uncertainties will not affect this motion (i.e., the system performance can be completely determined from the sliding motion).
- SMC system possesses new properties not present in any of the structures used separately. For example, a stable system may consist of two structures neither of which is stable.

The design procedure of SMC consists of two stages. In the first stage, the equation of the sliding surface or the manifold with sliding mode is designed in a way to meet the desired dynamics of the sliding motion in accordance with some performance specifications. Then, the switching or discontinuous feedback control law is designed such that the locus of the system state would reach the manifold and such that the sliding mode exists on this manifold. The stages of SMC design are explained in the following section.

2.6.1 Sliding Surface and Switching Control Law Design

One of the important methods used to analyze or study a control system, whether linear or nonlinear, is the phase plane analysis. The phase plane analysis is a graphical method for studying a system by generating motion trajectories corresponding to various initial conditions, and then examining the qualitative features of the trajectories such that information concerning stability of the system can be obtained [17]. The phase plane of a SMC system shows the sliding mode motion. This motion is described by motion trajectories directed towards the sliding or switching surface.

Sliding mode surfaces can be either linear or nonlinear. The design of linear sliding mode surfaces for linear systems were studied and developed in depth. The design of sliding surface for more general nonlinear systems remains largely an open problem [15]. In this thesis, the focus is only on linear sliding mode surfaces. Once the sliding surface has been designed, the switching feedback control law can be selected. Some common methods for designing the sliding mode surface equation and the switching feedback control law are summarized in the following sections.

Hung et al [18] presented a tutorial on variable structure control. The purpose is to introduce the reader to the fundamental theory of SMC design approaches. They started by explaining the basic idea of the VSS in detail. Then they suggested some methods to define the differential equation for the sliding mode surface. In one of the methods, the coefficients of a linear sliding surface function are chosen based on the ability to transform the system model to a controllable canonic form. In this form, the coefficient selection defines the characteristic equation of the sliding mode (i.e., the characteristics of the closed-loop system after reaching the sliding surface). Another method for describing the dynamics of the sliding mode surface is called the equivalent control approach. The first step of this approach is to find the equivalent control equation by merging the condition that guarantees the trajectory to stay on the switching surface with the system model. The condition can be expressed by having the rate of change of the sliding mode surface equation equal to zero. The sliding mode parameters can be chosen in a way to satisfy the system performance after substituting the equivalent control into the original system model. Hung et al also provided some approaches for choosing the parameters of the switching control law. They proposed reaching condition approaches under which the locus of the state of the system will move towards the sliding surface. One of the approaches for specifying the reaching condition is the Lyapunov function approach. Once Lyapunov function is found, the switching control parameters can be chosen in a way to satisfy the reaching condition.

A coordinate transformation method to design the sliding surface has been proposed by Y. Li [15]. This method supposes the existence of a nonsingular transformation form for the system. The procedure shows that the desired system performance can be achieved by the design of an appropriate sliding surface. This is possible by the use of one of the classical control feedback design methods, such as the pole placement or the linear quadratic approaches. The transformation method was also used by Pan et al [19].

Y. Li [15] proposed another approach called the linear quadratic (LQ) approach. LQ gives an optimal choice of the sliding surface coefficients by minimizing a quadratic cost function over an infinite time interval.

Ackermann and Utkin [20] used Ackermann's formula to find the sliding surface parameters vector in an explicit form without the sliding mode equation based on the original system model. Ackermann's formula is used to find the desired eigenvalues of a linear system. Then, the sliding surface parameters can be determined by applying the earlier mentioned condition that guarantees staying on the sliding surface [18].

Most other publications about designing a SMC explained same mathematical theory or conditions for designing the sliding surface and the switching control law. For instance, Young et al [21] presented a control engineer's guide to sliding mode control design and DeCarlo et al [22] presented a tutorial on variable structure control of nonlinear multivariable systems where same design theory can be found.

The SMC control design is still a serious challenge for control engineers since the design theories or conditions are still insufficient in most design cases. Hence, some have integrated the classical theories used for designing the sliding mode surface and the switching control law with other computational intelligence-based systems such as Fuzzy Logic (FL), Neural Networks (NN), and Genetic Algorithms (GA). However, despite its huge success and industrial applications, the lack of systematic design and mathematical rigor have hindered its application in many applications. Recently, the integration of computational intelligence-based techniques and conventional control approaches has been an active research focus. It is claimed that this union will lead to new control algorithms that exploit the advantages of the two patterns [23]. Some papers on integrated SMC and intelligence systems are summarized in the following sections.

J. Wang et al [23] proposed an online adaptive fuzzy sliding mode control. The sliding surface parameters are chosen using the conventional techniques mentioned previously while the control law is directly substituted by a fuzzy system. The major drawback of this approach is the difficulty involved in finding the optimal or sub-optimal rules and membership functions of the FL controller. Such rules can drive the system state to hit the sliding surface as fast as possible. Hence, an on-line adaptive tuning algorithm for the consequent parameters in the if-then fuzzy rules is designed. Another technique to tune up the if-then fuzzy rules as well as the membership functions is proposed by Lin and Chen [24]. Lin et al used GA technique to search for the optimal or sub-optimal fuzzy rules for a fuzzy sliding mode controller design. Also, Ghalia and Alouani [25] integrated the fuzzy rules with the SMC design but in a different way. They designed the sliding surface as well as the switching control law using the same classical theory or conditions explained earlier. The difference is in the employment of a set of fuzzy rules that should modify the behavior of the system while it is changing from the reaching mode to the sliding mode and vice versa. This can be done by choosing the appropriate switching control gain that should be provided by the fuzzy rules.

A neural network sliding mode control design approach has been proposed by Jezernik et al [26]. This approach was created to deal with problem of the existence of nonlinearities and uncertainties in the control law resulting from the system model itself. The neural networks are used for the approximation of nonlinear functions in the control law. The advantage of this approach is that no precise knowledge of a mathematical model is necessary. Hence, this approach overcomes the major drawback of conventional controller design methods where a mathematical development of the controller is necessary. The major drawback of this approach, however, is need to train the neural network.

Since none of the above mentioned SMC design approaches offered satisfaction and coherent methodology of design, the need for such a methodology provided the motivation for this thesis. Furthermore, no literature was found on the link between the controller gains and the sliding surface gains. Such a link has been derived and justified in this thesis.

2.6.2 Chattering Phenomenon

In order to design a SMC, a switching control law across the sliding surface between the two controller structures is needed to maintain the system state on that surface. Since the implementation of the associated control switching is imperfect [17], this leads to a phenomenon known as "Chattering". Utkin et al [27] described the term "Chattering" as the phenomenon of a finite-frequency oscillations that might appear in many sliding mode implementations. These oscillations are caused by a high-frequency switching of the sliding mode controller which may excite high frequency unmodeled dynamics in the system. Exciting the unmodeled dynamics results in oscillations in the system trajectory [27].

Without a proper treatment in the SMC design, chattering may be a major obstacle to the practical implementation of sliding mode controllers in a wide range of applications. The solution for the chattering problem is of a great importance especially when recognizing the benefits of applying a SMC on a real system.

In general, chattering must be eliminated for the controller to perform properly. Utkin et al [27] summarized some methods to solve the chattering problem. The most common of these is that of the boundary layer. In this approach, the switching control law is replaced by a saturation function which approximates the sign term by a boundary layer neighboring the sliding surface. Slotine and Li [17] also used the same approach of the boundary layer in order to smooth out the control discontinuity within a thin boundary layer straddling the sliding surface.

Another method was proposed by Utkin et al [27] is the observer-based solution. The key idea here is to generate an ideal sliding mode in an auxiliary observer loop rather than in the main control loop. Ideal sliding mode is possible in the observer loop since it is entirely generated in the control software and thus does not contain any unmodeled dynamics. The main loop follows the observer loop according to the observer dynamics such that no chattering occurs and the system behaves as if a continuous controller is applied.

Sadati and Talasaz [28] proposed another method to eliminate the chattering. For a conventional SMC, the switching control gain is chosen to be large and fixed in order to compensate for the uncertainties; therefore, a chattering will appear on the sliding surface. An appropriate control signal is applied when the states are far from or close to the sliding surface by substituting the switching function with a continuous control gain using fuzzy control gain. The fuzzy control gain is varied by an adaptive control law extracted from Lyapunov stability conditions.

M. Chen et al [29] also reduced the chattering by employing an online adjusting of the boundary layer width around the sliding surface. A decaying width boundary layer approach has been applied by adding an exponential term to the control law to smooth out the control signal and hence reducing the chattering. Then, they proposed a new boundary layer design where the width of the boundary layer is proportional to the system state norm.

The last approach to solve the chattering problem is the dithering technique proposed by Iannelli et al [30]. A high frequency signal called the dither signal is injected at the input of the discontinuous control signal. The dithering can be used as a boundary layer approach for the compensation of chattering in the SMC. The boundary layer can be adapted by simply changing the dither shape. A suitable dither shape must be chosen carefully for smoothing the discontinuous function in the system.

Since the boundary layer approach is quite useful and simple for most systems, it is applied to the TAGV control system of this thesis.

Chapter 3

Tracked Autonomous Guided Vehicle Model

3.1 Introduction:

A model representing the dynamic behavior of a tracked autonomous guided vehicle is developed. In this chapter, the model includes the full kinematic and dynamic equations and takes into account the vehicle skid steering model and the mechanics of vehicle-terrain interaction. A complete submodel of the driving motors dynamics is also included.

An example of a tracked vehicle is the Vanguard MK2 shown in Figure 3.1.

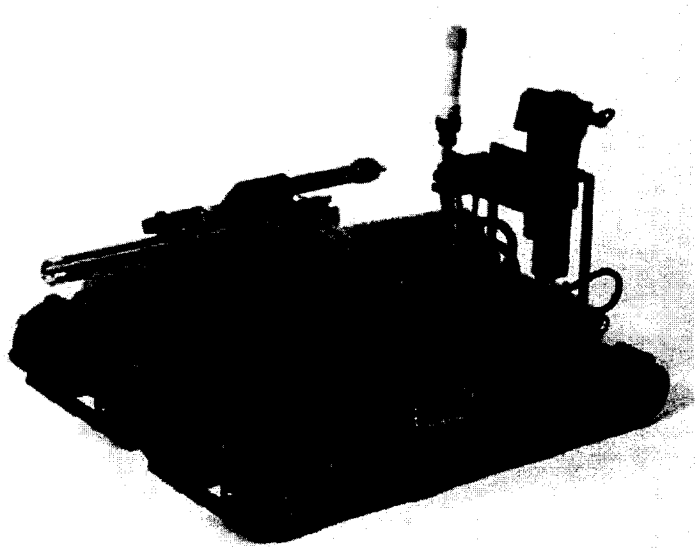

Figure 3.1: Vanguard MK2 tracked vehicle

The Vanguard MK2 is equipped with two tracks to move the vehicle towards the desired position. Two DC motors are used to provide power to the tracks and are controlled separately. Between the two tracks is the body of the vehicle which contains all the electronics necessary to receive and send information from /to the vehicle tracks motors. Different sensors are also installed to collect information about the vehicle and its environment. The types of tracks can be exchanged based on the mission of the vehicle since it can be deployed inside and outside buildings. The vehicle is designed to work with chemical, biological, radiological, nuclear, and explosive threats. It can also be used for surveillance and security operations. An arm is mounted on top of the vehicle to be used for special tasks as required. Some features and capacities of the robot are listed in Table 3.1.

Table 3.1: Vanguard MK2 features and capacities

Vanguard MK2 Standard Features	***Description***
Drive system	Two 7.6 *cm* wide rubber independent tracks driven by two DC motors
Battery packs	24VDC
RF System	Wireless system
Command and control station	Laptop with robot software interface
Overall length	91.5 *cm*
Overall width	43.5 *cm*
Stowed height	40.5 *cm*
Overall weight	52 *kg*

3.2 Tracked Vehicle Kinematics

The basic architecture of a tracked vehicle is that of a chassis equipped with two tracks. Each track has a role in enabling the whole vehicle to move, and at the same time, imposes constraint on the vehicle's motion. The tracks are tied together based on the vehicle chassis geometry, and therefore their constraints combine to form a global constraint on the overall motion of the vehicle chassis. The resulting constraint is nonholonomic and prevents the vehicle from moving laterally [27]. A notation that allows expressing the robot motion in a global or a world reference frame as well as robots's local reference frame is introduced in this chapter. A kinematic model of a simple mobile robot consisting of two wheels will be then explained as an introduction to tracked vehicle kinematics. Finally the model of a tracked vehicle with skid steering will be proposed.

3.2.1 Differential Steering Kinematics

Consider a mobile robot system having a set of wheels with a common axle but independent wheel actuators as shown in Figure 3.2. This simple wheel-based propulsion system is commonly used for mobile robots where the two wheels are powered and controlled separately, thus providing both the drive and the steering functionalities. If one wheel rotates faster than the other, the robot follows a curved path with the center of rotation lying along the common axis and nearer to the slower wheel. If the wheels turn at equal speeds and in the same direction, the robot moves in a straight line. If the wheels turn at equal speeds but opposite directions, the robot pivots. Thus, steering the robot is just a matter of varying the speeds of the drive wheels. In order to choose the speeds such that the robot will move along a given trajectory, a mathematical equation describing the robot motion has to be derived. This will be used when implementing the robot motion control software.

With reference to the schematic of the system shown in Figure 3.2, the nomenclature and sign convention used are as follows; assume a rider on the vehicle facing forward, "L" and "R" subscripts will refer to the left and right wheels respectively. Positive displacement, velocity, and acceleration are taken in the forward direction. The heading is measured with respect to the x-axis following the right hand rule with the z-axis taken upward. Angular velocity and acceleration are taken positive following the right hand rule. The subscripts "in" and "out" will designate the wheel nearer to and further away from the center of the path curvature respectively.

Assume that no wheel slip or skid occur, the motion of each wheel is restricted to a longitudinal direction with translational velocities V_R and V_L for the right and left wheels respectively. These linear velocities combine to produce robot translational and rotational velocities V and ω. The robot will not move laterally along the robot coordinate axis y_L because of the nonholonomic constraint. Figure 3.2 also shows the world reference frame (Y_w, X_w) and the robot local frame (y_L, x_L) as well as the robot pose (Y_w, X_w, θ).

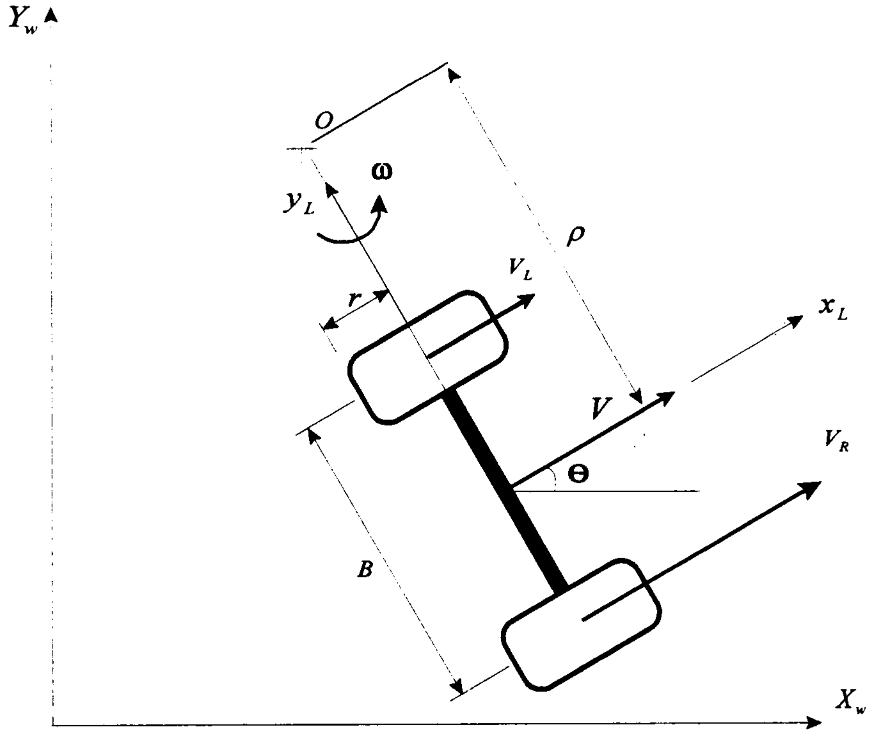

Figure 3.2: Principle of differential steering

The set of forward kinematic equations of the vehicle in the world coordinate frame is given by:

$$\begin{bmatrix} \dot{x} \\ \dot{y} \\ \dot{\theta} \end{bmatrix} = \begin{bmatrix} \cos\theta & 0 \\ \sin\theta & 0 \\ 0 & 1 \end{bmatrix} \begin{bmatrix} V \\ \omega \end{bmatrix} \tag{3.1}$$

subject to the constraint

$$\dot{y}\cos\theta - \dot{x}\sin\theta = 0 \tag{3.2}$$

Equation 3.2 expresses the nonholonomic constraint which specifies that the motion of the robot can not occur along the wheels axis. This is a nonintegrable constraint which involves time derivative of the robot pose.

With reference to the figure, the robot rotational velocity ω around the *z*-axis in yaw, i.e. the robot heading angle rate of change $\dot{\theta}$, is given by:

$$\omega = \dot{\theta} = \frac{V_R - V_L}{B} \tag{3.3}$$

where B is the distance between the centerlines of the two wheels, or wheel base, as shown in Figure 3.2.

For the remainder of this thesis $\dot{\theta}$ will be used instead of ω to avoid possible confusion with the angular velocities of the tracks motors.

The linear velocity of the robot is the average of the two wheels velocities, and is given by:

$$V = \frac{V_R + V_L}{2} \tag{3.4}$$

The robot rotational velocity can also be written in terms of the robot translational velocity and the path radius of curvature as follows:

$$\dot{\theta} = \frac{V}{\rho} \tag{3.5}$$

where ρ is the radius of curvature when the robot is turning around point O.

Combining Equations 3.3, 3.4 and 3.5, the robot turning radius of curvature ρ and the robot rotational velocity $\dot{\theta}$ can be expressed as follows:

$$\rho = \frac{B\,(V_R + V_L)}{2\,(V_R - V_L)} \tag{3.6}$$

$$\dot{\theta} = \frac{V_R + V_L}{2\rho} \tag{3.7}$$

While these equations have been derived for a wheeled robot, they are also applicable to a tracked vehicle where the tracks have replaced the wheels. It should be noted, however, that in the case of tracks, the assumption that no slip or skid occur must also be made for the equations to be valid.

The following two sections (3.2.2 and 3.3) are a re-working of skid steering kinematics and dynamics as given by Wong [2]. These sections are presented here for completion and clarity.

3.2.2 Skid Steering Kinematics

Figure 3.3 shows a schematic diagram of a tracked vehicle. The figure shows the tracked vehicle turning about a center O. The motion of the tracked vehicle in the global frame can be expressed using the same equations derived earlier for the wheeled vehicle.

Consider that the sprocket of the outside track of a tracked vehicle is rotating at an angular speed of $\omega_{R(out)}$ and that of the inside track is rotating at an angular speed of $\omega_{L(in)}$. If tracks slip and skid is ignored, then the turning radius ρ and the rotational velocity of the vehicle $\dot{\theta}$ around the *z*-axis are given by:

$$\rho = \frac{B}{2} \frac{(r\omega_{R(out)} + r\omega_{L(in)})}{(r\omega_{R(out)} - r\omega_{L(in)})} \tag{3.8}$$

$$\begin{aligned} \dot{\theta} &= \frac{r\omega_{R(out)} + r\omega_{L(in)}}{2\rho} \\ &= \frac{r\omega_{R(out)} - r\omega_{L(in)}}{B} \end{aligned} \tag{3.9}$$

where *r* is the radius of the track sprocket.

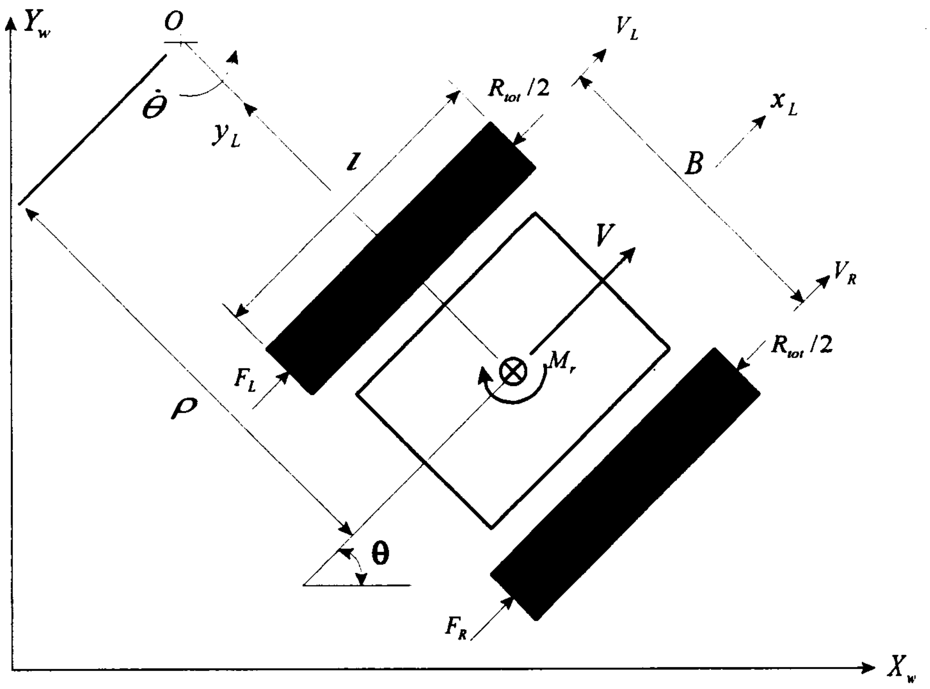

Figure 3.3: Principle of skid steering

With reference to Figure 3.3 [2], skid steering is achieved by applying an appropriate thrust or braking force to the tracks in order to steer the vehicle along a prescribed path. Depending on whether a forward thrust or a braking force is applied, a track may either slip or skid. When the skid or slip of the track is taken into consideration, the turning radius of curvature ρ and the rotational velocity $\dot{\theta}$ equations of the vehicle will change. Wong [2] has proposed the introduction of a parameter into Equations 3.8 and 3.9 to account for the slip or skid as follows:

$$\rho' = \frac{B}{2}\frac{[r\omega_{R(out)}(1-i_{R(out)}) + r\omega_{L(in)}(1-i_{L(in)})]}{[r\omega_{R(out)}(1-i_{R(out)}) - r\omega_{L(in)}(1-i_{L(in)})]} \tag{3.10}$$

$$\begin{aligned}\dot{\theta}' &= \frac{r\omega_{R(out)}(1-i_{R(out)}) + r\omega_{L(in)}(1-i_{L(in)})}{2\rho'} \\ &= \frac{r\omega_{R(out)}(1-i_{R(out)}) - r\omega_{L(in)}(1-i_{L(in)})}{B}\end{aligned} \tag{3.11}$$

In Equation 3.10 and 3.11, ρ' and $\dot{\theta}'$ are the modified vehicle turning radius and rotational velocity respectively due to the existence of the slip or skid. $i_{R(out)}$ and $i_{L(in)}$ are the slip or skid of the right track and the left tracks respectively. For a given vehicle moving over a particular terrain, the values of $i_{R(out)}$ and $i_{L(in)}$ depend on the thrust forces of both the left and right tracks of the vehicle, the vehicle weight, as well as on the terrain characteristics. The values of $i_{R(out)}$ and $i_{L(in)}$ can be determined experimentally as explained by Wong [2].

3.3 Tracked Vehicle Dynamics

Various dynamic models with different ranges of complexities have been introduced in the literature survey. The focus of this section is on the development of a model that accurately represents the behavior of the tracked vehicle especially while turning. When the vehicle is turning, tracks slip and skid will occur. This in turn will have an effect on the controllability of the vehicle.

3.3.1 Skid Steering Kinetics

The turning behavior of a tracked vehicle using skid steering depends on the thrust forces of the inside and outside tracks $F_{R(out)}$ and $F_{L(in)}$, the resultant resisting force R_{tot}, the moment of turning resistance M_r exerted on the tracks by the ground, and the vehicle parameters as shown in Figure 3.3. Assuming the simple case of steering at low vehicle speeds. The centrifugal force may be neglected, and the behavior of the vehicle can be described by the following equations of motion:

$$m\frac{d^2s}{dt^2} = F_{R(out)} + F_{L(in)} - R_{tot} \tag{3.12}$$

$$I_z\frac{d^2\theta}{dt^2} = \frac{B}{2}(F_{R(out)} - F_{L(in)}) - M_r \tag{3.13}$$

where,

s is the displacement of the center of mass of the vehicle

θ is the angular displacement of the vehicle

B is the distance between the centerlines of the two tracks as shown in the figure

I_z is the mass moment of inertia of the vehicle about the vertical axis passing through its center of mass

m is the mass of the vehicle

Assuming constant velocity motion, i.e., no linear or angular accelerations, the equations of motions reduce to:

$$F_{R(out)} + F_{L(in)} - R_{tot} = 0 \tag{3.14}$$

$$\frac{B}{2}(F_{R(out)} - F_{L(in)}) - M_r = 0 \tag{3.15}$$

Solving Equations 3.14 and 3.15 simultaneously for $F_{R(out)}$ and $F_{L(in)}$ gives:

$$\begin{aligned} F_{R(out)} &= \frac{R_{tot}}{2} + \frac{M_r}{B} \\ &= \frac{f_r W}{2} + \frac{M_r}{B} \end{aligned} \tag{3.16}$$

$$\begin{aligned} F_{L(in)} &= \frac{R_{tot}}{2} - \frac{M_r}{B} \\ &= \frac{f_r W}{2} - \frac{M_r}{B} \end{aligned} \tag{3.17}$$

where f_r is the coefficient of resistance to motion of the vehicle in the longitudinal direction and W is the vehicle weight.

The value of f_r depends on the vehicle translational velocity V and the tracks contour. Wang [2] proposed the following experimental equation to estimate f_r for military tracked vehicles:

$$f_r = f_o + f_s V \tag{3.18}$$

where f_o and f_s are experimental coefficients. For tracks having double, rubber-bushed pins, and rubber pads, the value of f_o is 0.03. If the tracks are all-steel, and single-pin, the value of f_o is 0.025; and for tracks having sealed, lubricated pin joints with needle bearing, it is 0.015. The value of f_s varies with the type of the tracks; however, it can be approximated to be 0.00015 [2].

To determine the values of the thrust forces $F_{R(out)}$ and $F_{L(in)}$, the moment of turning resistance M_r must be known. M_r depends on the weight of the vehicle, the geometry of contact patch between the track and the ground, and the coefficient of friction between the track and the ground. Since, for a given track, the coefficient of friction and the contact patch varies depending on the nature of the ground and its contour, a number of assumptions have to be made. It will be assumed that each track carries an equal part of the vehicle weight and that the normal pressure is uniformly distributed along each track. Figure 3.4 [2] shows the top and the side schematic of a tracked vehicle turning about the center of mass O. With reference to the figure, the resulting lateral resistance per unit length of each track R_l is expressed by:

$$R_l = \frac{\mu_t W}{2l} \tag{3.19}$$

where μ_t is the coefficient of lateral resistance and l is the contact length of the track.

The value of μ_t depends on the nature of the ground and on the track contour. Table 3.2 [2] gives the average values of μ_t for steel and rubber tracks over different types of terrains.

Table 3.2: Average values of μ_t [2]

Track Material	Coefficient of Lateral Resistance μ_t		
	Concrete	Hard Ground (not paved)	Grass
Steel	0.50-0.51	0.55-0.58	0.87-1.11
Rubber	0.90-0.91	0.65-0.66	0.67-1.14

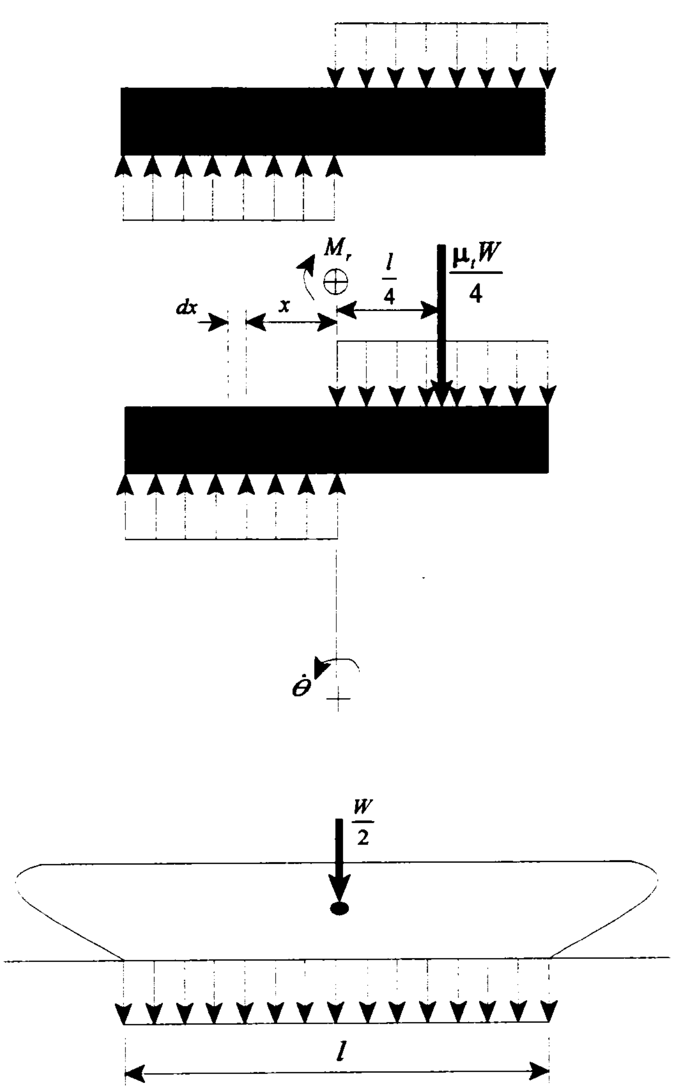

Figure 3.4: Moment of turning resistance with uniform pressure distribution

Integrating R_l over the entire length of the track results in the moment of turning resistance M_r as follows:

$$\begin{aligned} M_r &= 4\frac{W\mu_t}{2l}\int_0^{l/2} x\,dx \\ &= \frac{\mu_t W l}{4} \end{aligned} \tag{3.20}$$

Substituting Equation 3.20 into Equations 3.16 and 3.17, the thrust forces of the outside and inside tracks can be rewritten in the following form:

$$F_{R(out)} = \frac{f_r W}{2} + \frac{\mu_t W l}{4B} \tag{3.21}$$

$$F_{L(in)} = \frac{f_r W}{2} - \frac{\mu_t W l}{4B} \tag{3.22}$$

It should be noted that the value of M_r as calculated by Equation 3.20 is for a vehicle with a uniform normal pressure distribution and turning at low speed. In the case where the tracked vehicle is turning at high speed, the centrifugal force may be significant and its effect should be taken into consideration. If the center of mass is higher than the plane forming the sprockets, load transfer between the two tracks will also occur. The effect of the load transfer will be considered later. Figure 3.5 [2] shows a tracked vehicle turning at high constant velocity about a center O to the right. Because of the occurrence of a skid or slip, the turning radius changes. ρ' represents the resulting turning radius which forms an angle β with the line passes through the center of turning O'. The tracks thrust forces ($F_{R(in)}, F_{L(out)}$) and the resistance forces ($R_{R(in)}$, $R_{L(out)}$) are shown in Figure 3.5. Lateral resistance forces act on the tracks as a consequence of skid steering, and are assumed to be distributed as shown. With reference to Figure 3.5, to achieve equilibrium in the lateral direction, the resultant lateral resistance force exerted on the tracks by the ground must be equal to the centrifugal force. Similar to the case of low speed, assume that the normal pressure distribution along each track is uniform, and that the coefficient of lateral resistance μ_t is constant; then to satisfy the equilibrium condition in the lateral direction, the center of turning must lie at a distance s_o in front of the lateral centerline AC of the track-ground contact area as shown Figure 3.5. The equilibrium in the lateral direction can be expressed by applying Newton's second law as follows:

$$\left(\frac{l}{2}+s_o\right)\frac{\mu_t W}{l}-\left(\frac{l}{2}-s_o\right)\frac{\mu_t W}{l}=\frac{WV^2}{g\rho'}\cos\beta \tag{3.23}$$

It should be noted that, the right hand side of Equation 3.23 represents the centrifugal force along the lateral direction. Equation 3.19 is used to represent the lateral resistance per unit length of the track in Equation 3.23.

Solving Equation 3.23 for the displacement of the center of turning s_o gives:

$$\begin{aligned} s_o &= \frac{lV^2}{2\mu_t g\rho'}\cos\beta \\ &= \frac{la_y}{2\mu_t g}\cos\beta \end{aligned} \tag{3.24}$$

where $a_y = V^2/\rho'$, is the lateral acceleration of the center of mass of the vehicle.

Wong [2] assumed $\cos\beta$ to be equal to 1 since the turning radius ρ' is usually large compared to the contact length of the track l and in this case β would be small. Using the same assumption here, reduces Equation 3.24 to the following:

$$s_o = \frac{la_y}{2\mu_t g} \tag{3.25}$$

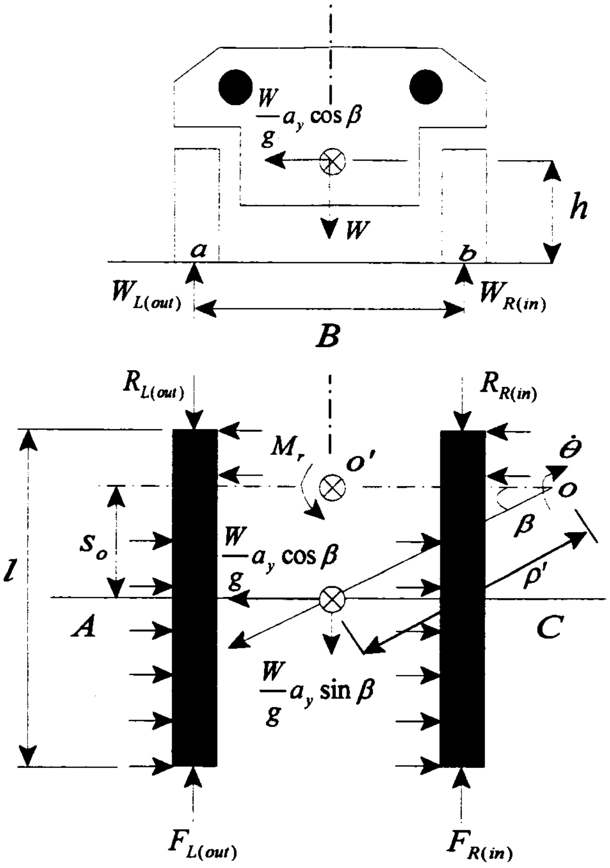

Figure 3.5: Forces acting on a tracked vehicle during turning at high speeds

As a result of the shift in the center of turning of the tracked vehicle, the equivalent moment of turning resistance M_r will have two components. The first is the moment of the lateral resistance exerted on the tracks from the ground about O'. The second is the moment of the centrifugal force about O'. Hence, with reference to Figure 3.5, M_r is expressed as follows:

$$\begin{aligned} M_r &= \frac{\mu_t W}{l}\left[\int_0^{l/2+s_o} x\,dx + \int_0^{-(l/2-s_o)} x\,dx\right] - \frac{WV^2 s_o}{g\rho'} \\ &= \frac{\mu_t W}{2l}\left(\frac{l^2}{2} + 2{s_o}^2\right) - \frac{WV^2 s_o}{g\rho'} \end{aligned} \tag{3.26}$$

Substituting Equation 3.25 into Equation 3.26 and solving gives:

$$\begin{aligned} M_r &= \frac{\mu_t W l}{4}\left(1-\frac{V^4}{g^2 \rho'^2 \mu_t^2}\right) \\ &= \frac{\mu_t W l}{4}\left(1-\frac{a_y^2}{g^2 \mu_t^2}\right) \end{aligned} \tag{3.27}$$

Comparing Equation 3.27 with Equation 3.20 derived for the case of turning at low speed shows that when the centrifugal force is taken into consideration, the equivalent moment of turning resistance is reduced.

The centrifugal force acting on the elevated center of mass of the vehicle results in a roll moment that will cause a lateral load transfer. Consequently, the resistance forces of the outside and inside tracks $R_{R(in)}$ and $R_{L(out)}$ of the vehicle will not be identical, and Equations 3.16 and 3.17 can be rewritten as follows:

$$F_{L(out)} = R_{L(out)} + \frac{M_r}{B} \tag{3.28}$$

$$F_{R(in)} = R_{R(in)} - \frac{M_r}{B} \tag{3.29}$$

With reference to Figure 3.5, the centerlines of the contact patches between the tracks of the vehicle and the ground are "*a*" and "*b*". Taking the moments of the forces acting on the vehicle about the contact centerlines *a* and *b* result in the following normal reaction equations:

$$W_{L(out)} = \frac{W}{2} + \frac{hWa_y}{Bg} \tag{3.30}$$

$$W_{R(in)} = \frac{W}{2} - \frac{hWa_y}{Bg} \tag{3.31}$$

where h is the height of the center of mass of the vehicle.

Hence, the resistance forces $R_{L(out)}$ and $R_{R(in)}$ are given by:

$$\begin{aligned} R_{L(out)} &= W_{L(out)} f_r \\ &= \left(\frac{W}{2} + \frac{hWa_y}{Bg}\right) f_r \end{aligned} \tag{3.32}$$

$$\begin{aligned} R_{R(in)} &= W_{R(in)} f_r \\ &= \left(\frac{W}{2} - \frac{hWa_y}{Bg}\right) f_r \end{aligned} \tag{3.33}$$

With reference to Figure 3.5, the centrifugal force has a component along the longitudinal axis of the vehicle given by:

$$Wa_y \sin\beta / g \tag{3.34}$$

but

$$\sin\beta = s_o / \rho' \tag{3.35}$$

Substituting Equation 3.35 into Equation 3.34 gives:

$$Wa_y s_o / g\rho' \tag{3.36}$$

This longitudinal component has to be compensated for from the thrust forces developed by the tracks. Hence, Equations 3.28 and 3.29 are given by:

$$F_{L(out)} = R_{L(out)} + \frac{Wa_y s_o}{2g\rho'} + \frac{M_r}{B} \tag{3.37}$$

$$F_{R(in)} = R_{R(in)} + \frac{Wa_y s_O}{2g\rho'} - \frac{M_r}{B} \tag{3.38}$$

Substituting Equations 3.27, 3.32 and 3.33 into Equations 3.37 and 3.38 results in the final form of the thrust forces of the inside and outside tracks required to maintain the vehicle at steady state while turning at high speed as follows:

$$F_{L(out)} = \left(\frac{W}{2} + \frac{hWa_y}{Bg}\right) f_r + \frac{Wa_y s_o}{2g\rho'} + \frac{\mu_t Wl}{4B}\left[1 - \left(\frac{a_y}{g\mu_t}\right)^2\right] \tag{3.39}$$

$$F_{R(in)} = \left(\frac{W}{2} - \frac{hWa_y}{Bg}\right) f_r + \frac{Wa_y s_o}{2g\rho'} - \frac{\mu_t Wl}{4B}\left[1 - \left(\frac{a_y}{g\mu_t}\right)^2\right] \tag{3.40}$$

3.4 DC Motor Model

As mentioned earlier, the TAGV employ permanent magnet DC motors to provide power to the tracks through a gearbox. The full derivation of the equations of motion of the motors is provided in Appendix *A* in Laplace form. With reference to these equations, considering that the controlled input is the armature voltage $E_a(s)$, and that the motor output is the angular displacement $\theta(s)$, the open-loop DC motor model can be represented in block diagram form as shown in Figure 3.6, where the symbols are as given in the appendix.

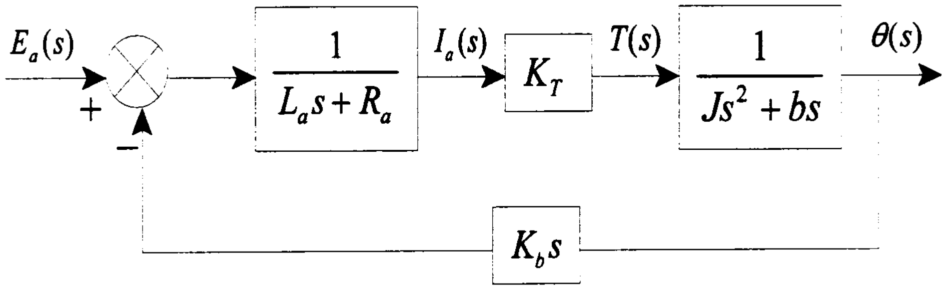

Figure 3.6: DC motor model

In general, DC motors are designed with the armature inductance L_a being very small when compared to the armature coil resistance R_a in order to increase the motor torque and reduce the back EMF. Assuming this to be the case here, the motor transfer function obtained from the block diagram shown in Figure 3.6 is as follows:

$$\frac{E_a(s)}{\theta(s)} = \frac{K_m}{s(T_m s + 1)} \tag{3.41}$$

where $K_m = K_T \,/\, (R_a b + K_T K_b)$ is the motor gain constant

$T_m = R_a J \,/\, (R_a b + K_T K_b)$ is the motor time constant

It should be noted that in this derivation the inertia and losses due to the load are reflected onto the motor side through a gearbox as shown in Appendix *A*.

3.5 TAGV System Model

A high level block diagram of the TAGV system model is shown in Figure 3.7. The model shows the DC motors and their low level controller submodel as a track drive system. The DC motors driving the left and right tracks of the vehicle are identical and their angular velocities are controlled by the low level controller. Equation 3.41 represents each of the DC motors shown in the figure. The feedback angular velocity of each motor is measured by a wheel/motor sensor [7] which is an optical encoder in this work. The low level controllers are SISO variable structure controllers. The structure of the controllers and a proposed design approach are presented in the following chapter.

The tracked vehicle dynamics and kinematics including the track drive system symbolize the vehicle submodel. The track-terrain interaction dynamics is included in this model as has been discussed and derived earlier. The "Vehicle Dynamics and Kinematics" block is shown in Figure 3.7. A cross-coupling between the left and right tracks exists as can be seen from Equations 3.39 and 3.40. The equations include the slip or skid coefficients between the track and the ground as has been explained earlier. For simulation purposes, the actual output path of the vehicle is generated by Equations 3.4-3.7.

Figure 3.7 also shows the vehicle navigational system which includes the desired input path, the actual output path of the vehicle, the high level path planning controller, and the vision-based navigational system.

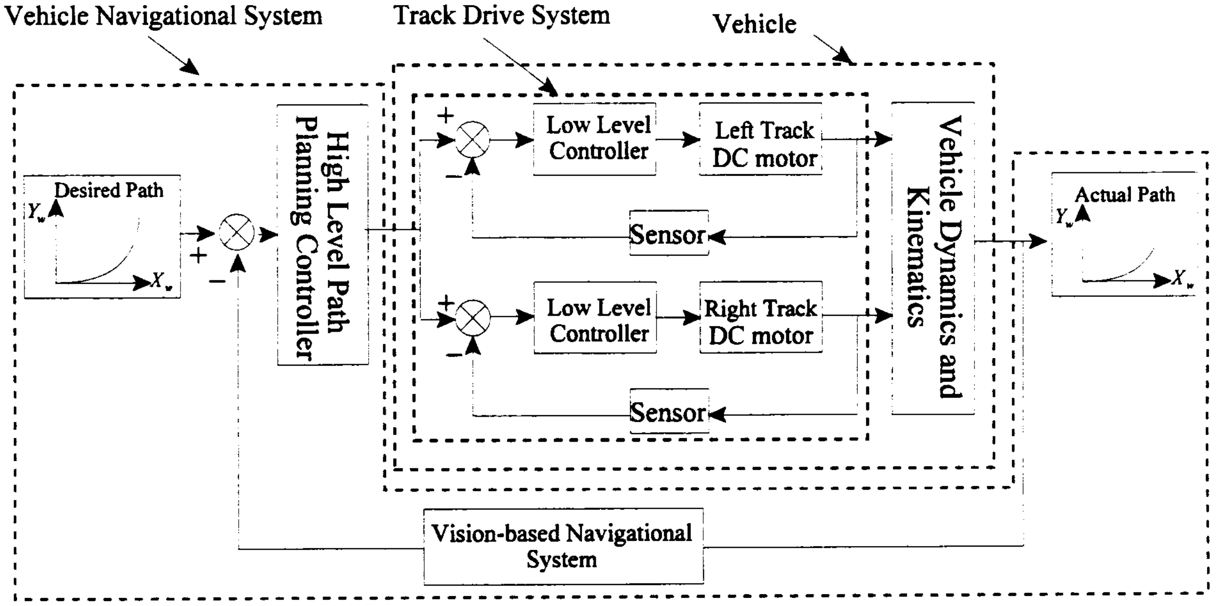

Figure 3.7: TAGV model

In order to be able to employ a controller that will drive the TAGV to the target pose, a feedback signal corresponding to the output pose of the vehicle has to be provided. A vision-based system is proposed in this work for navigation. The vision system is developed by [34] and its functionality is simulated for purposes of this work. The camera in this system looks ahead of the vehicle and extracts information about the current pose of the vehicle from quantified scene features, as well as information about the desired path. Due to the nonholonomic dynamics of the vehicle, a navigational manoeuvre would be required to correct a pose error and cause the vehicle to join and track the desired path at a target point ahead on the desired path. The high level controller algorithm determines such a viable path between the current pose of the vehicle and the target pose. The time required to execute the planned path is a function of the speed of the vehicle. The time required for the vision system to acquire and process the scene information to determine the current and the target poses is not a control system time delay in the conventional sense since the target pose is not expected to be reached till a future time. It should be noted however that if the time required to inquire and process the information is larger than the time to transverse the planned path between the current and the target poses, then the difference would be a control system time delay that might result in unstable response.

With reference to Figure 3.7, the desired input pose is compared to the output pose. The error is used to generate the high level control command through a SIMO variable structure controller. The structure and proposed design methodology of that controller is the subject of a later chapter. The control commands generated are the inputs of the low level motor controllers.

Chapter 4

Energy Based Design Procedure for Sliding Mode Controllers

4.1 Introduction

The physical parameters of the TAGV remain practically invariant during its operation. However, the interface parameters between its tracks and the ground vary considerably and often during its navigational mission. For example, the skid and slip parameters of the track/ground interface are significantly different when the ground is tile, carpet, and synthetic (polymeric) tiles or sheets. Even within the same generic type of flooring like carpets, the make and wear condition has significant effect on these parameters. The interface parameters are highly nonlinear and have the most significant effect on the TAGV performance. Consequently, a suitable controller for the TAGV must be able to react fast to large and very frequent changes in the operating conditions of the system, and be highly stable and robust.

Adaptive controllers were considered. Two primary types of adaptive controllers are common, namely; Model Reference Adaptive Controllers (MRACs) and Model Identification Adaptive Controllers (MIACs). Model reference adaptive controller compares the output of a reference model of the plant to the actual output and uses the results to re-tune the system controller parameters. On convergence, the optimum controller parameters would be found that cause the actual system output to match that of the reference model. Model identification adaptive controller uses a system identification module that has access to the control signal and the actual plant output and that attempts to identify system parameter uncertainties. An adjustment mechanism uses these parameters to re-tune the controller. In general, adaptive controllers are very effective when dealing with uncertainties in the system parameters and operating conditions. They are also very effective when these parameters or operating conditions undergo changes provided the changes are gradual and slow, or provided that sufficient time is allowed to ensure convergence before more changes occur. In the case of the practical application of the TAGV subject matter of this thesis, changes in track/ground interface parameters are large and rapid which preclude the use of adaptive controllers as a viable option.

As has been discussed earlier, one of the most important attributes of SMC is its simplicity of implementation and its robustness. Its major drawback stems from the difficulty of realization or design. The literature review shows that while a number of methods have been proposed, they all suffer from the arbitrary nature of choosing the sliding surface, a critical step in determining the performance of the SMC. In this chapter the theory and design methodology for the complete design of SMCs, including a reasoned approach for determining the sliding surface, are derived. To examine the performance of this new design methodology, it is applied to a SISO system. The DC motor model derived in Chapter 3 represents a SISO system. Finally, a classical proportional controller is applied to the DC motor and compared with the SMC new design methodology results.

4.2 An Example of a Variable Structure System

In order to understand the basic concept of variable structure control systems, assume the following simple example of a second order system [15]:

$$\begin{aligned} \ddot{x} &= a\dot{x} + u, \qquad a > 0 \\ u &= -kx \end{aligned} \tag{4.1}$$

where u is the feedback control signal.

The eigenvalues or the poles of the closed-loop system given by Equation 4.1 are found to be:

$$\lambda_{1,2} = \left(a \pm \sqrt{a^2 - 4k}\right)/2 \tag{4.2}$$

Assume the controller gain k to be as follows:

$$|k| = b \tag{4.3}$$

where $b > a^2 / 4$.

Equation 4.3 shows that there are two possible cases corresponding to the sign of the control signal gain k, these are:

I. The first case is that when $k = b$ and results in two complex poles (λ_1, λ_2) with positive real parts. Figure 4.1 (a) shows the phase plane portrait of such a system structure. This structure has unstable equilibrium point focus at the origin and from any starting point the system plot in the phase diagram will spiral outwards to instability.

II. The second case is that when $k = -b$ and results in a structure that has two real poles, one positive, $\lambda_1 > 0$, and the other negative, $\lambda_2 < 0$. The phase portrait of this structure is shown in Figure 4.1 (b). With reference to the figure, the phase plot curves depend upon the starting conditions and shows a saddle equilibrium point at the origin.

Both structures are primarily unstable, however, note that in the second structure, a motion leading to stability can occur along the line corresponding to the stable pole $\dot{x} - \lambda_2 x = 0$, i.e., a motion which tends to the origin. Therefore, if a switching function is defined as:

$$s(x, \dot{x}) = x s_1 \tag{4.4}$$

where $s_1 = \dot{x} - \lambda_2 x$.

and the system switches between the two structures, shown in Figures 4.1 (a) and (b), on the lines $x = 0$ and $s_1 = 0$ according to the following switching control law:

$$k = \begin{cases} +b, & s > 0 \\ -b, & s < 0 \end{cases} \tag{4.5}$$

then, the resulting phase trajectory would be as shown in Figure 4.1 (c). It can be seen that by using the above defined switching law, the state trajectories of the two unstable structures replace each other on the lines $x=0$ and $s_1=0$. As a result, all trajectories would be oriented towards the line $s_1=0$ and a stable slide towards the origin occurs.

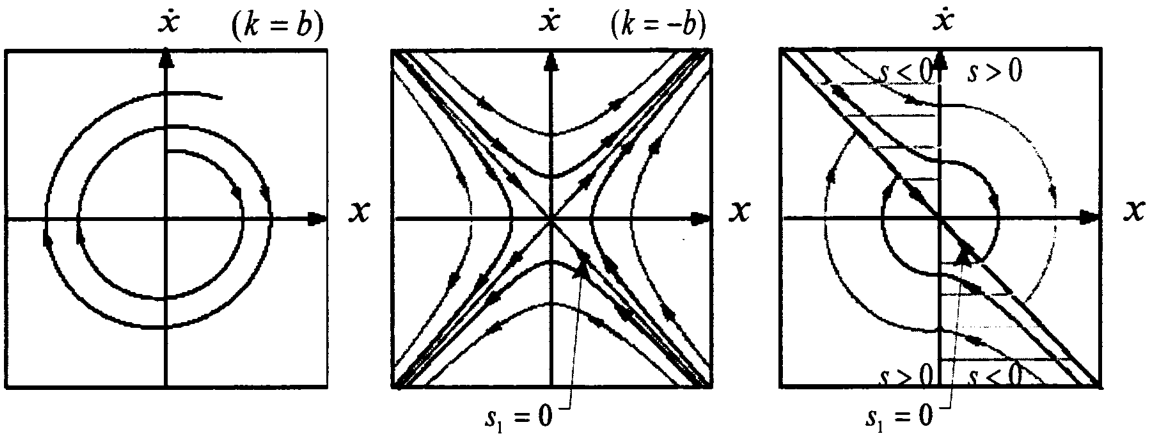

(a) (b) (c)

Figure 4.1: Asymptotically stable VSS consisting of two unstable structures

This example indicates that by switching between two structures, it is possible for a system to combine the useful properties of each. Moreover, new properties which are not present in any of the structures separately are attained [16]. Also, the example shows a new type of progression towards stability, which is the so called sliding mode. The line $s_1 = 0$ is called the switching or sliding surface. Different choices of the switching surface produce different system responses. In general, sliding mode arises along a trajectory which is not a trajectory of any of the involved structures. For more clarity, reconsider the following switching surface for the above example [15]:

$$\begin{aligned} s_1 &= \dot{x} + \lambda x \\ &= 0 \end{aligned} \tag{4.6}$$

where λ is the sliding surface slope and is measured in $\sec^{-1}$.

Figure 4.2 illustrates different system responses for different values of the slope λ. For $\lambda = |\lambda_2|$, by observing the dotted line trajectory in the figure, one can see that if the system state vector is perturbed at t_O below the line $s_1 = 0$, it will circle to the point t_1 before adjoining the switching line again. On the other hand, for $0 < \lambda < |\lambda_2|$, the line $s_1 = 0$ consists of the end points of the trajectories coming from both sides of the line, and thus any perturbation forcing the state vector off the line is always immediately forced back to the line since the phase plane velocity vectors always point towards the line. Thus the sliding mode may occur on this line.

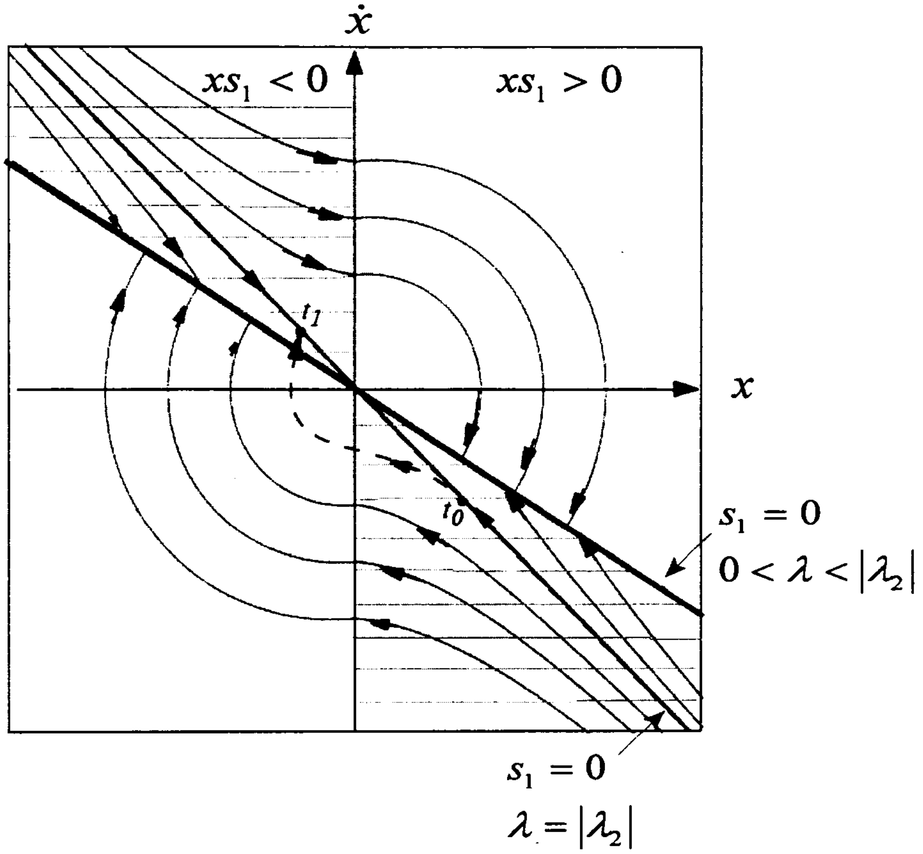

Figure 4.2: Path (doted line) of system state trajectory when perturbed below asymptotes

It can be seen that the condition for sliding mode to occur is that the structure of the system varies during the control phase, therefore the controller is named Variable Structure Controller (VSC). Since the sliding mode plays an important role, the control method is also referred to as Sliding Mode Controller (SMC). The discussion above shows that the phase plane trajectory of the resulting variable structure system consists of two modes: the reaching mode and the sliding mode. In the reaching mode, a trajectory starts from anywhere on the phase plane and moves towards the switching surface; where in the sliding mode the trajectory asymptotically tends to the origin along the surface $s_1 = 0$. These two modes are key elements of designing a SMC as shown in Appendix *B*.

4.3 Drawback of the Current Methodologies of Designing SMC

Based on the reviewed literature in Appendix *B*, the typical design methodology of a SMC is divided into two separate phases. In the first phase the sliding surface is designed and in the second phase the switching feedback control law is designed. In the following sections, a number of important observations can be gleaned from the review.

***Observations on the Sliding surface design*:**

1. Approaches based on special transformations of the system equations (Equations B.11 and B.14) have the drawback of obscuring the physical form of the system and changing its original state space. This results in the definition of a sliding surface that may not be physically obvious.
2. When classical feedback control design methodologies are used for designing the sliding surface in the above mentioned approaches, the values of some parameters must be assumed in order to be able to design the sliding surface. No coherent approach is available to guide the choice of the parameters.

***Observations on the control law design*:**

1. To satisfy the reaching condition for a prespecified switching feedback control law mentioned in Appendix *B* (Equations B.24 and B.27), the values of some parameters must be assumed in order to be able to proceed with the design. Even though the control law is prespecified here, complex inequalities might result which must be solved to find the required control law parameters.
2. Using the hierarchical control method (Equation B.31) to design the control law involves solving a set of complicated inequalities (Equation B.32) and is generally a very difficult task.

The above stated observations underline the difficulties faced when designing a SMC. Moreover, none of the sighted methods provide a relationship between the control law parameters and the sliding surface parameters. These observations provided the impetus for looking for a new methodology to design a SMC. The proposed methodology and its underlying reasoning are provided below.

4.4 SMC and the Principle of Work and Energy

One method used for assessing the behavior and stability of a system is the phase plane analysis. The phase plane of a system is a two-dimensional plot where the abscissa is the displacement and the ordinate is the velocity, i.e., the plot relates the system velocity to its displacement. Based on the system dynamics, the phase portrait is constructed by generating motion trajectories corresponding to different initial conditions. Consider the conservative spring-mass system shown in Figure 4.3 (a). If a step input displacement is applied to the body, potential energy is stored in the spring. Upon release, the potential energy is gradually converted to kinetic energy as the body accelerates. The continual interchange between potential and kinetic energy causes the body to oscillate. The kinetic energy of the body depends on its speed while the potential energy stored in the spring depends on the applied displacement on the spring. Hence, the ordinate of a system phase portrait can be viewed as a proxy of the kinetic energy and the abscissa can be viewed as a proxy of the potential energy. The total energy of the system shown in the figure is given by:

$$\frac{1}{2}kx^2 + \frac{1}{2}m\dot{x}^2 = E \tag{4.7}$$

where E is the total energy of the system and k is the spring constant.

Rearranging Equation 4.7 gives:

$$\frac{x^2}{a^2} + \frac{\dot{x}^2}{b^2} = 1 \tag{4.8}$$

where,
$$a = \sqrt{\frac{2E}{k}}$$
$$b = \sqrt{\frac{2E}{m}}$$

Equation 4.8 is that of an ellipse. Smaller ellipses represent smaller energy levels. Figure 4.3 (b) shows a scaled phase plane portrait of such an undamped system. In this portrait, the abscissa is scaled by $1/a^2$ and the ordinate is scaled by $1/b^2$. The ellipses corresponding to different initial conditions E_i. Studying the stability of this system can be carried out by examining the shape of the trajectories. The phase portrait in the figure shows that the system trajectories neither converge to the origin nor diverge to infinity since the system has no dissipative element, and its energy level remains constant. A phase plane portrait that converge to the origin indicates a stable system with decreasing energy level and a phase portrait diverging to infinity indicates an unstable system with increasing energy level as shown in Figure 4.4 (a) and (b) respectively.

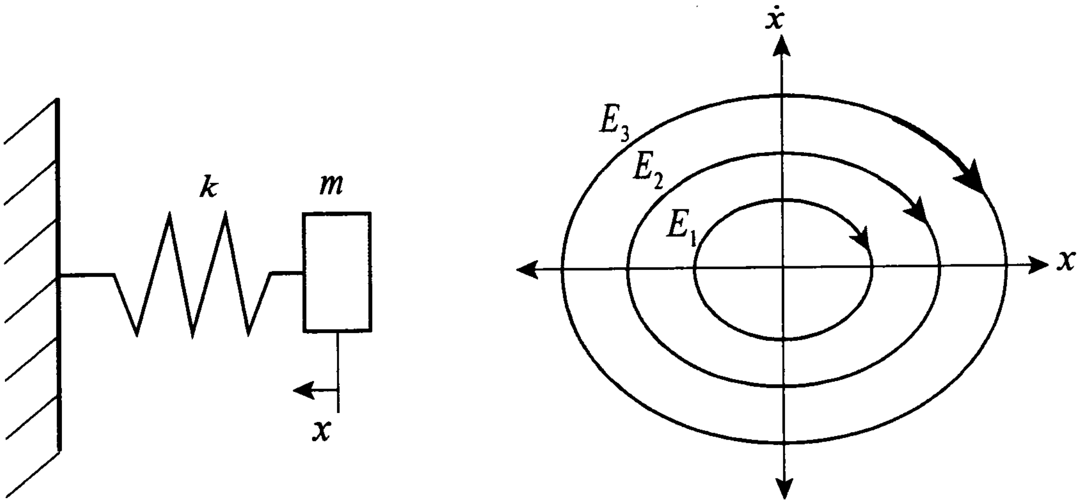

(a) (b)

Figure 4.3: Spring-mass system phase portrait. (a) System. (b) Phase portrait

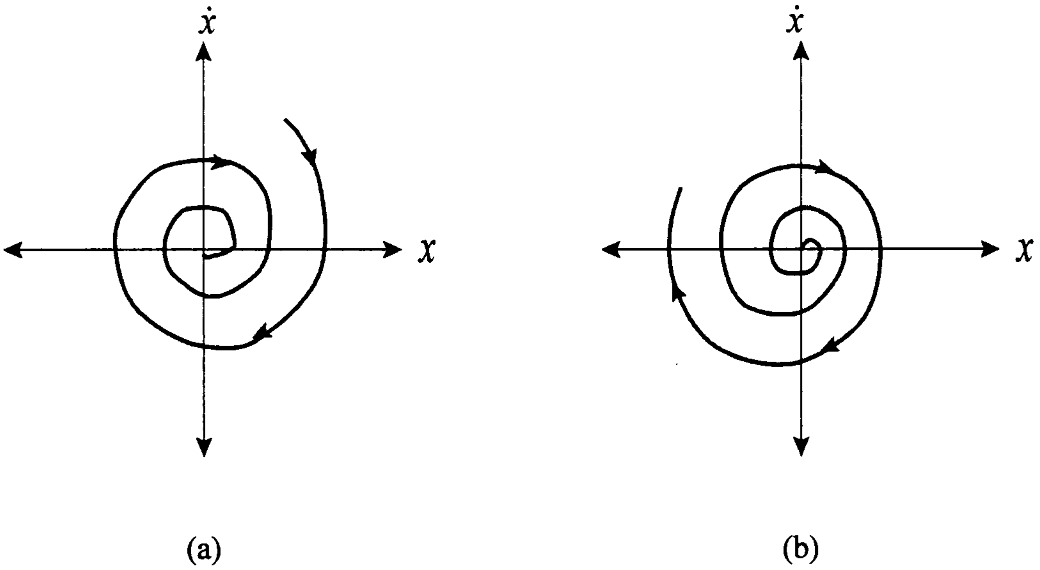

(a) (b)

Figure 4.4: Phase portrait of linear systems. (a) Stable. (b) Unstable

A dynamic system is considered stable if its total energy decreases asymptotically with time till it reaches its minimum value at the equilibrium state. Lyapunov exploited this fact in his stability criteria for dynamic systems. His approach requires the determination of the Lyapunov energy function, be it a true representation of the energy of the system, or a proxy for it. If the time derivative of the Lyapunov energy function is negative definite, then the energy is decreasing with increasing time and the system is said to be asymptotically stable.

In control engineering, given a simplified control system like that shown in Figure 4.5 as an example, a change in the set point $R(s)$ is tantamount to shifting the stability state from *0* on the phase plane portrait to *A* as shown in Figure 4.6. *A* now represents the current, previously stable, energy level of the system, and *0* represents the new stable state. Since *0* represents the minimum energy level of the system required for stability, it follows that the controller action will appear like it will have to dissipate energy equivalent to that between *A* and *0*.

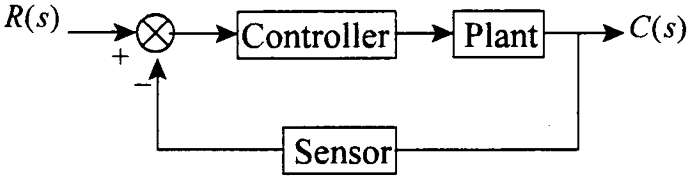

Figure 4.5: General control system

The controller action to dissipate energy can not occur along a path strictly on the *x*-axis of the phase plane. An infinite number of paths exist that would lead the system from the state represented by *A* to that represented by *0*. Paths that remain exclusively in the upper left quadrant, Figure 4.6 (a), correspond to overdamped response. Paths that traverse the $\dot{x}$ -axis, Figure 4.6 (b), correspond to underdamped response.

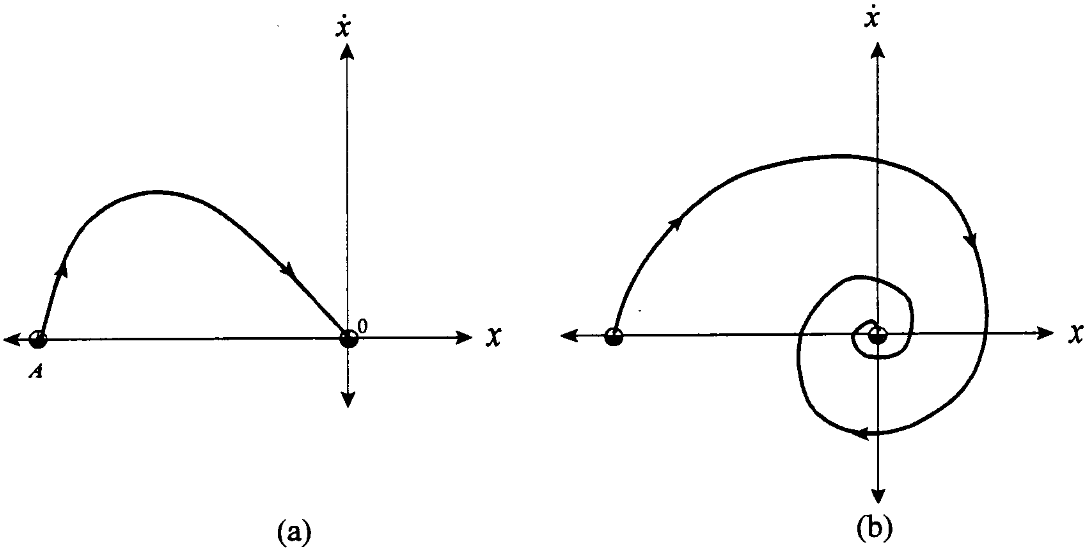

Figure 4.6: Phase portrait of linear systems. (a) Overdamped. (b) Underdamped

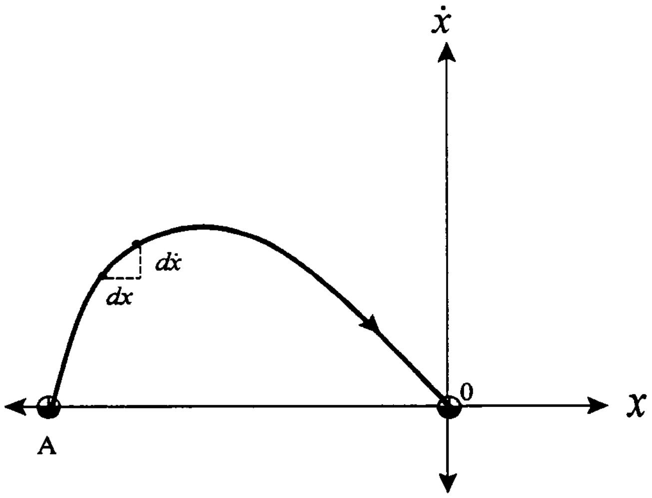

Figure 4.7: Reaching time to equilibrium state

The aim of a controller is to reach the set point in as little time as possible and preferably without an overshoot. With reference to Figure 4.7, the time required to traverse an infinitesimal reduction in energy along the path from *A* to *0* is calculated as follows:

$$\begin{aligned}\int_A^0 \dot{x}(x)dx &= \int_A^0 \frac{dx}{dt}dx \\ &= \frac{\int_A^0 \int_A^0 dx\, dx}{\int_A^0 dt}\end{aligned} \tag{4.9}$$

Rearranging Equation 4.9 gives:

$$\begin{aligned}\int_A^0 dt &= \frac{\int_A^0 \int_A^0 dx\, dx}{\int_A^0 \dot{x}(x)dx} \\ t\big|_A^0 &= \frac{(x_0 - x_A)^2}{\int_A^0 \dot{x}(x)dx}\end{aligned} \tag{4.10}$$

Equation 4.10 shows that to reach the equilibrium state in a minimum time, $\int_A^0 \dot{x}dx$ has to be maximum.

A conventional system controller can be tuned such that the system response is critically damped. Then, generally speaking, the system response should reach true steady state faster than that with other tuning conditions. Determining the tuning conditions that would result in critical damping for a second order time invariant system is relatively easy. For higher order systems, the problem becomes more difficult and would be impossible in the case of time varying or nonlinear systems.

For any control system, a single structure controller can be designed to allow energy to flow in one direction only. This will result in an overdamped system. The phase plane portrait will remain in the second quadrant. Such a controller will not be optimal. Utkin showed in [16] that a variable structure controller can be designed such that the phase plane portrait of the system will have a higher $\dot{x}$ yet remains entirely in the second quadrant. The energy based design methodology of such a controller is the subject of the next sections.

4.5 SMC Design Technique based on the Principle of Work and Energy

With reference to the phase plane portrait shown in Figure 4.8, assuming a controller acting to move a mechanical system from one state (1) to another (2) in the presence of a dissipative viscous load. The work done by the controller $U_{1\to 2}$ less that consumed by the dissipative load $U_{R(1\to 2)}$ is related to the energy of the system as follows:

$$T_1 + V_1 + U_{1\to 2} = T_2 + V_2 + U_{R(1\to 2)} \tag{4.11}$$

where,

T_1, V_1 are the kinetic and potential energy of the system at position (1)

T_2, V_2 are the kinetic and potential energy of the system at position (2)

$U_{1\to 2}$ is the work done by the controller between the two positions

$U_{R(1\to 2)}$ is the work lost to the viscous damper between the two positions

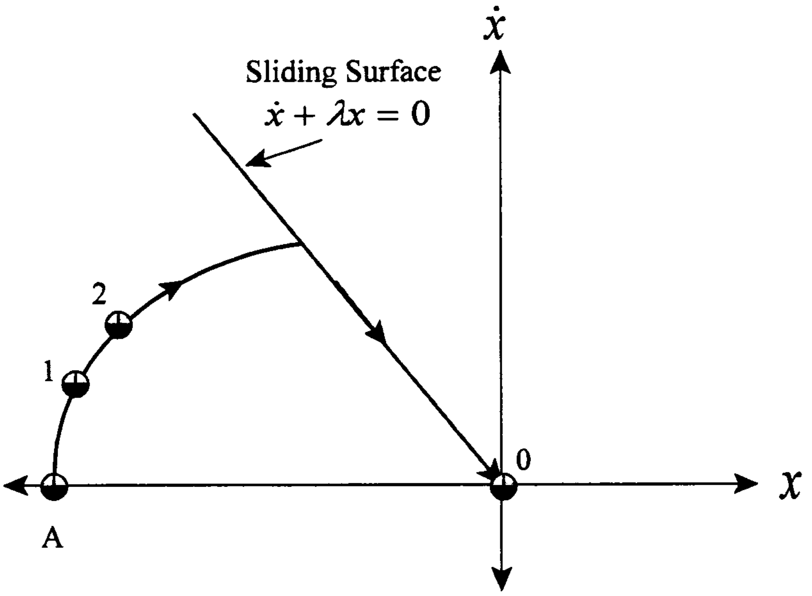

Figure 4.8: Sliding mode motion

Assuming a mechanical system and substituting for the kinetic energy, the potential energy, and the work done components of Equation 4.11 gives:

$$\frac{1}{2}\beta(\dot{x}_2^2 - \dot{x}_1^2) + \frac{1}{2}\alpha(x_2^2 - x_1^2) - \Gamma(\dot{x}_2 x_2 - \dot{x}_1 x_1) - k(x_2^2 - x_1^2) = 0 \tag{4.12}$$

where ,

β	is equivalent to an inertia
α	is a constant corresponded to the potential energy equivalent to a spring constant
Γ	is equivalent to a damping coefficient
k	is the controller gain

In order to calculate the controller gain k that would force the system to change state from (1) to (2), the system parameters α , β, and Γ must be known.

Consider the case when the system discussed above is one with the following differential form:

$$m\ddot{x} + b\dot{x} + k_s x = u \tag{4.13}$$

where m, b, and k_s are the mass, damping coefficient, and spring constant respectively. u is the controller force.

The work done by the controller between (1) and (2) in this case is given by:

$$\int_1^2 m\ddot{x}dx + \int_1^2 b\dot{x}dx + \int_1^2 kxdx = \int_1^2 udx \tag{4.14}$$

but

$$\begin{aligned} \ddot{x} &= \frac{d\dot{x}}{dx}\frac{dx}{dt} \\ &= \dot{x}\frac{d\dot{x}}{dx} \end{aligned}$$

and $u = kx$

Hence, Equation 4.14 can also be written as:

$$\int_1^2 m\dot{x}d\dot{x} + \int_1^2 b\dot{x}dx + \int_1^2 k_s xdx = \int_1^2 kxdx \tag{4.15}$$

Integrating Equation 4.15 and applying the limits gives:

$$\frac{1}{2}m(\dot{x}_2^2 - \dot{x}_1^2) - b(\dot{x}_2 x_2 - \dot{x}_1 x_1) + \frac{1}{2}k_s(x_2^2 - x_1^2) = \frac{1}{2}k(x_2^2 - x_1^2) \tag{4.16}$$

Comparing Equations 4.12 and 4.16 shows that:

$$\beta \equiv m,\ \alpha \equiv k_s, \text{ and } \Gamma \equiv b$$

It is clear that for a given control system, if Equation 4.12 is considered, the coefficients α, β, and Γ can be found by comparing Equation 4.12 and the differential equation describing the system behavior.

If Equation 4.12 is rewritten in the following form:

$$\frac{1}{2}\beta\dot{x}^2+\frac{1}{2}\alpha x^2-\Gamma\dot{x}.x-kx^2=0 \tag{4.17}$$

Assuming the system is on the sliding surface shown in Figure 4.8. The sliding surface $s=0$ is a straight line passing through the origin and is given by:

$$\begin{aligned} s &= \lambda x+\dot{x} \\ &= 0 \end{aligned} \tag{4.18}$$

Substituting for $x=-\dot{x}/\lambda$ from Equation 4.18 into Equation 4.17 and rearranging results in:

$$\frac{1}{2}\beta\dot{x}^2+\frac{1}{2\lambda^2}\alpha\dot{x}^2+\frac{1}{\lambda}\Gamma\dot{x}^2=\frac{1}{\lambda^2}k\dot{x}^2 \tag{4.19}$$

Cancelling similar terms from both sides and rearranging gives:

$$k=\frac{1}{2}(\beta\lambda^2+\alpha)+\Gamma\lambda \tag{4.20}$$

Equation 4.20 provides a relationship between the slope λ of the sliding surface $s=0$ and the control law gain k. This equation provides a mean for calculating the value of the control law gain based on a given value of the sliding surface slope. However, the gain and the slope are governed by the system capabilities.

4.6 SMC Stability

As has been outlined earlier in Section 4.2, a SMC causes the transition of the system state from the initial to the final required state along two very distinct phases. In the first, reaching phase, the goal is to cause the system state to reach the sliding surface as fast as possible. Any stable conventional controller may be used for this phase. The efficiency of the entire SMC, however, is affected by that choice and the speed by which that controller causes the system state to reach the sliding surface. In Section 4.2 and in view of the discussion in Section 4.4, it was shown that during the second phase, the sliding phase, the system state undergoes a transition from a higher total energy level to lower ones asymptotically until the target state is reached. Hence, it is sufficient to show that for a system controlled by a SMC, the stability can be assured by studying the reaching state. The stability analysis of this section is valid for second order systems.

In this work, a proportional controller is used during the reaching phase. Consequently, stability of the system can be studied by evaluating the pole placement of the entire system in the s-plane. Provided that the system poles do not cross into the right hand side of the s-plane, the system would be stable and its total energy would be decreasing till it intersects the sliding surface. Beyond that point, the switching logic of the SMC would ensure asymptotic decay of energy, and hence stability. The stability issue of the proposed controller can also be verified using Lyapunov stability criteria. Lyapunov stipulated that the stability of a system is guaranteed if the total energy of the system is continuously dissipated. Lyapunov proposed defining a proxy function for the energy of the system and examining this function to assess stability. The function must be positive definite and has continuous partial derivative. If the time derivative of the energy function along any state trajectory of the system is locally negative definite, then the stability of the system is asymptotic. With reference to the previous section, the following function is a good candidate for a Lyapunov function:

$$V = \frac{1}{2}\beta\dot{x}^2 + \frac{1}{2}\alpha x^2 \tag{4.21}$$

Taking the time derivative of Equation 4.21 gives:

$$\dot{V} = \dot{x}[\beta\ddot{x} + \alpha x] \tag{4.22}$$

Substituting for $\ddot{x}$ from Equation 4.13 results in:

$$\dot{V} = \dot{x}x\left[\frac{\beta}{m}(k - k_s) + \alpha\right] - b\dot{x}^2 \tag{4.23}$$

Noting that $u = kx$.

In the reaching mode, the system is in the second quarter of the phase portrait of the system as shown in Figure 4.8. This mean that the term $x\dot{x}$ of Equation 4.23 is negative. Hence, Equation 4.23 is negative definite if and only if $k > k_s$ and as a result the stability of the system is guaranteed in the reaching mode.

To analyze the stability in the sliding mode, substitute x from Equation 4.18 into Equation 4.21 to obtain the following equation:

$$V = \frac{1}{2}\beta\dot{x}^2 + \frac{1}{2\lambda^2}\alpha\dot{x}^2 \tag{4.24}$$

Taking the time derivative of Equation 4.24 results in:

$$\dot{V} = \xi\dot{x}\ddot{x} \tag{4.25}$$

where $\xi = \beta + \frac{1}{\lambda^2}\alpha$ is constant.

Substituting for $\ddot{x}$ and x from Equations 4.13 and 4.18 respectively into Equation 4.25 gives:

$$\dot{V} = -\left[\frac{\xi}{m}b\dot{x}^2 - (k - k_s)\frac{\dot{x}^2}{\lambda}\right] \tag{4.26}$$

Equation 4.26 is negative definite if and only if $k > k_s$. This is guaranteed if Equation 4.20 is used to find the controller gain k. Hence, choosing the controller gain based on Equation 4.20 and selecting $k > k_s$ results in an asymptotically stable system.

The stability of the particular SMCs designed throughout the work will be addressed in the individual sections dealing with them.

4.7 Comparison Between a Sliding Mode Controller and a Proportional Controller

In this section, a comparison is made between a SMC and a Proportional (P) controller based on the system response. Consider the general control system given in Figure 4.5. Assume the plant has the following fourth order form:

$$G(s) = \frac{1}{s(s^3 + 5s^2 + 8s + 6)} \tag{4.27}$$

For a unity-feedback gain and a proportional controller, the system response $c(t)$ for a step input $r(t)$ is critically damped if the gain of the controller is chosen to be $k = 1$. Increasing the controller gain to $k = 4$, as an example, results in an underdamped response as shown in Figure 4.9. A faster overdamped response can be obtained by using a SMC with a linear sliding surface passing through the origin and a relay type control law. Figure 4.9 shows different response patterns for proportional controller with gains of 1 and 4, and SMC with gains of $k = \pm 4$ but for different sliding surface slopes λ. The corresponding phase portraits of the systems are shown in Figure 4.10. In all cases, the SMCs exhibit superior performance to proportional controllers. The proportionally controlled systems exhibit classical critically damped and underdamped responses for $k = 1$ and $k = 4$ respectively. Settling times for systems controlled using SMCs decrease with the increase of the slope of the sliding surface up to $\lambda = 0.85\,\mathrm{sec}^{-1}$ and then increase as the response oscillates about the set point. This can be clearly seen from the phase plane portraits of the responses where for the oscillatory systems the curves circle about the origin. The response of the system controlled using a SMC with a slope $\lambda = 0.5\,\mathrm{sec}^{-1}$ clearly shows the effect of the sliding surface. As the state of the system crosses the sliding surface, the controller changes structure and attempts to reverse the progression of the system response. In Figure 4.9 this is manifested by the oscillations in the response. In Figure 4.10 this is manifested by the acceleration and deceleration of the system response as it crosses the sliding surface. At a high slope $\lambda = 1\,\mathrm{sec}^{-1}$, for example, the system state crosses the sliding surface at high velocity. The system in this case has a high kinetic energy, and the structure of the controller is unable to brake the system before it passes the set point.

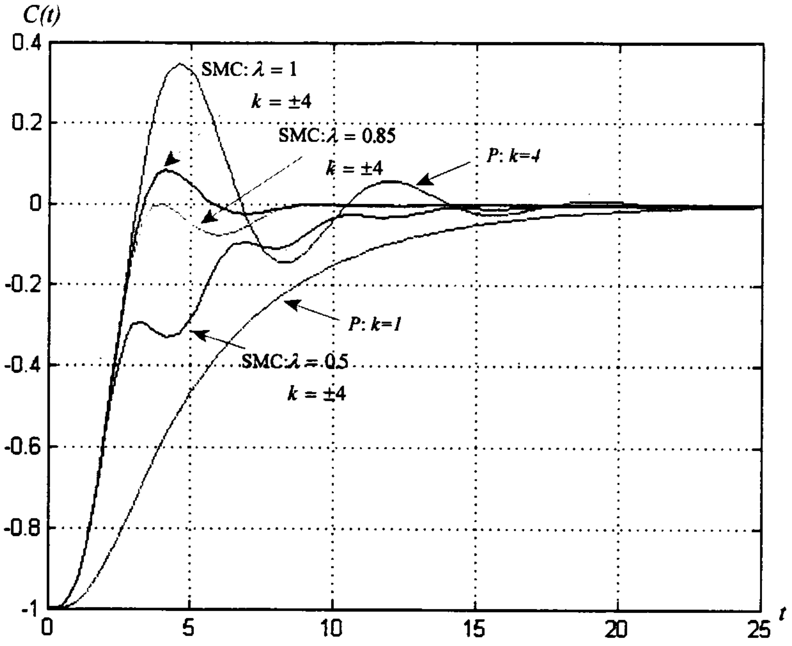

Figure 4.9: Fourth order system response for P-controller and SMC

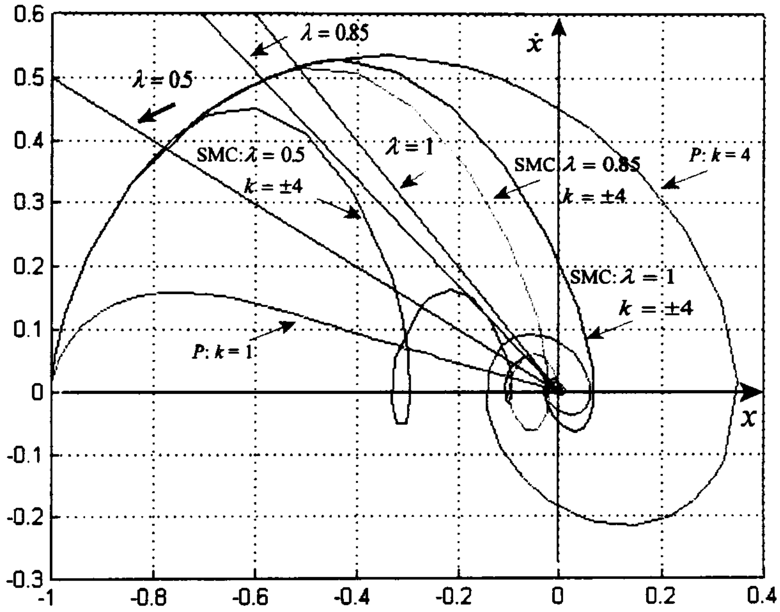

Figure 4.10: Fourth order system phase portrait for P-controller and SMC

To study the effect of change in system parameters, assume the plant in Figure 4.5 to have the following transfer function:

$$G(s) = \frac{55}{as^2 + s} \tag{4.28}$$

The original system has the parameter $a = 0.13$. Assume the value of a changes during operation to 0.10. Figure 4.11 shows plots for three proportionally controlled unity-feedback system responses with gains of 1, 2, 5 and for both cases $a=0.13$ and $a=0.10$ when subjected to step inputs. Similar to the fourth order system explained earlier, a faster overdamped response can be obtained by employing a SMC and a relay type control law. The response of the system for a SMC with switching gains $k = \pm 5$ and sliding surface slope $\lambda = 13\,\text{sec}^{-1}$ is shown in Figure 4.11 for both cases $a=0.13$ and $a=0.10$. The system responses show that the proportionably controlled systems are susceptible to parameter variations while the sliding mode controlled system does not seem to be affected by these changes and hence more robust. The corresponding phase portraits of the system are shown in Figure 4.12.

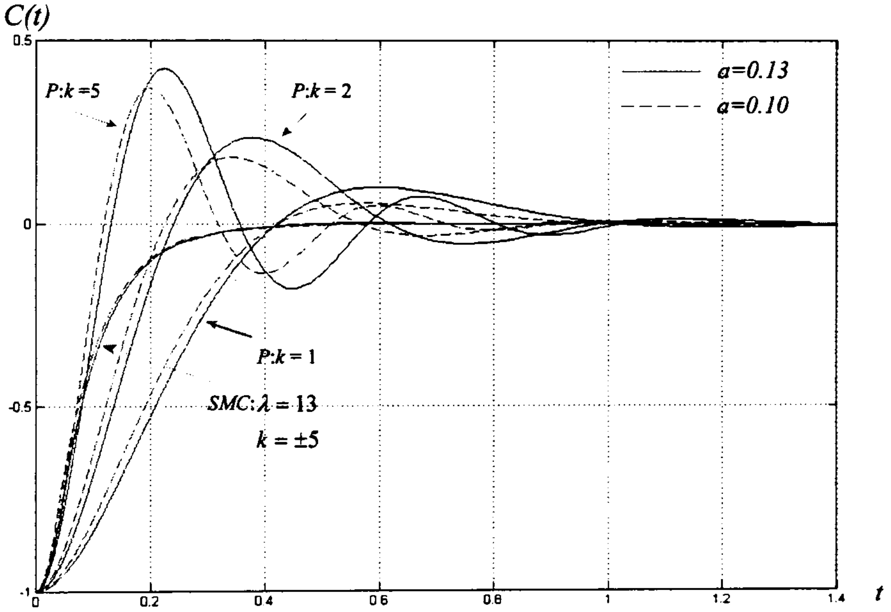

Figure 4.11: Second order system response for P-controller and SMC

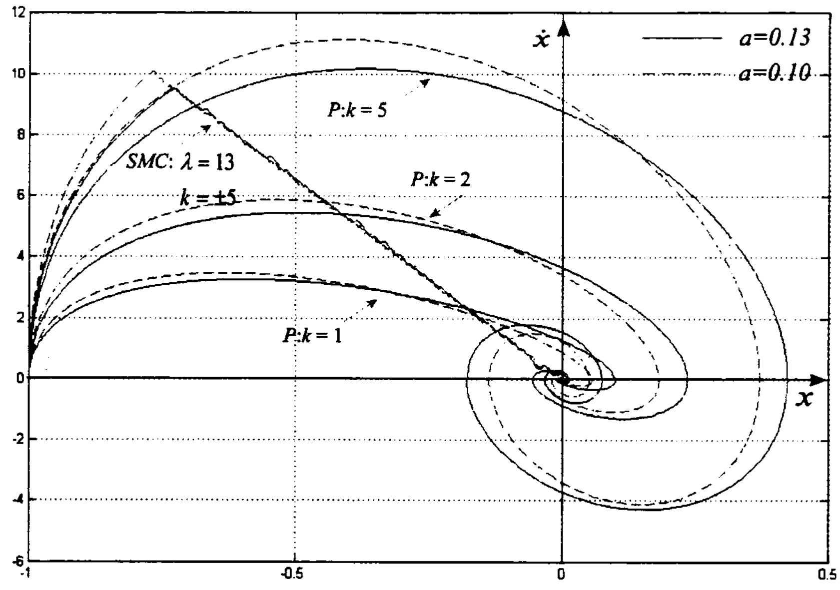

Figure 4.12: Second order system phase portrait for P-controller and SMC

4.8 DC motor Control

In order to examine the performance of the new design methodology of SMCs derived in Section 4.5, proportional and sliding mode controllers for the DC motor model derived in Chapter 3 are designed and their performance simulated. The block diagrams for the proportional and sliding mode controlled systems are shown in Figures 4.13 and 4.14 respectively.

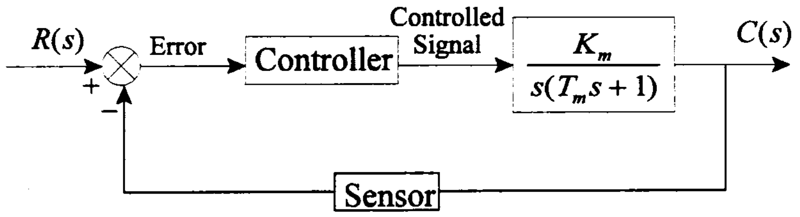

Figure 4.13: Closed-loop DC motor block diagram

4.8.1 Controller Design

The SMC is described by a linear sliding surface and a relay control law given by:

$$s = \lambda\theta + \dot{\theta} \tag{4.29}$$

$$u = \begin{cases} +k\theta, & s > 0 \\ -k\theta, & s < 0 \end{cases} \tag{4.30}$$

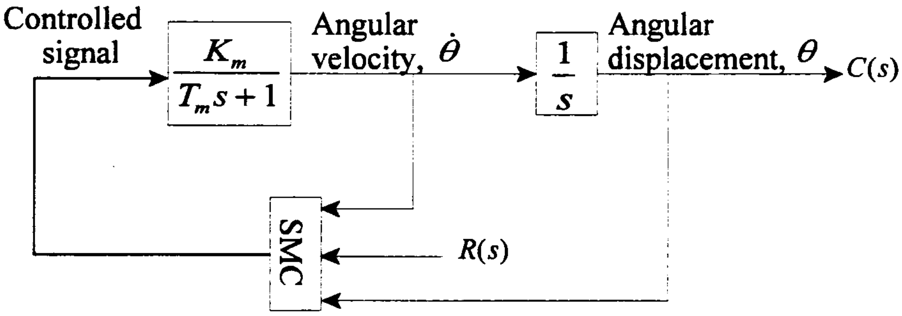

Figure 4.14: DC motor with SMC block diagram

With reference to Figure 4.13, the transfer function of the plant is given by:

$$\frac{\theta(s)}{E_a(s)} = \frac{K_m}{T_m s^2 + s} \tag{4.31}$$

In the time domain, the above equation becomes:

$$T_m\ddot{\theta} + \dot{\theta} + K_m e_a = 0 \tag{4.32}$$

With reference to Equation 4.20, the coefficients α, β, and Γ can be found by direct comparison as was done in the previous section, and are given as follows:

$$\beta = T_m$$
$$\alpha = 0 \tag{4.33}$$
$$\Gamma = 1$$

Hence, the relationship between the controller gain and the sliding surface slope in terms of the system parameters is given by:

$$k = \frac{1}{2} T_m \lambda^2 + \lambda \tag{4.34}$$

4.8.2 Simulation Results and Comparisons

In this section, a proportional controller and the new design methodology of the SMC are applied to the motor system for comparison. Table 4.1 shows the motor-load characteristics used in the simulation.

Table 4.1: Motor-Load characteristics

Motor and Load Characteristics

Rated voltage range, e_a	0-30 *Volt*
Rated current, i_a	6.1 *Ampere*
Back EMF constant, K_b	0.041 *Volt.Sec/rad*
Armature resistance, R_a	0.47 *Ohms*
Motor torque constant, K_T	0.041*N.m/Ampere*
Moment of inertia of the motor, J_m	$5 \times 10^{-5}\ kg.m^2$
Viscous friction coefficient of the motor, b_m	Negligible
Moment of inertia of the load, J_l	$50 \times 10^{-3}\ kg.m^2$
Viscous friction coefficient of the load, b_L	$10 \times 10^{-2}\ N.m/rad/\sec$
Gear ratio, n	1:16

With reference to the motor-load parameters given above and the derivation in Appendix *A*, solving for T_m and substituting in Equation 4.34 gives:

$$k = \frac{1}{2}0.018\lambda^2 + \lambda \tag{4.35}$$

The transfer function of the DC motor system when controlled using a SMC is given by Equation 4.31. The closed-loop pole placement of the system for the reaching phase when the system controller is configured as a proportional one is shown in Figure 4.15. The s-plane portrait of the system shows that the system is unconditionally stable for all values of gains. It was shown earlier that during the sliding phase, the energy level of the system decreases asymptotically. Hence, the designed system controlled using the SMC is stable.

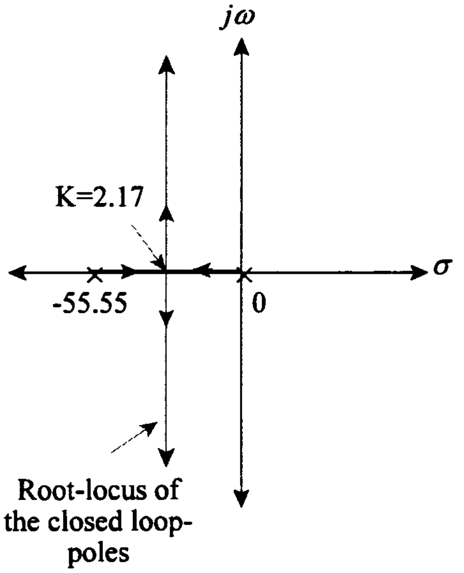

Figure 4.15: Root-locus diagram of the DC motor

Equation 4.35 shows that for any given slope of the sliding surface there is a corresponding value of the controller gain. However, the motor has a power limit which can be expressed by its speed-torque curve. Based on the motor equations provided in Appendix *A*, the relationship between the load torque *T* and the motor output speed $\dot{\theta}$ can be expressed as follows:

$$\dot{\theta} = \frac{1}{K_b} e_a - \frac{R_a}{K_b K_T} T \tag{4.36}$$

With reference to Equation A.4 in Appendix *A*, the torque *T* depends on the total inertia of the system as well as on its viscous friction. The effect of changing the inertia causes either an increase or decrease in the settling time of the speed response, whereas the effect of changing the friction causes either an increase or decrease in the resulting maximum speed of the motor.

Equation 4.36 is that of a straight line function of the speed $\dot{\theta}$ versus the torque *T* for a given supply voltage e_a . An example of the plot of the equation is shown in Figure 4.16.

Assume a dissipative damping load given by $T = b\dot{\theta}$, substituting for $\dot{\theta}$ into Equation 4.36 results in:

$$\dot{\theta} = \frac{1}{K_b} e_a - \frac{R_a b}{K_b K_T} \dot{\theta} \tag{4.37}$$

Rearranging Equation 4.37 gives:

$$\dot{\theta} = \frac{e_a K_T}{K_b K_T + R_a b} \tag{4.38}$$

Using the system parameters given in Table 4.1, the maximum rotational speed of the motor is calculated to be $\dot{\theta}_m = 560.3\ rad / \sec$. Noting that increasing the load decreases the speed. If the damping coefficient is increased to $b = 0.01\ N.m / rad / \sec$, the resulting maximum speed of the motor reduces to $\dot{\theta}_m = 154.21 rad / \sec$. The time required for the system to reach its maximum speed depends on the motor time constant T_m. In first order systems, the response reaches 98.2% of the final value at four times the time constant of the system. During the reaching phase, it is desired to let the system reach its maximum speed in as little time as possible as has been explained earlier. Hence, if the angular speed is considered to be the output of the system, then in this case the system is a first order one. Hence, the time required to reach 98.2% of the final value of the angular speed is $4T_m = 0.072 \sec$. This time translates to an angular displacement of $11.15 rad$ that the motor travels before the speed reaches its maximum value of $\dot{\theta}_m = 154.21 rad/\sec$. Figure 4.17 shows the phase portrait of the system in this case. Since it is always desired to minimize the time required for a controller to bring the system to the set point, then in this case it would be prudent to let the system reach this maximum speed. The minimum sliding surface slope in this case would be as shown in Figure 4.17. The angular displacement between *A* and *B* on the plot corresponds to the reaching phase of the SMC and that between *B* and *0* corresponds to the sliding phase.

Assume that the angular displacement for the sliding phase is $10 rad$, then with reference to Figure 4.17, the slope of the sliding surface can be calculated as follows:

$$\begin{aligned}\lambda &= \frac{\dot{\theta}_m}{\theta_d} \\ &= \frac{154.21}{10} \\ &= 15.42\sec^{-1}\end{aligned} \tag{4.39}$$

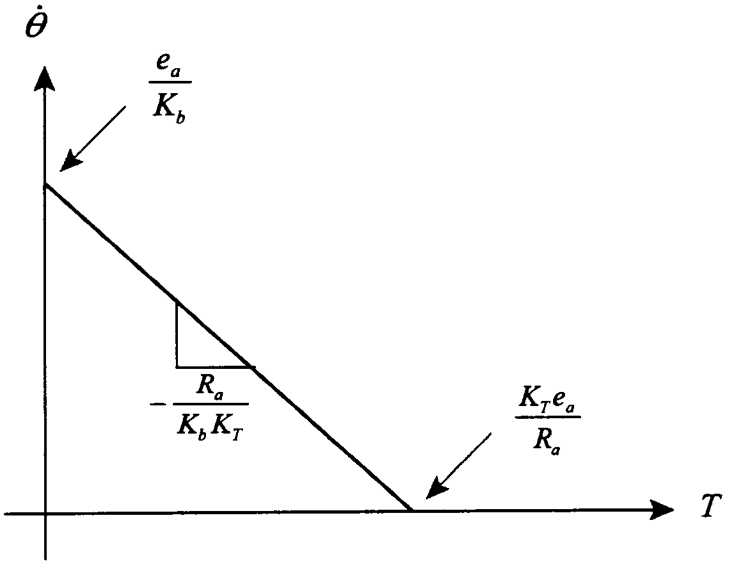

Figure 4.16: DC motor speed-torque curve

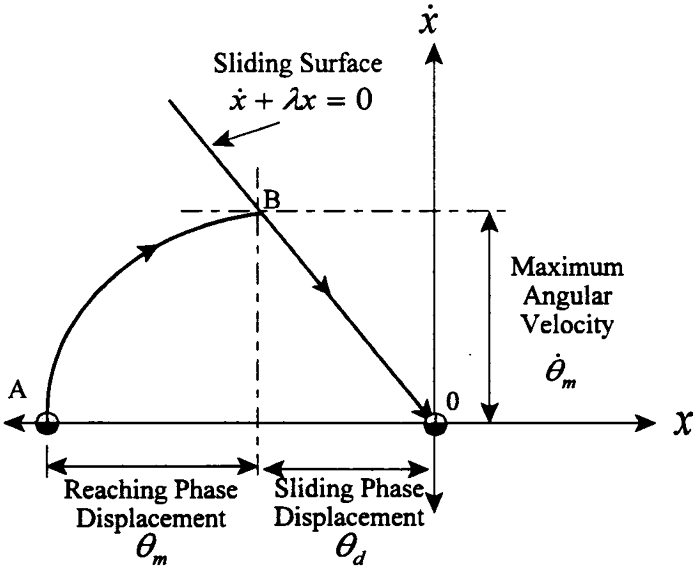

Figure 4.17: SMC limits

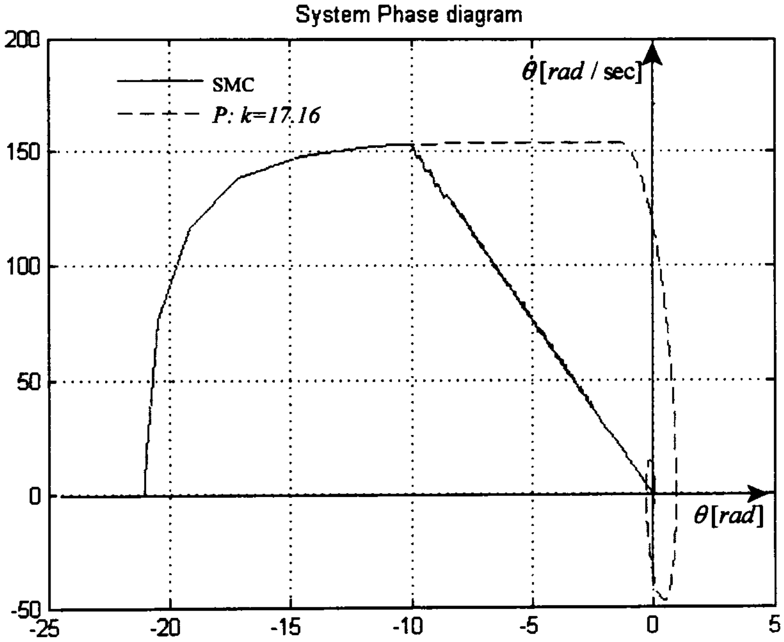

Figure 4.18: DC motor phase portrait with $\lambda = 15.42$

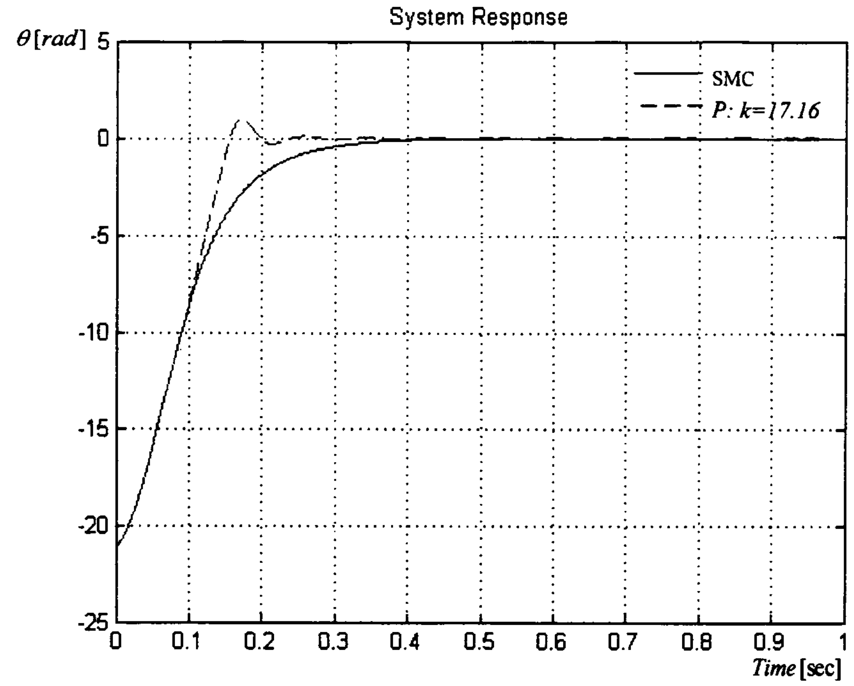

Figure4.19: DC motor response with $\lambda = 15.42$

Substituting Equation 4.39 into Equation 4.35 results in a controller gain $k = \pm 17.16$ of the SMC. Simulation results are shown in Figures 4.18 and 4.19. The figures show the phase portrait and the response of the system for both the proportional controller and the SMC. The value of the proportional controller gain is selected here to be $k = 17.16$ for reference purposes only. A performance comparison with a critically damped proportional controller, and two PD-controllers tuned based on Ziegler-Nichols tuning method [33] and MATLAB Control System Toolbox tuning is provided at the end of this section.

Figure 4.19 shows an overdamped response of the system for the SMC and underdamped response for the proportional controller. However, the SMC is not faster than the proportional controller while bringing the system to the equilibrium state. The response of the system for the SMC can be improved to reach the desired equilibrium state faster with less settling time by increasing the duration time that the system travels at the maximum speed $\dot{\theta}_m$. This improvement can be achieved by increasing the slope of the sliding surface. At the maximum speed, the load torque on the motor and the controller output must be matched, i.e,

$$b\dot{\theta} = k\theta \tag{4.40}$$

Substituting Equation 4.34 into Equation 4.40 results in:

$$b\dot{\theta} = \left(\frac{1}{2}T_m\lambda^2 + \lambda\right)\theta \tag{4.41}$$

When the system reaches the sliding surface, $\theta = -\dot{\theta}/\lambda$ is a valid condition and can be substituted into Equation 4.41 to give:

$$b\dot{\theta} = \left(\frac{1}{2}T_m\lambda^2 + \lambda\right)\left(-\frac{\dot{\theta}}{\lambda}\right) \tag{4.42}$$

Rearranging Equation 4.42 yields the sliding surface slope as follows:

$$\lambda = \frac{-2(1+b)}{T_m} \tag{4.43}$$

Substituting $T_m = 0.018\sec$ and $b = 0.01\ N.m/rad/\sec$ into Equation 4.43 results in $\lambda = 110\sec^{-1}$ at which the system response becomes optimum. Applying Equation 4.35for this slope gives $k = \pm 218.9$. Simulation results are shown in Figures 4.20 and 4.21. The figures show the phase portraits and the response of the system for the SMC, with $\lambda = 110\sec^{-1}$ and $k = \pm 218.9$, and the same proportional controller gain used earlier, i.e., $k = 17.16$. The results show that SMC performance of the SMC is better than that of the proportional controller.

Since the system decelerates as it moves on the sliding surface, the motor-load system Equation A.4 of Appendix A can be rearranged to give:

$$-d\dot{\theta} = \frac{T}{J}dt - \frac{b}{J}d\theta \tag{4.44}$$

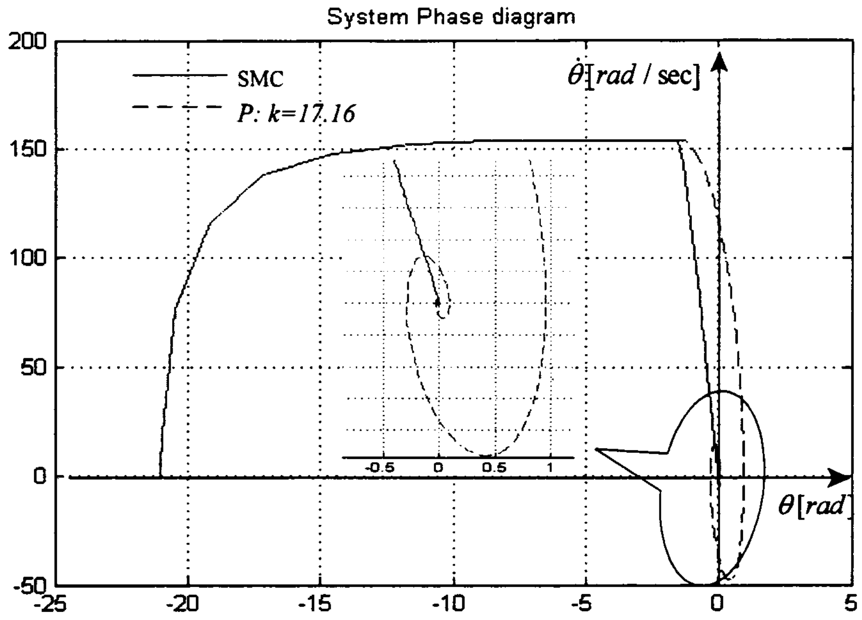

Figure 4.20: DC motor phase portrait with $\lambda = 110$

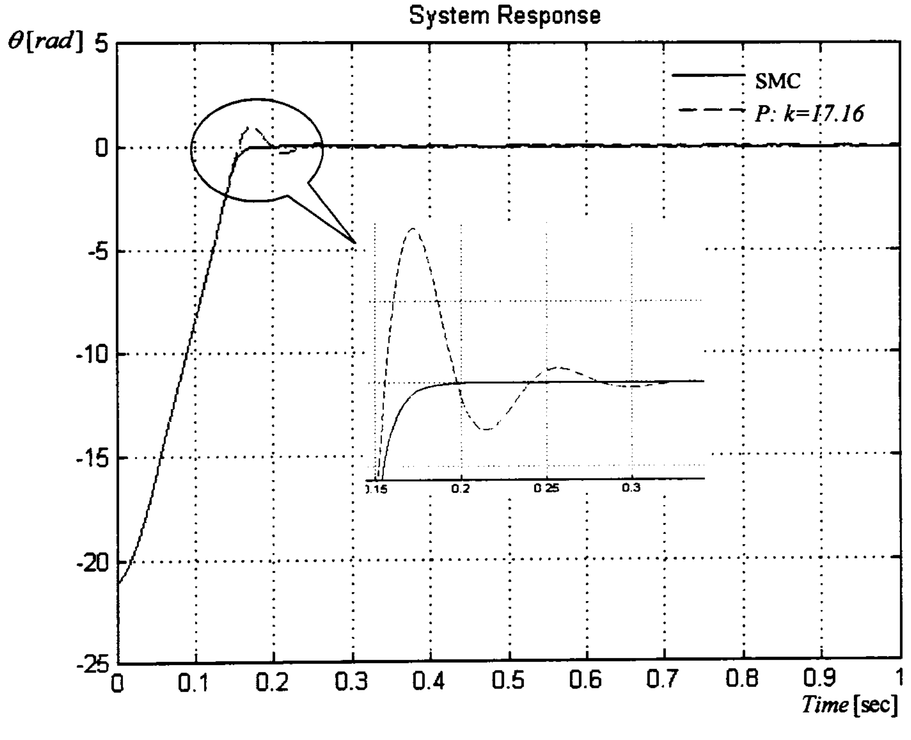

Figure 4.21: DC motor response with $\lambda = 110$

Substituting for the torque *T* from Equation 4.36 into Equation 4.44 gives:

$$-d\dot{\theta}=\frac{e_aK_T}{R_aJ}dt-\frac{K_bK_T}{R_aJ}d\theta-\frac{b}{J}d\theta \qquad (4.45)$$

Integrating both sides of the above equation between position *B* and *0* in Figure 4.17 yields:

$$\dot{\theta}_m=\frac{e_aK_T}{R_aJ}\Delta t-\left(\frac{K_bK_T}{R_aJ}+\frac{b}{J}\right)\Delta\theta \qquad (4.46)$$

where Δt and $\Delta\theta$ are the time required to reach the steady state, i.e., origin of the phase plot, and the corresponding displacement.

Since the sliding surface is considered linear in this work, the average velocity of travel along the sliding surface is $\dot{\theta}_m/3$. Hence, the time Δt can be found as follows:

$$\Delta t=\frac{\Delta\theta}{\frac{1}{3}\dot{\theta}_m} \qquad (4.47)$$

Substituting Equation 4.47 into Equation 4.46 results in:

$$\dot{\theta}_m=\left(\frac{3e_aK_T}{R_aJ\dot{\theta}_m}-\frac{K_bK_T}{R_aJ}-\frac{b}{J}\right)\Delta\theta \qquad (4.48)$$

Substituting the system characteristics of Table 4.1 into Equation 4.48, for a load of $b=0.01\ N.m/rad/\sec$ where $\dot{\theta}_m=154.21rad/\sec$, gives:

$$\Delta\theta=1.39\,rad \qquad (4.49)$$

Substituting Equation 4.49 and $\dot{\theta}_m=154.21rad/\sec$ into Equation 4.39 gives:

$$\lambda=110.6\sec^{-1} \qquad (4.50)$$

This value matches that obtained earlier from Equation 4.43.

Increasing the slope of the sliding surface beyond this optimum value leads to an overshoot in the system response. If the sliding surface slope is selected to be $\lambda=150\sec^{-1}$, the response of the motor system and the corresponding phase portrait are shown in Figures 4.22 and 4.23 respectively. The response and the phase portrait corresponding to the same proportional controller gain used earlier , i.e. $k = 17.16$, are also shown. As it can be seen in the enlarged region of Figure 4.22, the system leaves the sliding surface and circles around the equilibrium state causing a small overshoot (around the critically damped state) in the response as shown in Figure 4.23. However, the response is faster for the SMC than that of the proportional controller.

Figure 4.24 shows the motor response using a PD-controller tuned using Ziegler-Nichols tuning method [33]. The gains of the PD-controller are $k_p = 22$ and $k_d = 0.04$. The PD controlled system response shows less overshoot than the proportionally controlled one with $k = 17.16$. Increasing the value of the damping term of the PD- controller to $k_d = 0.3$ based on the trial and error tuning function of MATLAB Control System Toolbox results in an overdamped response as shown in the figure. The figure also shows the response of the motor when the proportional controller is used with a critically damped gain, i.e. $k = 2.17$. The proposed SMC controlled system is shown to be the fastest in reaching the final value among all controllers and with no overshoot.

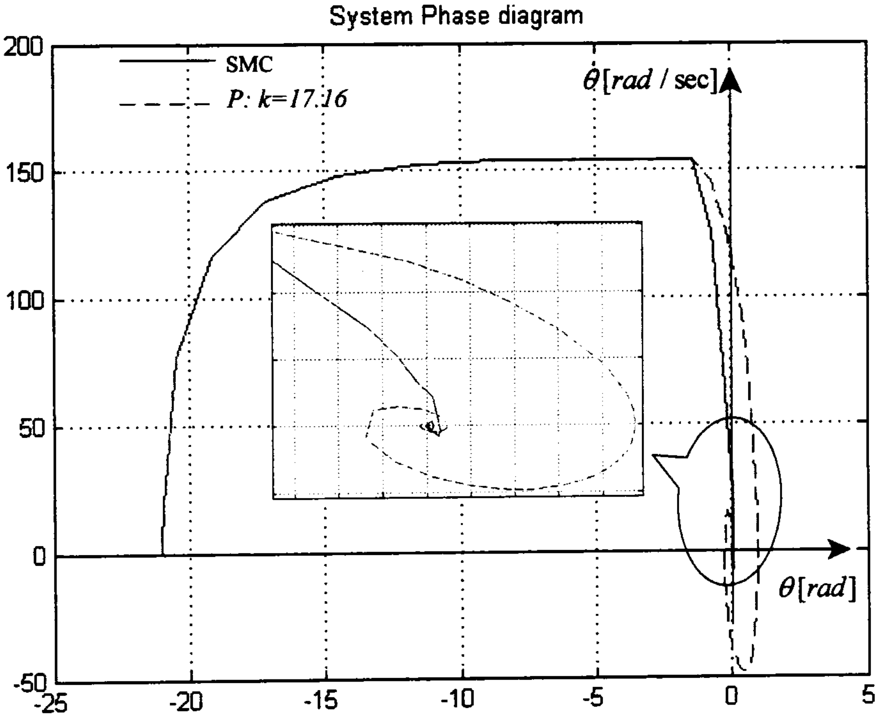

Figure 4.22: DC motor phase portrait with $\lambda = 150$

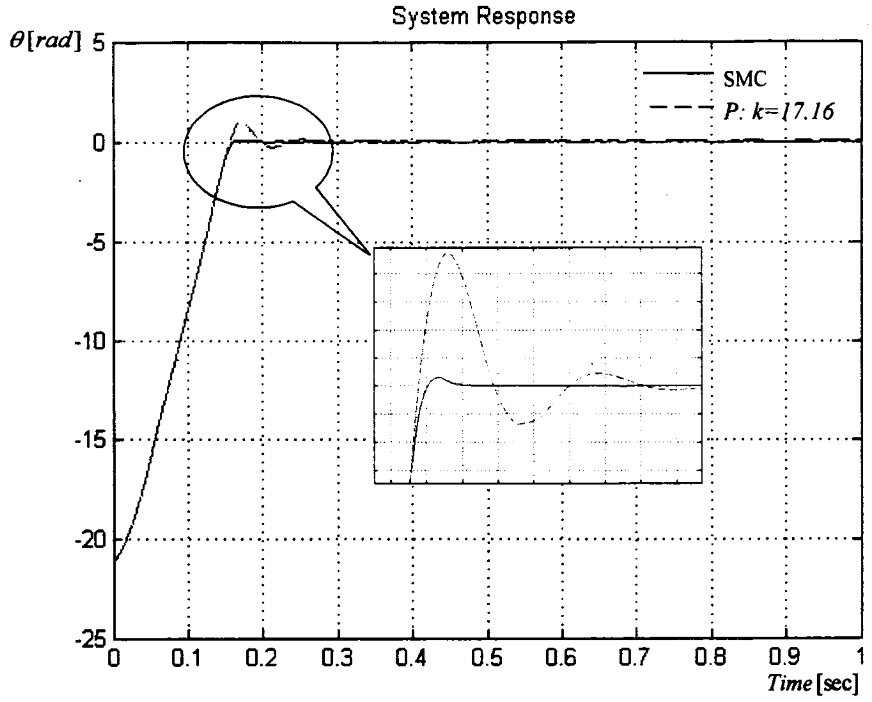

Figure 4.23: DC motor response with $\lambda = 150$

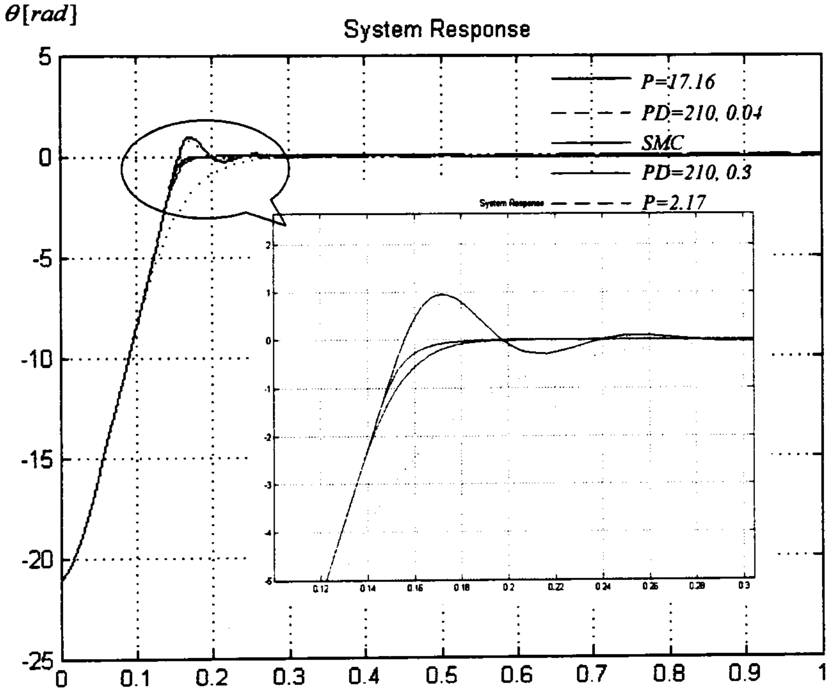

Figure 4.24: DC motor response Using PD-controller

4.9 Adaptive Controller for a DC motor

As mentioned in the introduction of this chapter, adaptive controllers are effective in the presence of system nonlinearities and uncertainties. However, they are not effective when the conditions of the system are changing rapidly. This section proves that adaptive controllers are more sensitive than SMCs to system parameters changes. A model reference adaptive controller is used to control the DC motor used in Section 4.8. The performance of the adaptive controller is then compared to that of the proposed SMC. Figure 4.25 shows a block diagram of the motor model with the adaptive controller. The adaptive control law shown in the figure is given by:

$$\dot{K}_C = \beta \dot{e}(r - y_p) \tag{4.51}$$

where β is adaptation constant that affects the convergence of the system. Increasing the value of this constant decreases the time of convergence.

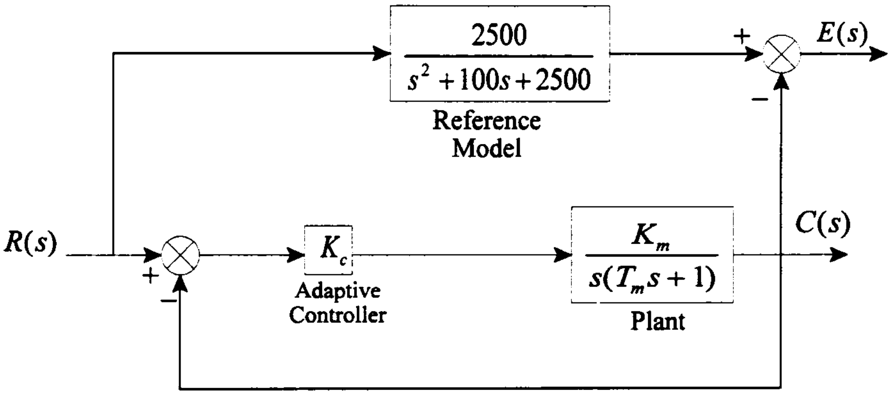

Figure 4.25: Block diagram of adaptive controller for a DC motor

If the adaptation constant is chosen high, $\beta = 20000$, the system converges very fast as shown in Figure 4.26. The figure also shows the response of the DC motor when the load on the motor is changing rapidly. The load change represents an external disturbance. Figure 4.27 shows a comparison between the performance of the adaptive controller and the proposed SMC used in Section 4.8 with $\lambda = 110\,\text{sec}^{-1}$ when a disturbance is applied to the motor. The figure clearly shows that the SMC controlled system is shown to be less sensitive than that controlled using an adaptive controller.

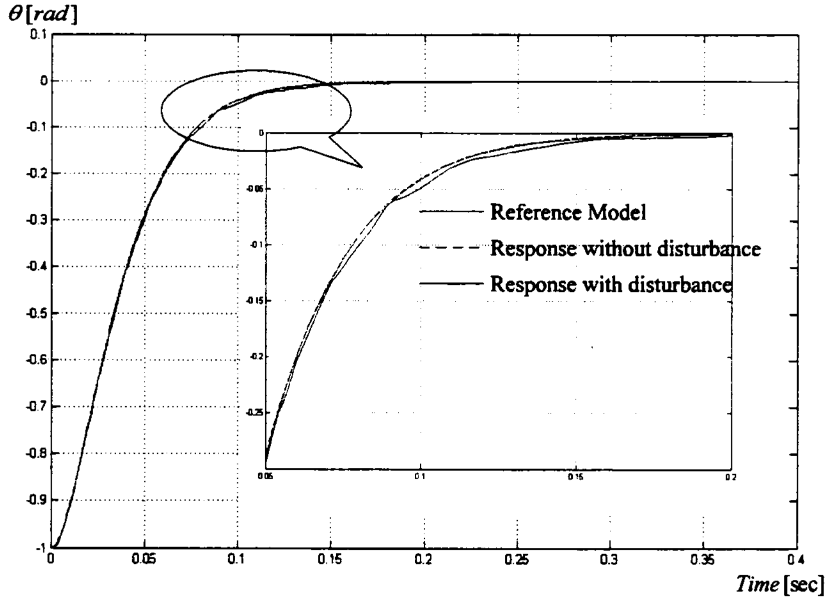

Figure 4.26: DC motor response using adaptive controller

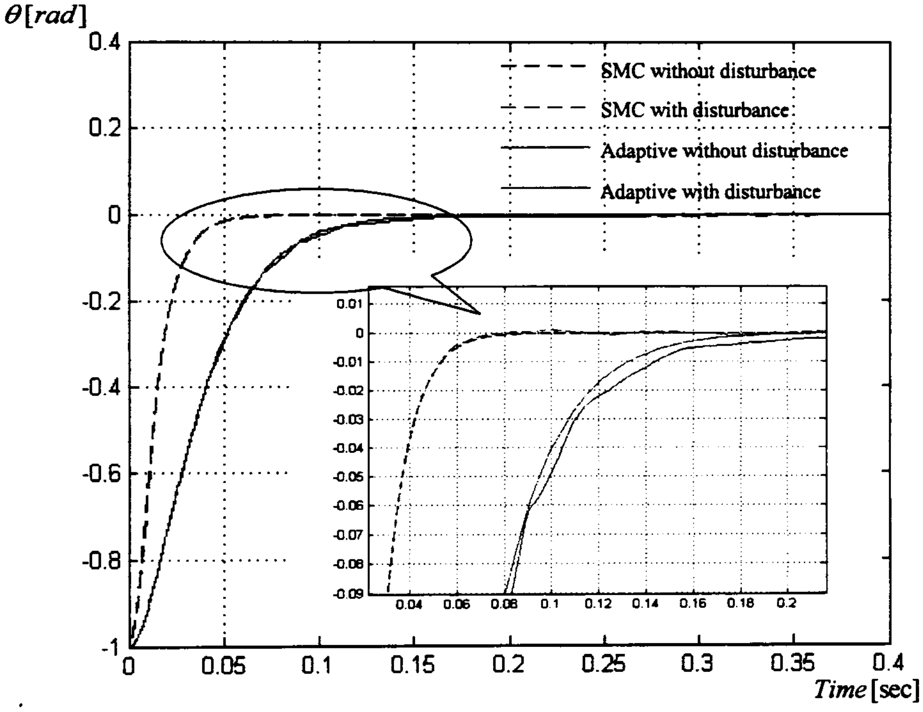

Figure 4.27: DC motor response using SMC and adaptive controller

Chapter 5

Extension of the Proposed Sliding Mode Control Approach to Single-input-multi-output Systems

5.1 Introduction

The SMC design methodology derived in Chapter 4 is primarily for a SISO control system. Chapter 3 shows that the TAGV model is a special case of MIMO systems. Hence, the initial part of this chapter will focus on an extension of the SMC design methodology so that it can be applied to SIMO systems. The extension will be exemplified using an inverted pendulum control system. Simulation results of the inverted pendulum system controlled using the SMC are then compared to those of other controller schemes such as a proportional controller.

Applying the new extended SMC design methodology to the TAGV system and its simulation results are given in the next chapter.

5.2 Inverted Pendulum System

Figure 5.1 shows an inverted pendulum system. Such systems are popular examples in many control texts because of the interesting dynamics they represent and the many practical applications they can model, particularly in the filed of robotics and rockets [31]. The system is also found to be essential for performance evaluation and comparison of various types of controllers. The general case of the inverted pendulum system is considered to be a special case of a MIMO system. The system has one input and two outputs. The input is the force u and the two outputs are the system state, the pendulum angle θ and the cart position x.

The goal for this system is to keep the pendulum always upright. To do so, an input force u has to be controllably applied to the cart to keep the system stable.

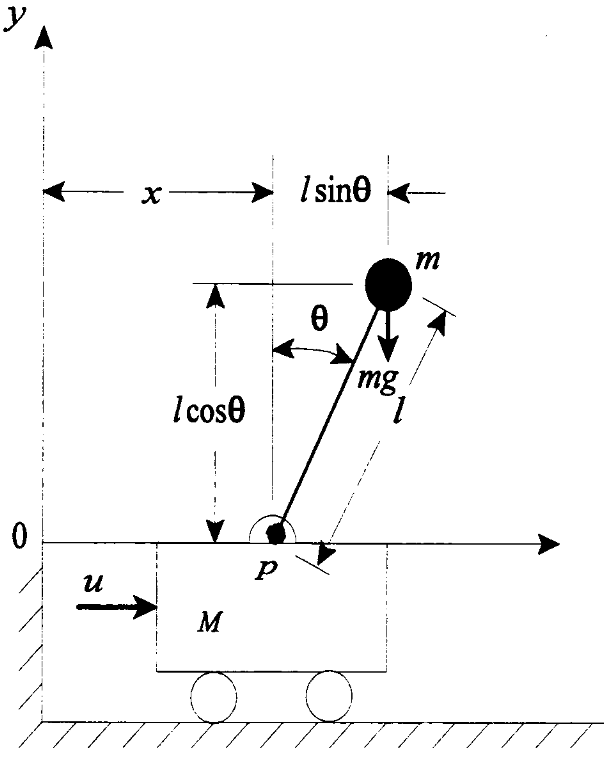

Figure 5.1: Inverted pendulum system

5.2.1 Inverted Pendulum System Model

With reference to Appendix *C*, the following equations represent the inverted pendulum dynamics:

$$M\ddot{x} + mg\theta = u \tag{5.1}$$

$$Ml\ddot{\theta} - (M+m)g\theta = -u \tag{5.2}$$

By eliminating $\ddot{x}$ from Equations C.9 and C.10 of Appendix *C*, the following equation is achieved:

$$Ml\ddot{\theta} - (M+m)g\theta = -u \tag{5.3}$$

Hence, the plant transfer function is given as follows:

$$\frac{\Theta(s)}{-U(s)}=\frac{1/Ml}{s^2-\dfrac{(M+m)g}{Ml}} \tag{5.4}$$

The model of the inverted pendulum system can be expressed in block diagram form as shown in Figure 5.2.

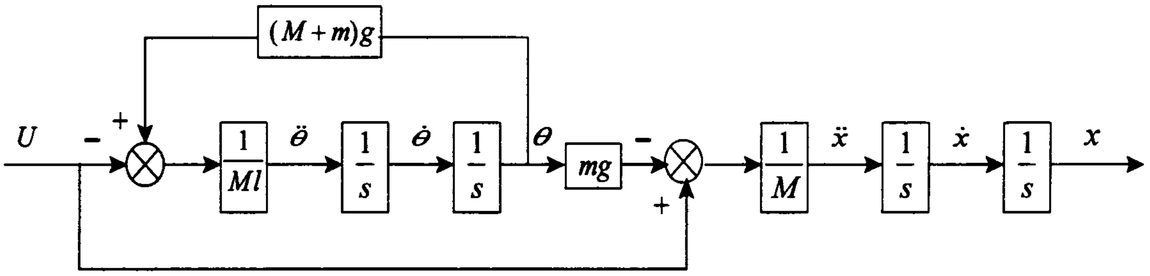

Figure 5.2: Open-loop inverted pendulum system

5.3 SMC of SIMO Systems Using Decoupled Sliding Surfaces

5.3.1 Controller Design

In this section the controller is designed such that sliding on the pendulum and the cart sliding surfaces occurs independently. Figure 5.3 shows the block diagram of the inverted pendulum system with the SMC. To bring the system back to stability at $x = 0$, $\theta = 0$ after a disturbance is a difficult task since the system is a SIMO system. In other word, it is difficult to control two output variables with one input simultaneously. However, to guarantee this control task, two different sliding mode surfaces, s_1 and s_2, corresponding to the two desired system outputs are used with one control signal *u*. The sliding surfaces are given by:

For the cart :

$$s_1 = \lambda_1 x + \dot{x} \tag{5.5}$$

For the pendulum:

$$s_2 = \lambda_2 \theta + \dot{\theta} \tag{5.6}$$

The input force applied to the cart u is a relay type control signal and is given by:

$$u = k_1 x + k_2 \theta \tag{5.7}$$

where,

$$k_1 = \begin{cases} +\eta_1, & sx > 0 \\ -\eta_1, & sx < 0 \end{cases} \tag{5.8}$$

$$k_2 = \begin{cases} +\eta_2, & s\theta > 0 \\ -\eta_2, & s\theta < 0 \end{cases} \tag{5.9}$$

and

λ_1, λ_2	are the slopes of the cart and the pendulum sliding surfaces respectively
k_1, k_2	are the controller gains of the cart and the pendulum respectively
η_1, η_2	are the magnitudes of the controller gains of the cart and the pendulum respectively

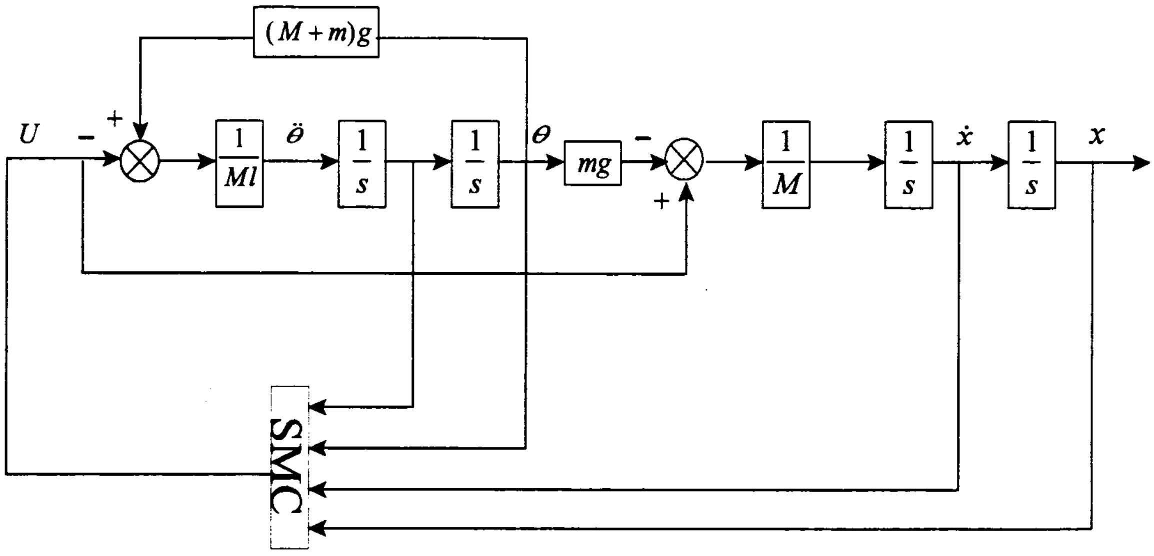

Figure 5.3: Closed-loop inverted pendulum system with SMC

The energy based design approach developed in the previous chapter, and specifically Equation 4.20, will be used here to design the SMC for the pendulum system. Since two separate sliding surfaces are needed, the following equations are used to design the SMC:

$$k_1 = \frac{1}{2}\beta_1\lambda_1^2 + \Gamma_1\lambda_1 + \frac{1}{2}\alpha_1 \tag{5.10}$$

$$k_2 = \frac{1}{2}\beta_2\lambda_2^2 + \Gamma_2\lambda_2 + \frac{1}{2}\alpha_2 \tag{5.11}$$

Applying the same methodology used in Section 4.5 for finding the coefficients β, α, and Γ for both k_1 and k_2, i.e., comparing Equations 5.1 and 5.2 to Equations 5.10 and 5.11, the following similarities are concluded:

$$\begin{aligned} k_1 &= \frac{1}{2}\beta_1\lambda_1^2 + \Gamma_1\lambda_1 + \frac{1}{2}\alpha_1 \\ &= \frac{1}{2}M\lambda_1{}^2 \end{aligned} \tag{5.12}$$

$$\begin{aligned} k_2 &= \frac{1}{2}\beta_2\lambda_2^2 + \Gamma_2\lambda_2 + \frac{1}{2}\alpha_2 \\ &= \frac{1}{2}Ml\lambda_2^2 + \frac{1}{2}(M+m)g \end{aligned} \tag{5.13}$$

Equations 5.12 and 5.13 show that choosing the values of the slopes and hence the corresponding control switching gains is difficult especially with the existence of the cross coupling between the dynamics of the cart and that of the pendulum. The equations also show that for each of the two parts the value of one of the parameters, λ_i or k_i, has to be assumed. The ranges of the SMC parameters $(k_1, k_2, \lambda_1, \lambda_2)$ are very wide such that additional constraints have to be imposed on the choice of the parameters to guide the choice. The system sensitivity [32] to parameters variations is introduced to find such constraints or parameter limitations. The condition that $\dot{s} = 0$ is necessary to keep the system state on the sliding surface. Combining the system sensitivity with $\dot{s}_1 = 0$ and $\dot{s}_2 = 0$ for both sliding surfaces results in the following cases:

Case I) Sliding surface of the cart

Since $s_1 = \lambda_1 x + \dot{x}$, the rate of change of the sliding surface equation $\dot{s}_1$ is given by:

$$\lambda_1\dot{x} + \ddot{x} = 0 \tag{5.14}$$

Substituting for $\ddot{x}$ and u from Equations 5.1 and 5.7 into Equation 5.14 respectively results in the following:

$$\lambda_1\dot{x} + \frac{1}{M}k_1 x + (\frac{1}{M}k_2 - \frac{mg}{M})\theta = 0 \tag{5.15}$$

The change in the angular position θ of the inverted pendulum system, and hence its stability to changes in the cart velocity $\dot{x}$ can be obtained from the partial derivative of θ with respect to $\dot{x}$ as follows:

$$\frac{\partial\theta}{\partial\dot{x}} = -\frac{M\lambda_1}{k_2 - mg} \tag{5.16}$$

In order that the pendulum position θ is rendered insensitive to the cart velocity, the magnitude of the denominator of Equation 5.16 must be larger than that of the numerator. This implies that $\lambda_1 < (k_2 - mg) / M$. Substituting for λ_1 and then for k_2 from Equations 5.12 and 5.13 receptively into Equation 5.16 gives the following two constraints:

$$k_1 < \frac{(k_2 - mg)^2}{2M} \tag{5.17}$$

$$\lambda_1 < \frac{1}{2} l\lambda_2^2 + \frac{1}{2M}(M - m)g \tag{5.18}$$

Case II) Sliding surface of the pendulum

The sliding surface of the pendulum is $s_2 = \lambda_2\theta + \dot{\theta}$ and the rate of change of s_2 when the system state is on the sliding surface is given by:

$$\lambda_2\dot{\theta} + \ddot{\theta} = 0 \tag{5.19}$$

Substituting Equations 5.1 and 5.7 into Equation 5.19 for $\ddot{\theta}$ and u gives:

$$\lambda_2\dot{\theta} + \left(\frac{(M+m)g}{Ml} - \frac{k_2}{Ml}\right)\theta - \frac{k_1}{Ml}x = 0 \tag{5.20}$$

It can be seen that Equation 5.20 provides no significant information. Also, it is not possible to carry out the sensitivity analysis since the equation does not include the cart velocity.

5.3.2 Simulation Results and Comparisons

In this section, a performance comparison between a traditionally designed proportional controller and the new approach of the SMC designed following the above procedure is carried out. Equations 5.12 and 5.13 are used to determine the SMC slopes and the corresponding controller gains subject to the constraints given by Equations 5.17 and 5.18. To be able to use these equations, the values of the parameters $M, m, l,$ and g must be known. Table 5.1 gives the values of these parameters used in the simulation.

Table 5.1: Inverted pendulum numerical values

m	$0.1\ kg$
M	$2\ kg$
l	$0.5\ m$
g	$9.81 m/\sec^2$

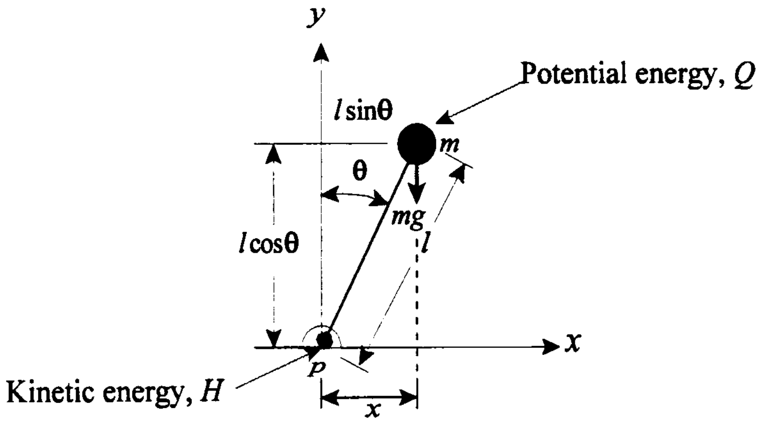

Figure 5.4: Pendulum energies

Substituting the parameters in Table 5.1 into Equations 5.12 and 5.13 gives:

$$k_1 = \lambda_1^2 \tag{5.21}$$

$$k_2 = \frac{1}{2}\lambda_2^2 + 10.3 \tag{5.22}$$

With reference to Section 4.6, studying the location of the poles of Equation 5.4 in the s-plane provides the stability of the plant. Figure 5.5 is the root-locus diagram of the plant poles when changing the proportional gain. Based on the selection of the proportional gain, the system is either unstable or critically stable. If the gain is selected to result in a critically stable system, the system is critically stable in the reaching mode. However, for the entire system controlled using the proposed SMC, the following simulation will show that the system is asymptotically stable due to the sliding action along the sliding surface.

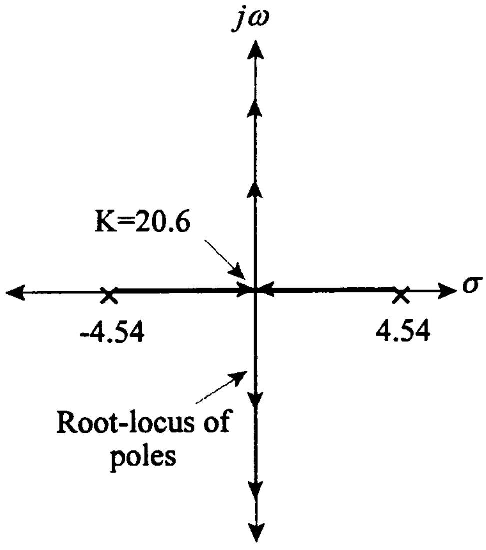

Figure 5.5: Root-locus diagram of the pendulum

With reference to Figure 5.4, in order to find the optimal limits of Equations 5.21 and 5.22, the pendulum is disturbed by applying an initial input angle θ. The pendulum in this position has a maximum potential energy Q that must be compensated for by the kinetic energy H in order to keep the system stable. The kinetic energy H should be attained from the cart motion. To guarantee this, the following equation is used:

$$\begin{aligned} Q &= H \\ mgl\cos\theta &= \frac{1}{2}(M+m)\dot{x}^2 \end{aligned} \tag{5.23}$$

It should be noted that Equation 5.23 is valid under the assumption made earlier that the pendulum angular velocity is negligible.

For small input angle, $\cos\theta = 1$ and Equation 5.23 can be cast in the following form:

$$\dot{x} = \sqrt{\frac{2mgl}{M+m}} \tag{5.24}$$

Substituting for the values of the parameters from Table 5.1 into Equation 5.24 gives $\dot{x} = 0.683\, m/\sec$. This is considered as the minimum velocity required to provide the necessary kinetic energy to balance for the pendulum potential energy. Moreover, this value of the velocity is not enough to return the pendulum back to its stable position. Hence, a higher velocity of the cart is required. With reference to Figure 5.4, assume the following condition to be valid:

$$l\dot{\theta} = \dot{x} \tag{5.25}$$

Substituting for $l = 0.5m$ and $\dot{x} = 0.683\, m/\sec$ into Equation 5.25 gives $\dot{\theta} = 1.366\, rad/\sec$. Assuming the system state is on the sliding surface of the pendulum, for an initial input angle of $\theta = -0.1\, rad$, the slope of the sliding surface can be approximated to be:

$$\begin{aligned}\lambda_2 &= \frac{\dot{\theta}}{\theta} \\ &= \frac{1.366}{0.1} \\ &= 13.66 \text{ sec}^{-1}\end{aligned} \tag{5.26}$$

The initial state of the inverted pendulum system is boundary stable upright. The system is disturbed by applying an initial input angle of $\theta = -0.1 rad$ (5.73°). The controller is required to keep the pendulum upright by generating the required force u as explained earlier. In order to design the SMC, Equations 5.11 and 5.12 are used with the constraints found from the sensitivity analysis. The slope of the cart sliding surface λ_1 must satisfy the condition of Equation 5.18. For $\lambda_2 = 13.66 \text{sec}^{-1}$, $\lambda_1 << 51.3$. λ_1 is selected to be 0.7sec^{-1}. Substituting these values into Equations 5.21 and 5.22 results in the corresponding controller gains $k_1 = \pm 0.49$ and $k_2 = \pm 103.6$. These values do satisfy the constraint set forth by Equation 5.17. The responses of the pendulum and the cart with respect to time for this design case are shown in Figures 5.6 and 5.8 respectively. The corresponding phase portraits are shown in Figures 5.7 and 5.9 respectively. The system state crosses the sliding surface at a relatively high speed such that it leaves the sliding surface as shown in Figure 5.7. Since the structure of the controller is unable to brake the system, the system circles around the origin and intercepts the sliding surface in the lower right quadrant. In Figure 5.6, this is manifested by the oscillations of the pendulum around the set point. With reference to the cart, when the pendulum is disturbed by the initial input angle, the cart tries to compensate by moving in the same direction of the input angle as shown in Figure 5.9. While returning back to its original position, the cart oscillates around the origin in response to the oscillatory behavior of the pendulum in order to keep it stable upright as shown in Figure 5.8. This is manifested on the phase diagram whereby its response leaves the sliding surface of the cart while stabilizing the pendulum and returning back to the original position represented by the origin of the plot.

Reducing the slopes of the cart and the pendulum sliding surfaces to $\lambda_1 = 0.1 \text{sec}^{-1}$, $\lambda_2 = 10 \text{sec}^{-1}$ receptively results in the responses and the phase portraits shown in the

Figures 5.10-5.13. In this case, the response of the pendulum is marginally underdamped, and the pendulum will keep oscillating with a small magnitude around the equilibrium point. The response of the cart in this case is overdamped. Reducing the slopes implies reducing the kinetic energy when the system states intercept the sliding surfaces for the pendulum and the cart. The system states do not leave the sliding surface as shown in Figures 5.11 and 5.13.

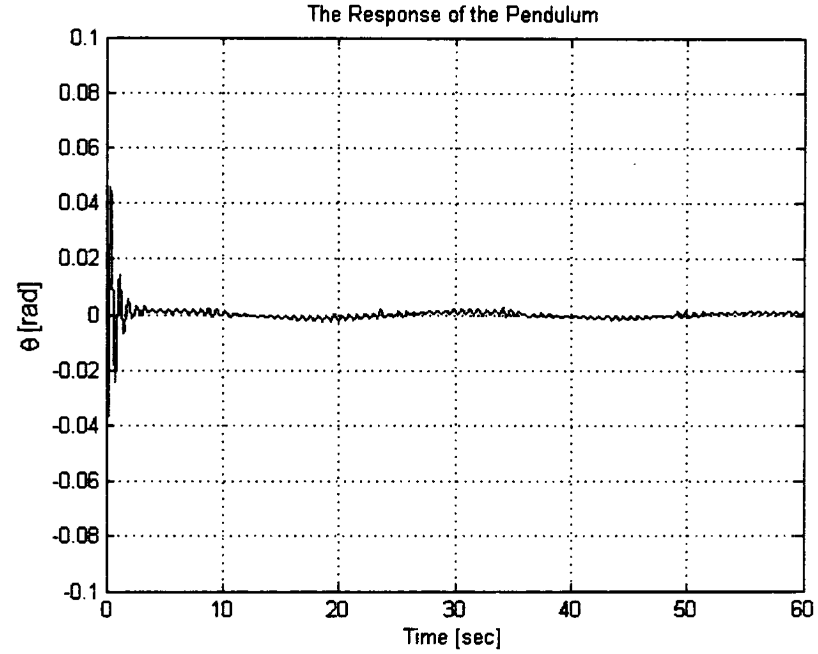

Figure 5.6: Pendulum response for the SMC with $\lambda_1 = 0.7$ and $\lambda_2 = 13.66$

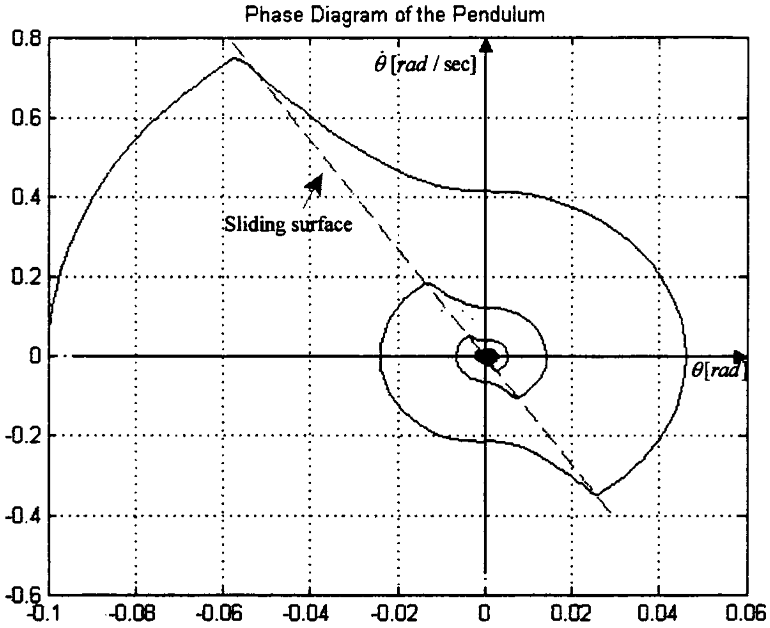

Figure 5.7: Pendulum phase portrait for the SMC with $\lambda_1 = 0.7$ and $\lambda_2 = 13.66$

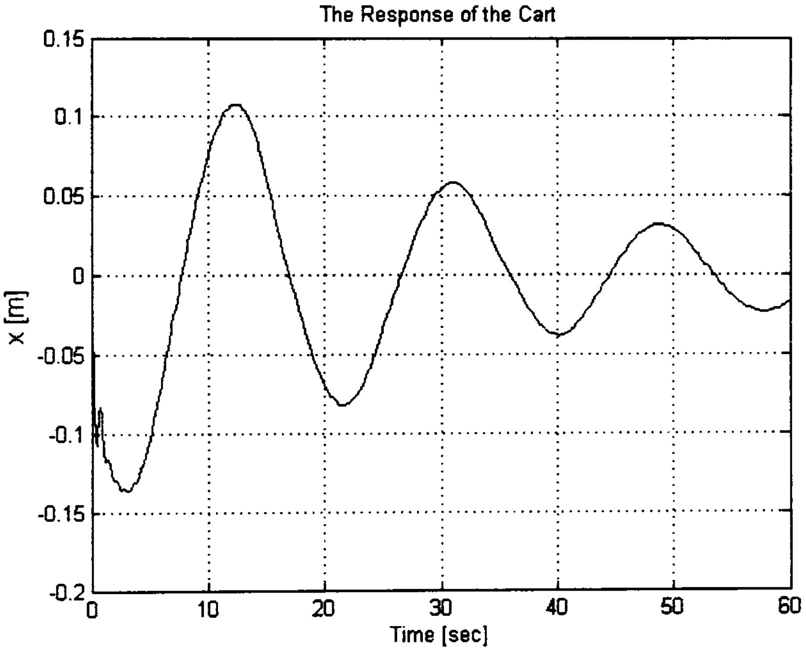

Figure 5.8: Cart response for the SMC with $\lambda_1 = 0.7$ and $\lambda_2 = 13.66$

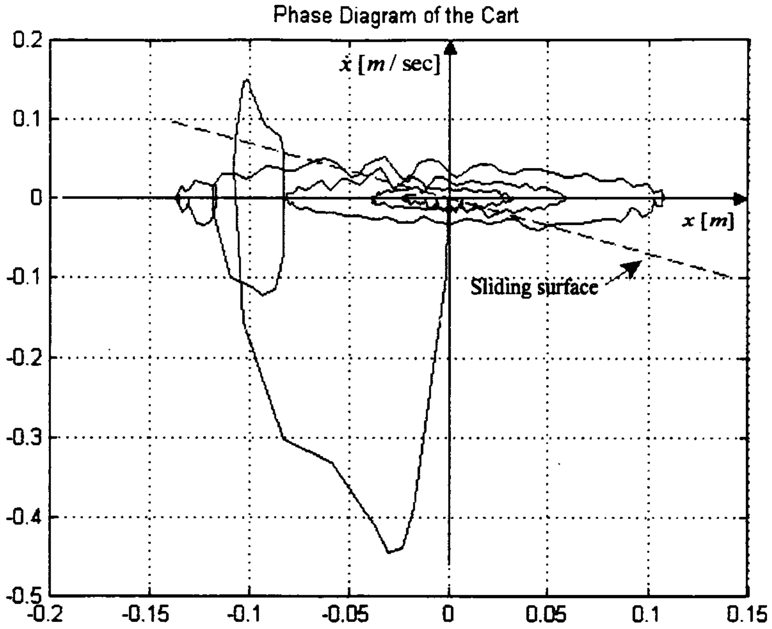

Figure 5.9: Cart phase portrait for the SMC with $\lambda_1 = 0.7$ and $\lambda_2 = 13.66$

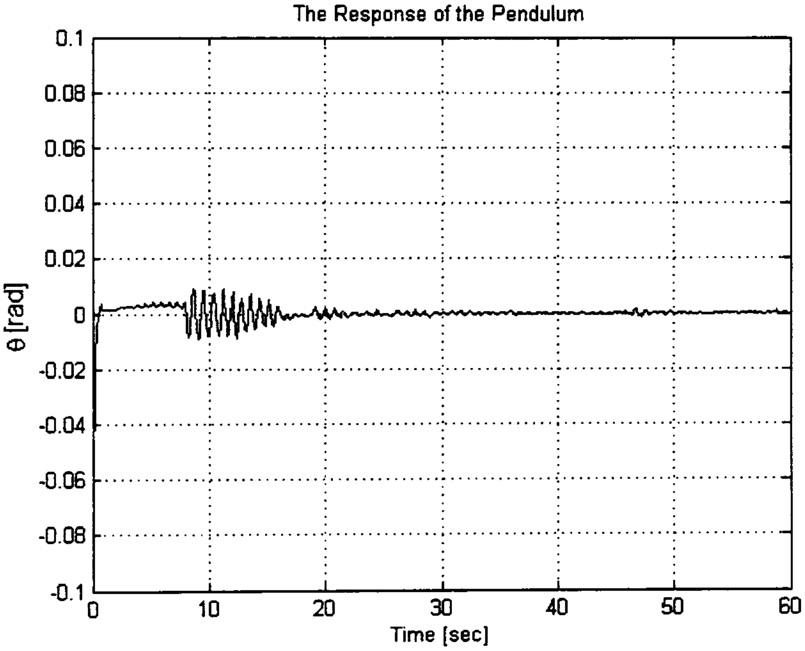

Figure 5.10: Pendulum response for the SMC with $\lambda_1 = 0.1$ and $\lambda_2 = 10$

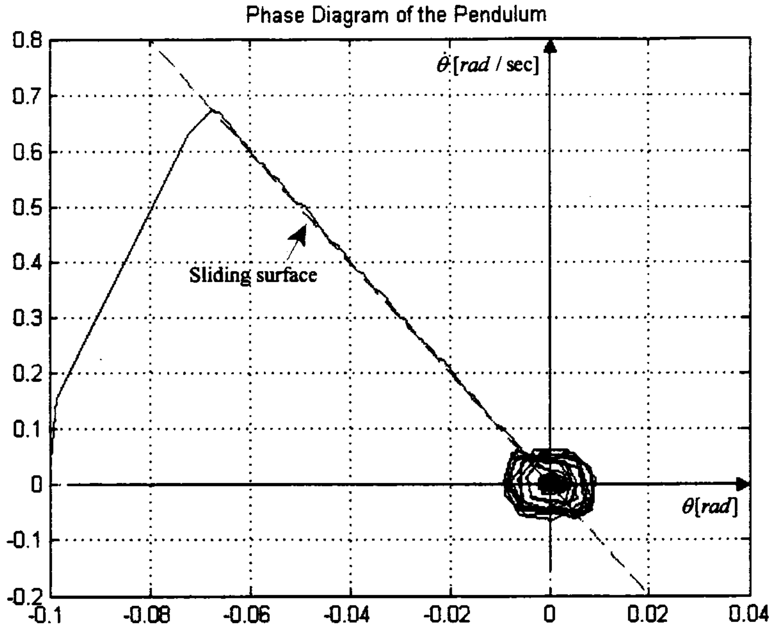

Figure 5.11: Pendulum phase portrait for the SMC with $\lambda_1 = 0.1$ and $\lambda_2 = 10$

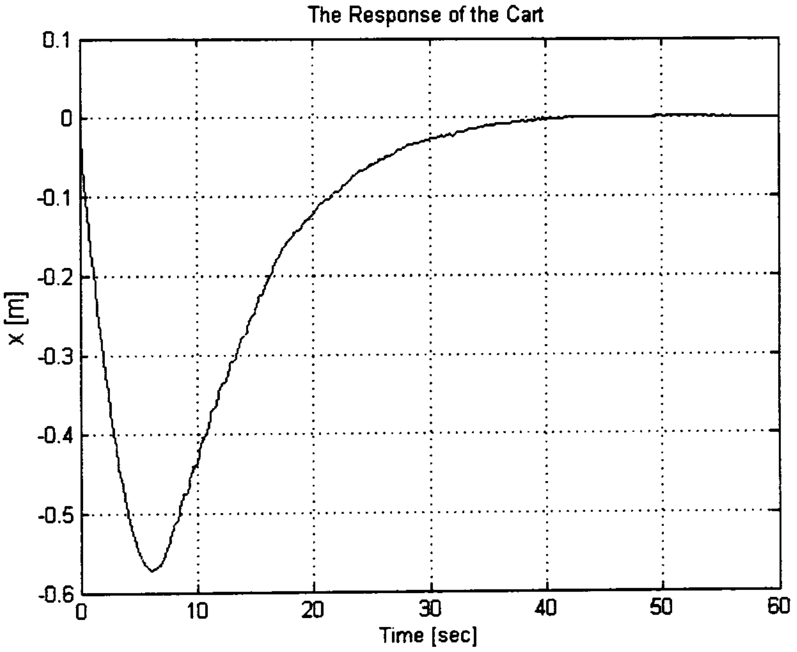

Figure 5.12: Cart response for the SMC with $\lambda_1 = 0.1$ and $\lambda_2 = 10$

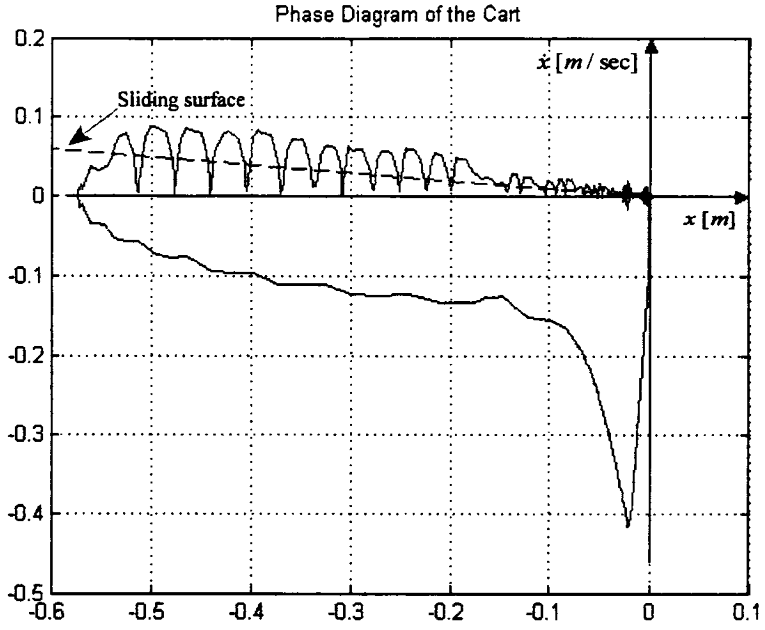

Figure 5.13: Cart phase portrait for the SMC with $\lambda_1 = 0.1$ and $\lambda_2 = 10$

Since the system is a single input-two output one, a possible proportional control law can be constructed as follows:

$$u = k_1 x + k_2 \theta \tag{5.27}$$

where k_1 and k_2 are the controller gains.

As has been shown above, for a proportionally controlled pendulum, any value for the proportionality constant below $k_2 = 20.6$ results in an unstable system. Values above $k_2 = 20.6$ result in a critically stable system. Increasing the magnitude of the proportionality gain speeds up convergence, however the system remains critically stable. For comparison purposes, if the proportional controller gains are selected to be $k_1 = 0.49$ and $k_2 = 103.6$ to match the gains selected for the SMC controller for reference purposes, the responses of the pendulum and cart for the same step input used earlier are shown in Figures 5.14 and 5.16 respectively. The corresponding phase portraits are shown in Figures 5.15 and 5.17 respectively. The figures show critically stable undamped responses. Figures 5.14 and 5.16 show a fixed range angular and positional displacements for both the pendulum and cart. These ranges are expressed by a repetition of a circular shape of the pendulum and the cart phase portraits shown in Figures 5.15 and 5.17 respectively.

The performance of the SMC and the proportional controller based on the simulation results clearly show how the energy is absorbed by SMC as it asymptotically brings the system to stability, while it is not the case when the proportional controller is used.

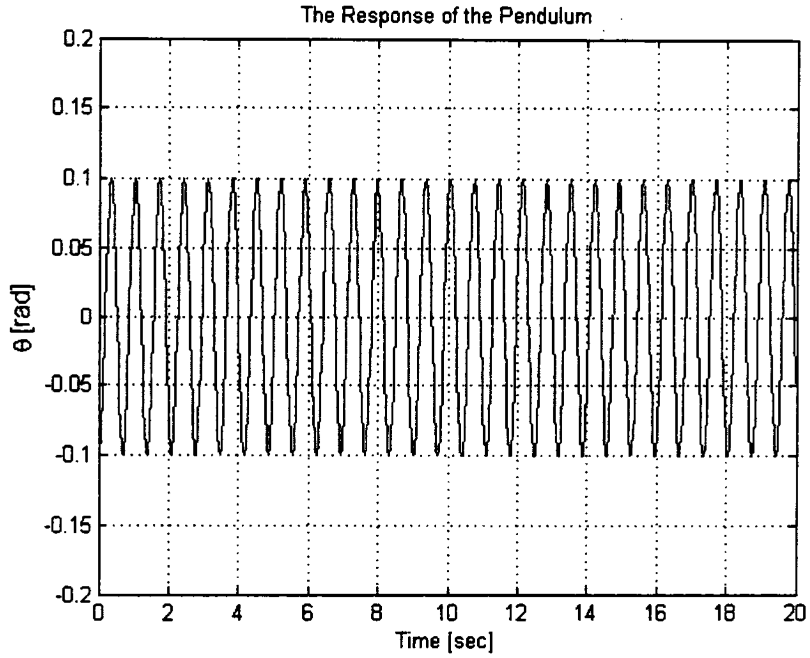

Figure 5.14: Pendulum response for the P-controller with $k_1 = 0.49$ and $k_2 = 103.6$

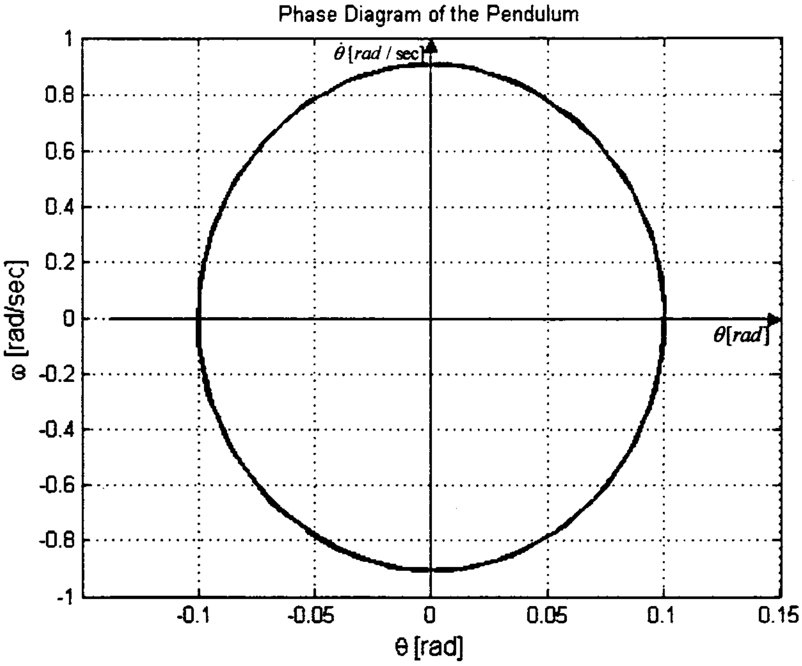

Figure 5.15: Pendulum phase portrait for the P-controller with $k_1 = 0.49$ and $k_2 = 103.6$

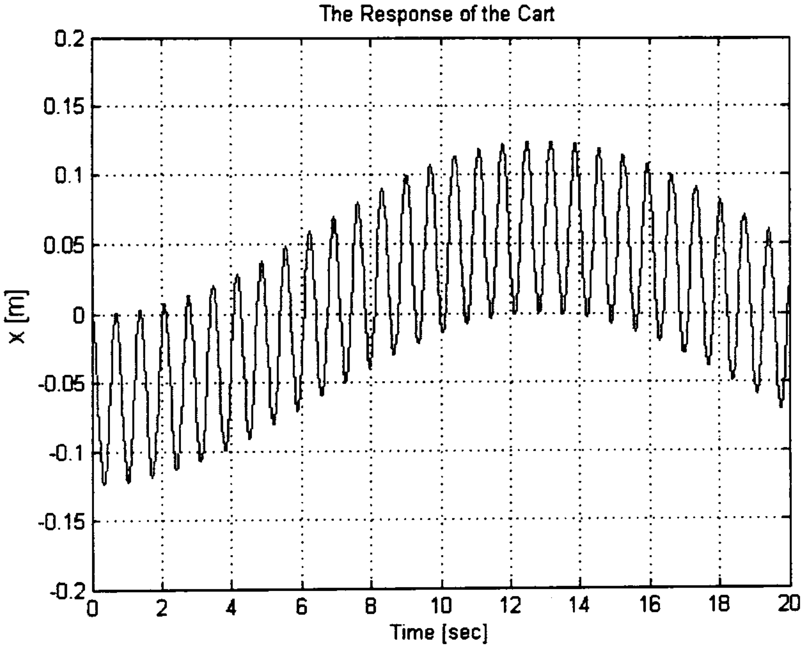

Figure 5.16: Cart response for the P-controller with $k_1 = 0.49$ and $k_2 = 103.6$

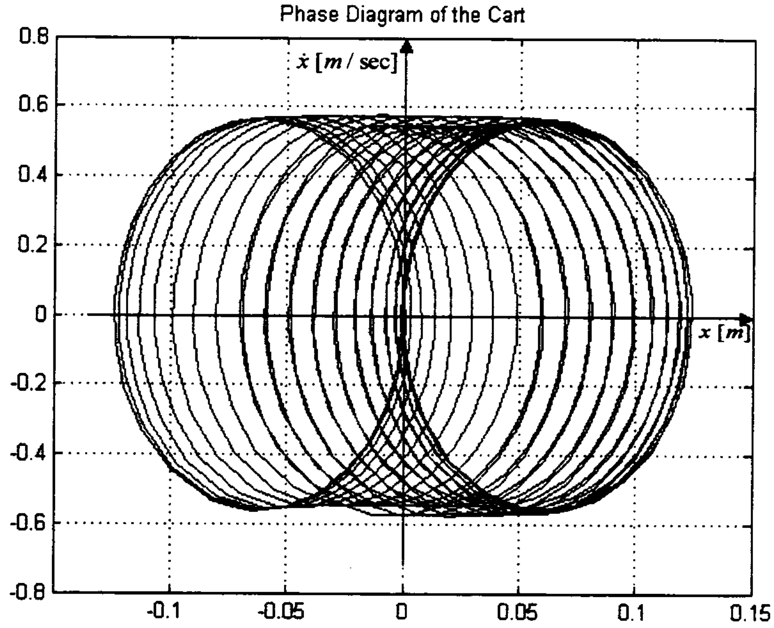

Figure 5.17: Cart phase portrait for the P-controller with $k_1 = 0.49$ and $k_2 = 103.6$

5.4 SMC for SIMO Systems Using Hyper Sliding Surface

5.4.1 Controller Design

In this section, the sliding mode controller is designed such that the sliding surfaces of the pendulum and the cart are coupled together to form a hyper sliding surface s. The hyper sliding surface has the following form:

$$s = s_1 + s_2 \tag{5.28}$$

where s_1 and s_2 are the sliding surfaces of the pendulum and the cart respectively.

Substituting Equations 5.5 and 5.6 for s_1 and s_2 into Equation 5.28 gives:

$$s = \lambda_1 x + \dot{x} + \lambda_2 \theta + \dot{\theta} \tag{5.29}$$

The input force applied to the cart *u* is of a relay type control signal and is given by:

$$u = \begin{cases} +\nu, & s > 0 \\ -\nu, & s < 0 \end{cases} \tag{5.30}$$

where the values of $+\nu$ and $-\nu$ are chosen based on the system capability. In this example, they depend on the cart DC motor capability.

5.4.2 Simulation Results and Comparisons

If a DC motor is used to provide the desired input force *u* to the cart, the selection of the values $+\nu$ and $-\nu$ is based on the motor torque limits. The DC motor used in Chapter 4 has a rated torque of *0.28 N.m.* and a gear ratio of 1:16. If the cart wheel connected to the motor has a radius of *5 cm*, the controller force *u* will have switching gains ± 90. For the same siding surfaces slopes used in Section 5.3, $\lambda_1 = 0.7\,\text{sec}^{-1}$ and $\lambda_2 = 13.66\,\text{sec}^{-1}$, Figures 5.18 and 5.19 show the responses of the pendulum and cart respectively. The performance of this controller is much better than those of the previous controllers. The pendulum response is faster than the ones shown in Section 5.3 and is marginally underdamped (around the critical damping state). The cart response shows an underdamped response with a small overshoot; however, it is faster than the ones of Section 5.3.

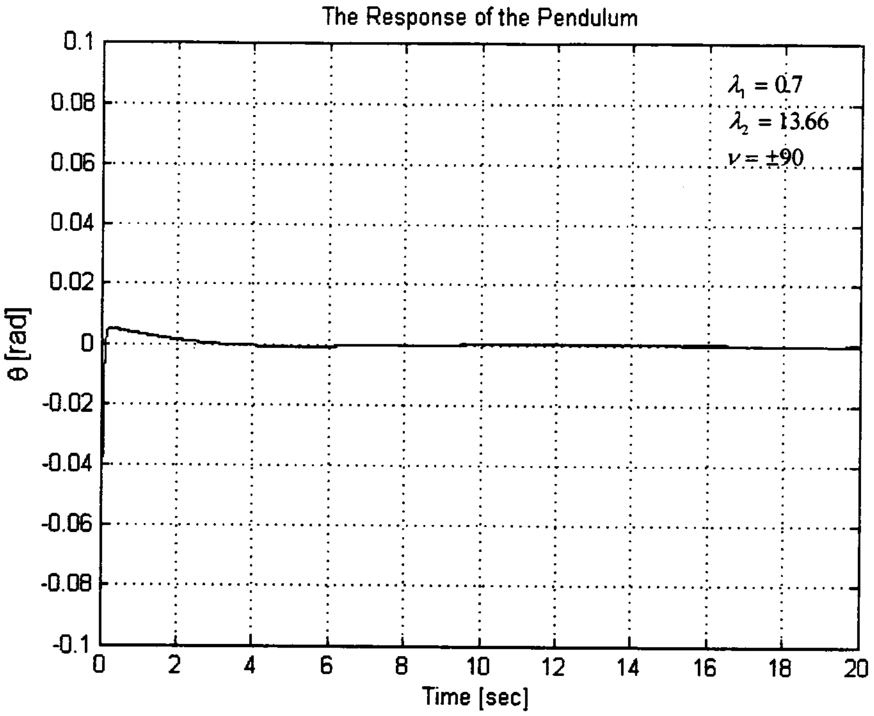

Figure 5.18: Pendulum response for Hyper SMC

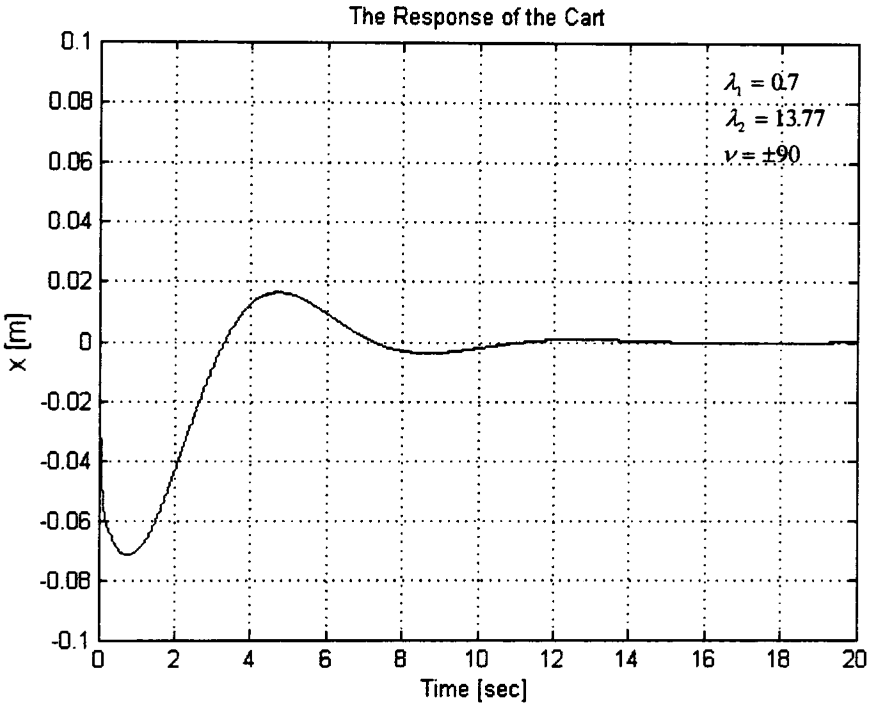

Figure 5.19: Cart response for Hyper SMC

5.5 SMC of Pure Inertial Systems

5.5.1 Controller Design

The inverted pendulum system has no dissipative viscous load to absorb energy. This can be seen in the dynamic equations of the system. The controller design used in Section 5.3 also does not include any damping terms in the control law to compensate for the lack of damping. Hence, adding a damping terms in the control law is advisable. This can be accomplished by modifying the control law of Equation 5.7 as follows:

$$u = k_1 x + k_2 \theta + k_3 \dot{x} + k_4 \dot{\theta} \tag{5.31}$$

where,

k_1, k_2	are the same controller gains given by Equations 5.8 and 5.9
k_3, k_4	are the damping controller gains, and chosen to be always positive

In order to select suitable values for k_3 and k_4, the system sensitivity analysis is carried out as follows:

case I) Sliding surface of the cart

Substituting for $\ddot{x}$ and u from Equations 5.1 and 5.31 into Equation 5.14 respectively gives:

$$\left(\lambda_1 + \frac{k_3}{M}\right)\dot{x} + \frac{k_1}{M}x + \frac{k_2 - mg}{M}\theta + \frac{k_4}{M}\dot{\theta} = 0 \tag{5.32}$$

Taking the partial derivative of the pendulum angle with respect to the cart velocity in Equation 5.32 gives:

$$\frac{\partial \theta}{\partial \dot{x}} = -\frac{M\lambda_1 + k_3}{k_2 - mg} \tag{5.33}$$

case II) Sliding surface of the pendulum

Substituting Equations 5.2 and 5.31 into Equation 5.19 for $\ddot{\theta}$ and u respectively gives:

$$-\frac{k_1}{Ml}x-\frac{k_3}{Ml}\dot{x}+\frac{(M+m)g-k_2}{Ml}\theta+\left(\lambda_2-\frac{k_4}{Ml}\right)\dot{\theta}=0 \tag{5.34}$$

Taking the partial derivative of the pendulum angle with respect to the cart velocity in Equation 5.34 gives:

$$\frac{\partial\theta}{\partial\dot{x}}=\frac{k_3}{k_2-(M+m)g} \tag{5.35}$$

In order for the system to be rendered insensitive to the cart velocity, the magnitude of the denominators of Equations 5.33 and 5.35 must be larger than that of the numerators, hence:

$$k_3<k_2-mg-M\lambda_1 \tag{5.36}$$

$$k_3<k_2-(M+m)g \tag{5.37}$$

If the partial derivative of the pendulum angular velocity is taken with respect to the cart velocity in Equations 5.32 and 5.34, the following can be achieved:

$$\frac{\partial\dot{\theta}}{\partial\dot{x}}=-\frac{M\lambda_1+k_3}{k_4} \tag{5.38}$$

$$\frac{\partial\dot{\theta}}{\partial\dot{x}}=\frac{k_3}{k_4-\lambda_2 Ml} \tag{5.39}$$

With reference to Equation 5.25, the following equation is also valid:

$$\frac{d\dot{\theta}}{d\dot{x}}=\frac{1}{l} \tag{5.40}$$

Equating Equation 5.38 and 5.39 to Equation 5.40 respectively gives:

$$k_4=-(lk_3+Ml\lambda_1) \tag{5.41}$$

$$k_4 = lk_3 + Ml\lambda_2 \tag{5.42}$$

Equation 5.41 can be ignored since k_4 is chosen to be always positive.

5.5.2 Simulation Results and Comparisons

In order to use the control law of Equation 5.31, the controller gains k_1, k_2, k_3, and k_4 must be selected based on the sensitivity analysis of the system. With reference to Section 5.3, the slope of the cart sliding surface λ_1 must satisfy the condition of Equation 5.18. For $\lambda_2 = 13.66\,\text{sec}^{-1}$, $\lambda_1 << 51.3$. λ_1 is selected to be $2\,\text{sec}^{-1}$. Substituting these values into Equations 5.21 and 5.22 results in the corresponding controller gains $k_1 = \pm 4$ and $k_2 = \pm 103.6$ respectively. The damping controller gains k_3 and k_4 must satisfy the conditions of Equations 5.36, 5.37, and 5.42. Since $k_3 << 82.7$, k_3 is selected to be 9. Substituting the parameters in Table 5.1 into Equation 5.42 with $k_3=9$ results in $k_4=18.16$. Figures 5.20 and 5.21 shows the responses of the pendulum and the cart respectively. The response of the cart is overdamped and the response of the pendulum is marginally underdamped.

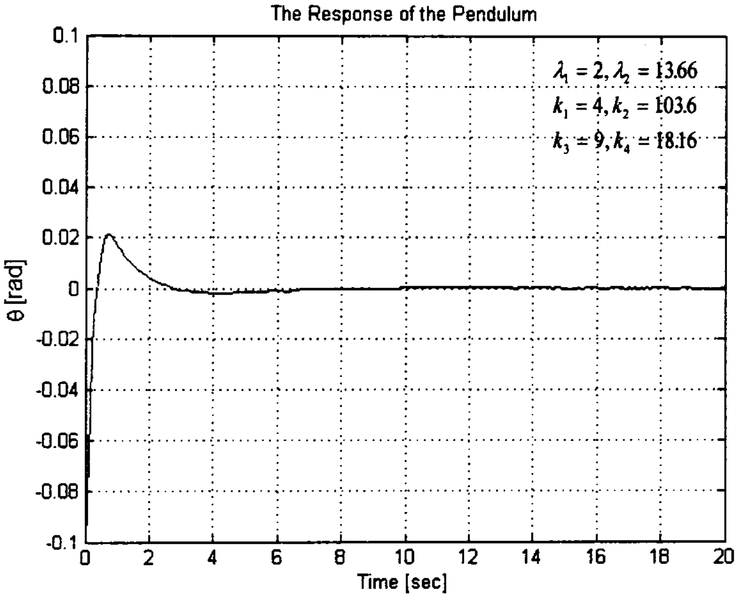

Figure 5.20: Pendulum response for the modified SMC of pure inertial systems

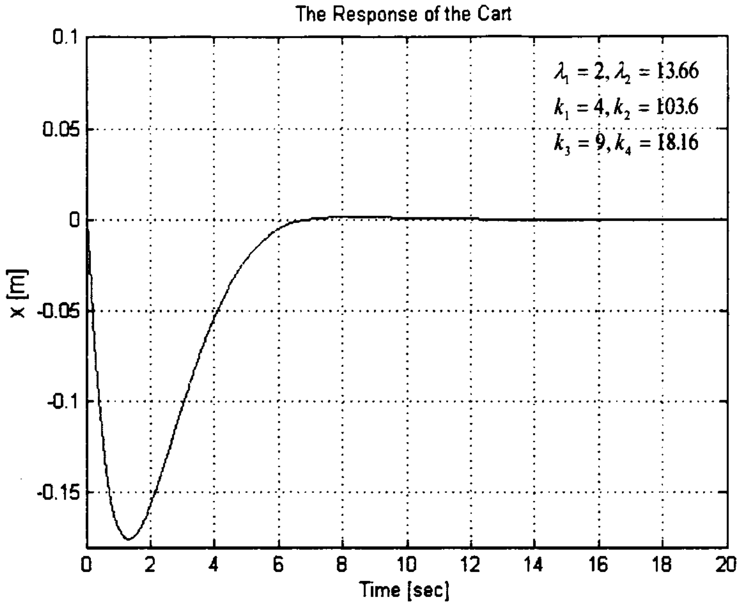

Figure 5.21: Cart response for the modified SMC of pure inertial systems

For comparison purposes, a Proportional-Derivative (PD) controller design that has the following form is used [33]:

$$u = 163.1x + 73.4\dot{x} + 298.15\theta + 60.7\dot{\theta} \tag{5.43}$$

The PD-controller gains of Equation 5.43 are chosen based on the pole placement tuning method where the closed-loop pole locations are selected to meet a given desired performance specifications. The closed-loop pole locations are chosen to give a 2 *sec* settling time [33]. The responses of the pendulum and the cart when using this controller are shown in Figures 5.22 and 5.23. The figures show that both responses are underdamped. The 2 *sec* settling time results in 0.5 damping ratio and 70% overshoot as shown in Figure 5.22. A faster response of the pendulum alone ignoring completely the cart can be obtained if the choice of the PD-controller gains of the pendulum are selected based on Ziegler-Nichols method of tuning [33]. The control law in this case is given by:

$$u = 210\theta + 10.5\dot{\theta} \tag{5.44}$$

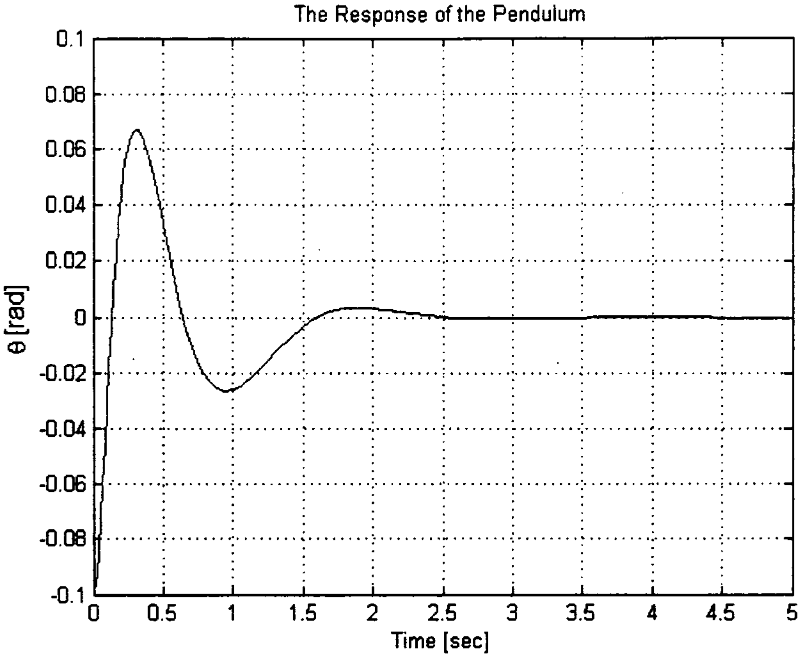

Figure 5.22: Pendulum response for PD-controller [33]

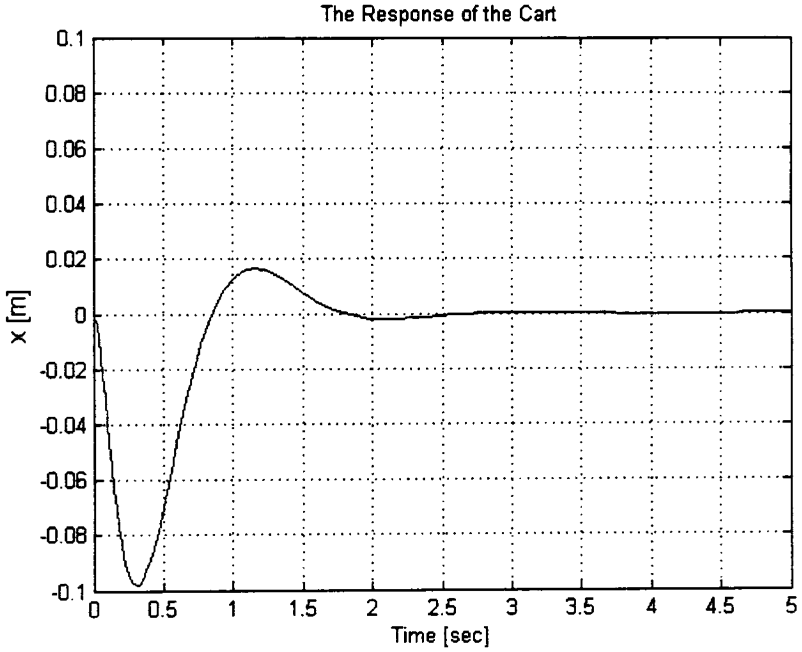

Figure 5.23: Cart response for PD-controller [33]

Figure 5.24 shows the response of the pendulum in this case. Figure 5.25 shows the cart response to continually move away from the desired equilibrium state since there is no contribution of the cart state in the control law. If the control law (Equation 5.44) is modified to include the cart state, and the gains of these state are tuned using the MATLAB Control System Toolbox, the following control law is obtained:

$$u = 15x + 5\dot{x} + 210\theta + 105\dot{\theta} \tag{5.45}$$

Figure 5.24 also shows the pendulum response when using this modified PD-controller. The figure shows the response to be more oscillatory, however, with reference to Figure 5.25 the cart response is shown to be stable but slightly underdamped. When MATLAB Control System Toolbox is used to tune the PD-controller gains of both the cart and pendulum together, the following control low results:

$$u = 80x + 100\dot{x} + 550\theta + 82\dot{\theta} \tag{5.46}$$

The response of the pendulum using the control law of Equation 5.46 is underdamped as shown in Figure 5.24. The cart response in this case however, is overdamped as shown in Figure 5.25.

Comparing the responses of the different controllers used so far shows that the PD-controller of Equation 5.43 has the fastest response for the cart, however, the response has an overshoot. The response of the system when using the SMC with the hyper sliding surface shows ideal performance for the pendulum where the response is almost at the critical damping state, and is faster than for all the other types of controllers. Comparing the responses of the cart and the pendulum for the original SMC of Equation 5.7 with that of the modified SMC of Equation 5.31 shows that the modified SMC has a better performance and a faster response. The response of the cart for the modified SMC also shows a faster response and a better performance than that of the SMC with a hyper sliding surface.

Among the four PD-controllers, that of Equation 5.44 results in the best performance of the pendulum, least overshoot and the fastest response. Comparing this performance to that of the SMC with the hyper sliding surface shows that the latter is still the best among all controllers. The cart response when using the controller of Equation 5.46 is faster than those resulting from using other controllers, and has no overshoot.

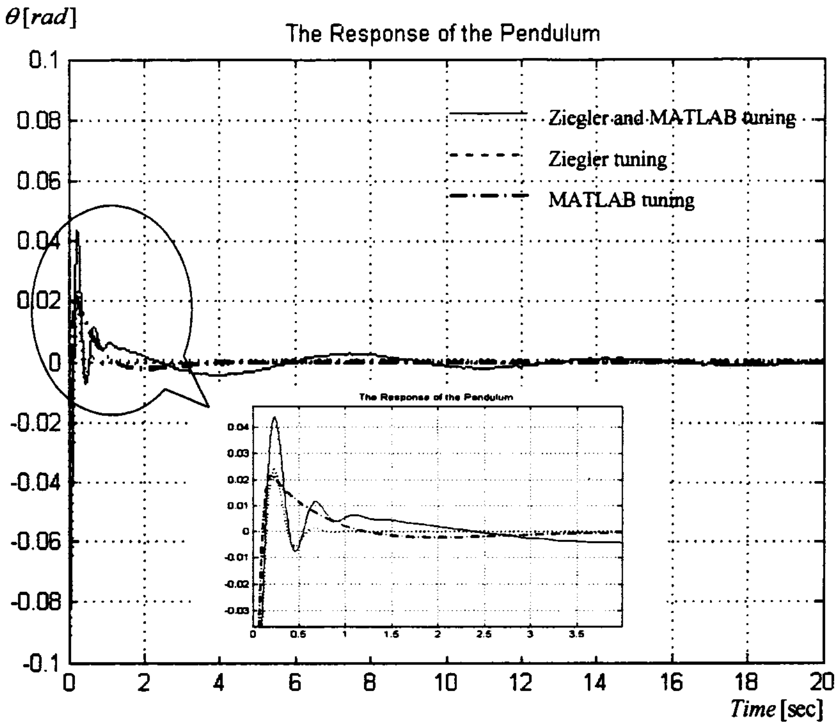

Figure 5.24: Pendulum responses using different tuning methods for PD-controllers

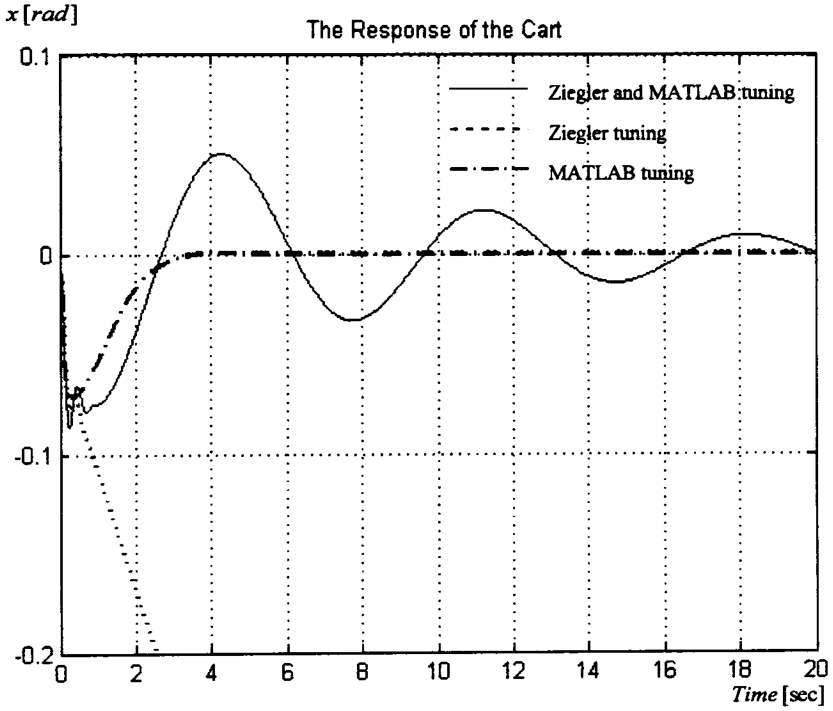

Figure 5.25: Cart responses using different tuning methods for PD-controllers

5.6 Simulation Results of the Nonlinear Inverted Pendulum System

The inverted pendulum system was linearized by assuming that the pendulum inclination angle is small such that the sinusoidal functions in its equation tend towards the magnitude of the angle, and that the pendulum angular velocity is negligible. In this section, these approximations are not carried out and the full nonlinear pendulum cart model is used to reevaluate the performances of all the controllers used.

Figures 5.26 to 5.37 show the responses of the pendulum and cart when controlled using two SMCs (with $\lambda_1 = 0.7$, $\lambda_2 = 13.66$ and $\lambda_1 = 0.1$, $\lambda_2 = 10$), the proportional controller, the hyper SMC, the modified SMC, and the PD-controller used before respectively. The figures show that the responses of the nonlinearized model are practically identical to those of the linearized model. This verification serves two purposes. Firstly, it shows that the linearized model is sufficiently accurate to allow it to be used as a basis for controller design. Secondly, it shows that even though the pendulum angle and its angular velocity is small but not negligible, yet its effect on the controllers performance is negligible.

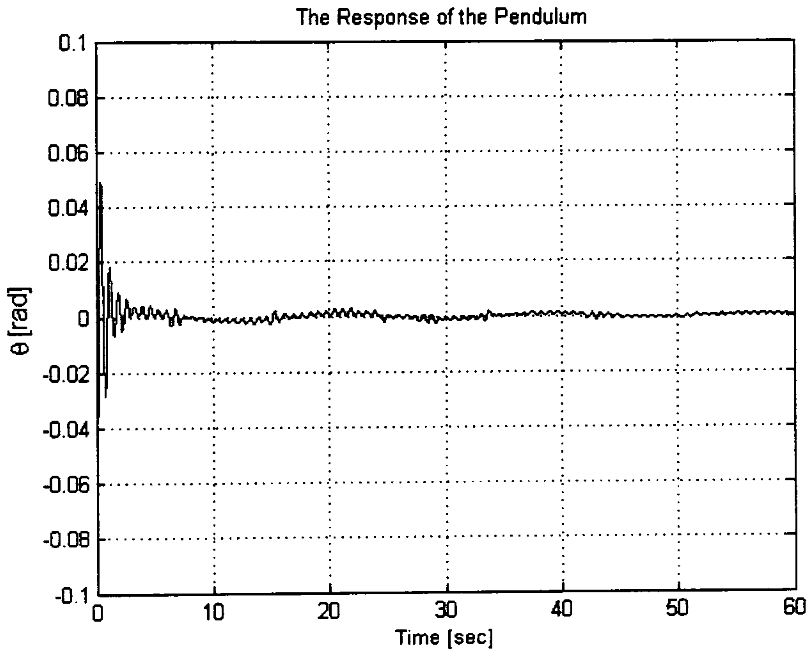

Figure 5.26: Pendulum response for the SMC with $\lambda_1 = 0.7$ and $\lambda_2 = 13.66$ (Nonlinearized model)

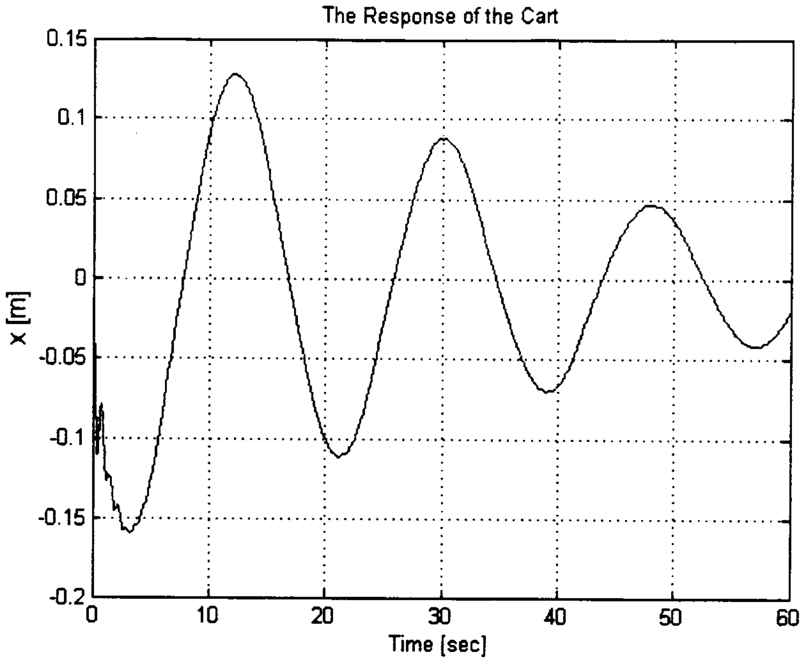

Figure 5.27: Cart response for the SMC with $\lambda_1 = 0.7$ and $\lambda_2 = 13.66$ (nonlinearized model)

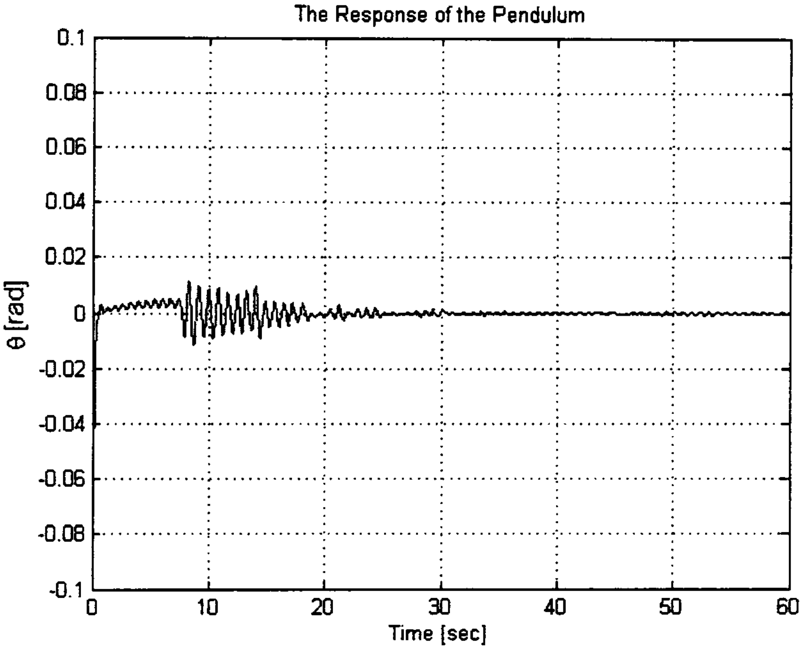

Figure 5.28: Pendulum response for the SMC with $\lambda_1 = 0.1$ and $\lambda_2 = 10$ (nonlinearized model)

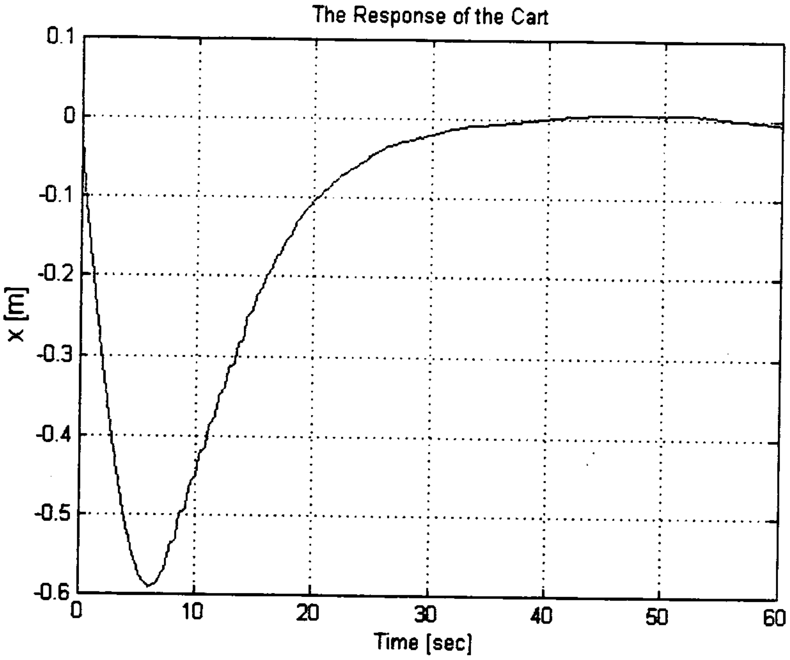

Figure 5.29: Cart response for the SMC with $\lambda_1 = 0.1$ and $\lambda_2 = 10$ (nonlinearized model)

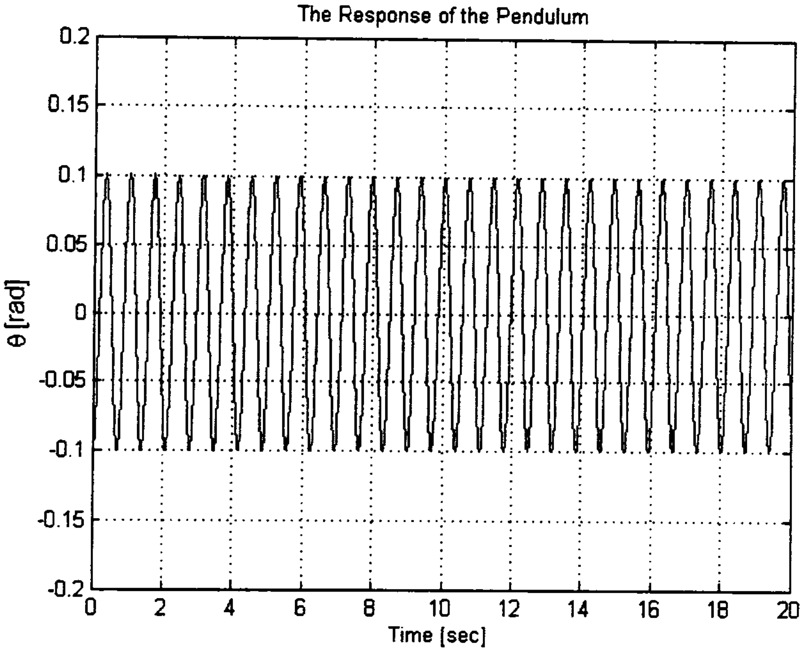

Figure 5.30: Pendulum response for the P-controller with $k_1 = 0.49$ and $k_2 = 103.6$ (nonlinearized model)

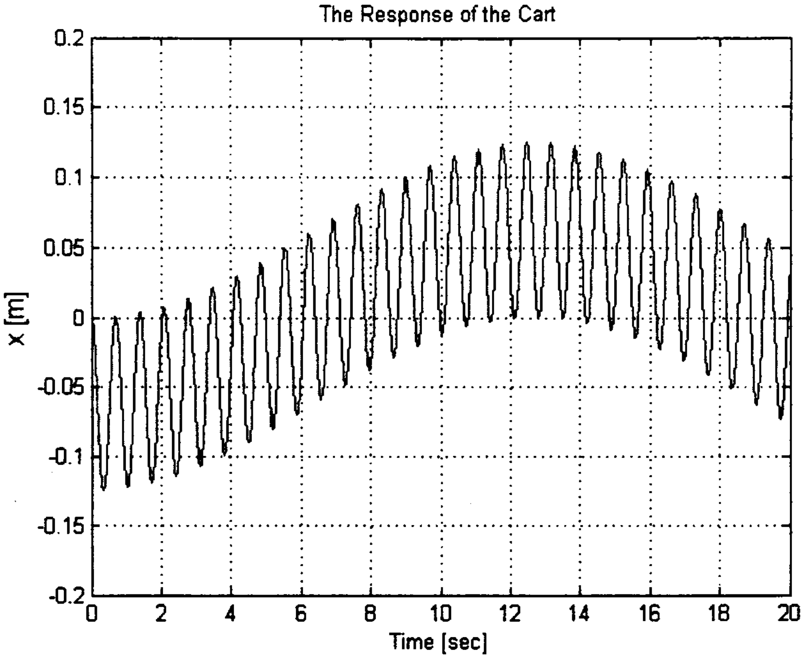

Figure 5.31: Cart response for the P-controller with $k_1 = 0.49$ and $k_2 = 103.6$ (nonlinearized model)

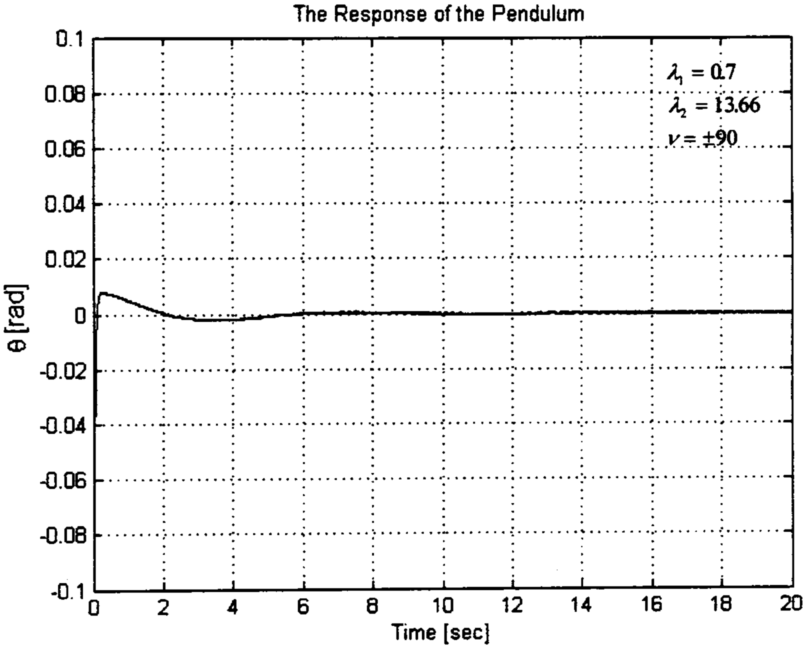

Figure 5.32: Pendulum response for Hyper SMC (nonlinearized model)

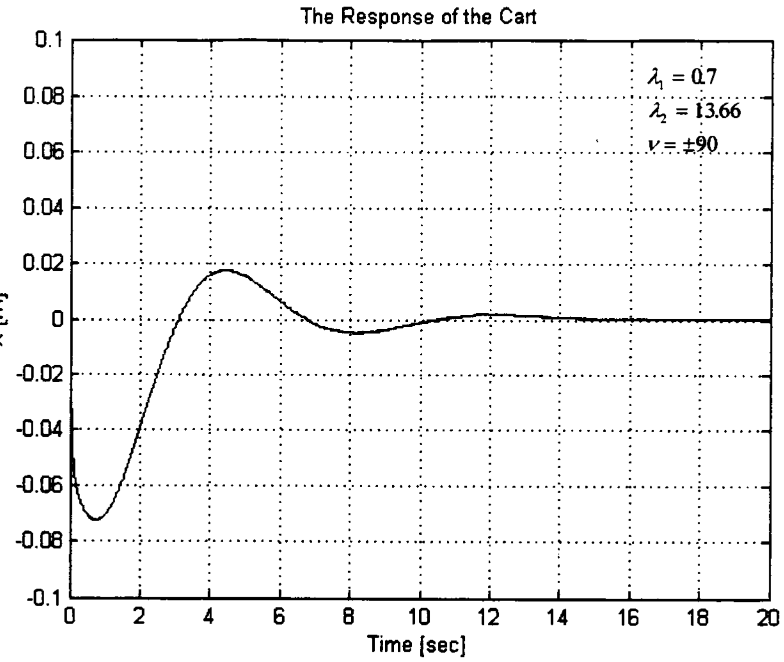

Figure 5.33: Cart response for Hyper SMC (nonlinearized model)

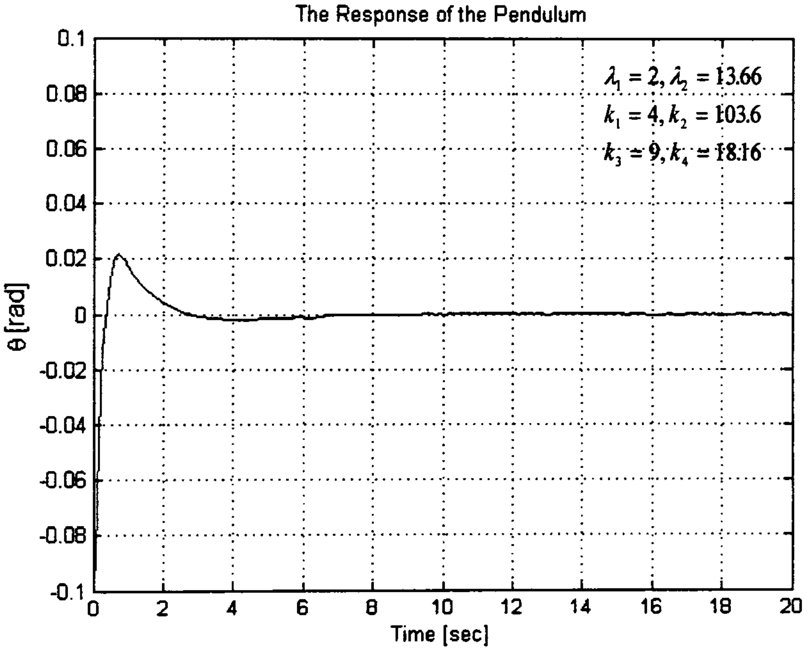

Figure 5.34: Pendulum response for the modified SMC of pure inertial systems (nonlinearized mode)

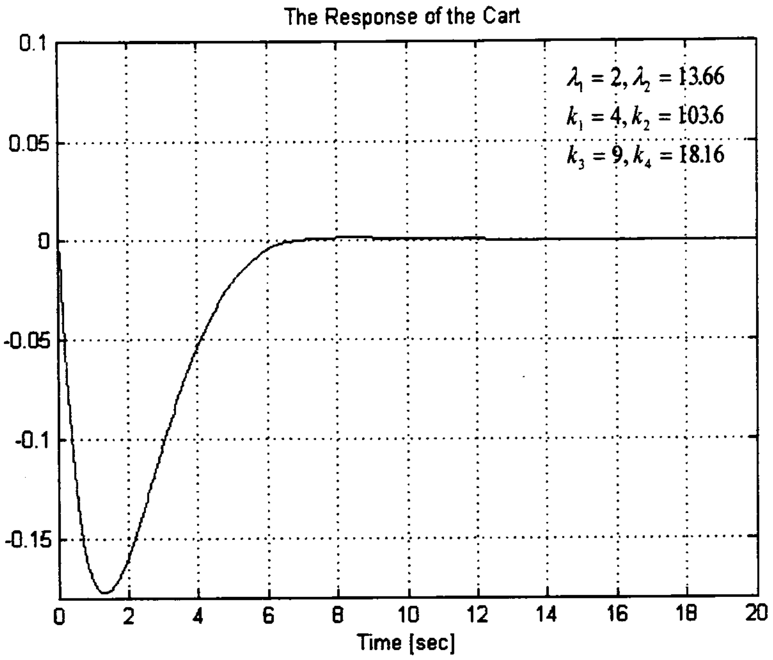

Figure 5.35: Cart response for the modified SMC of pure inertial systems (nonlinearized model)

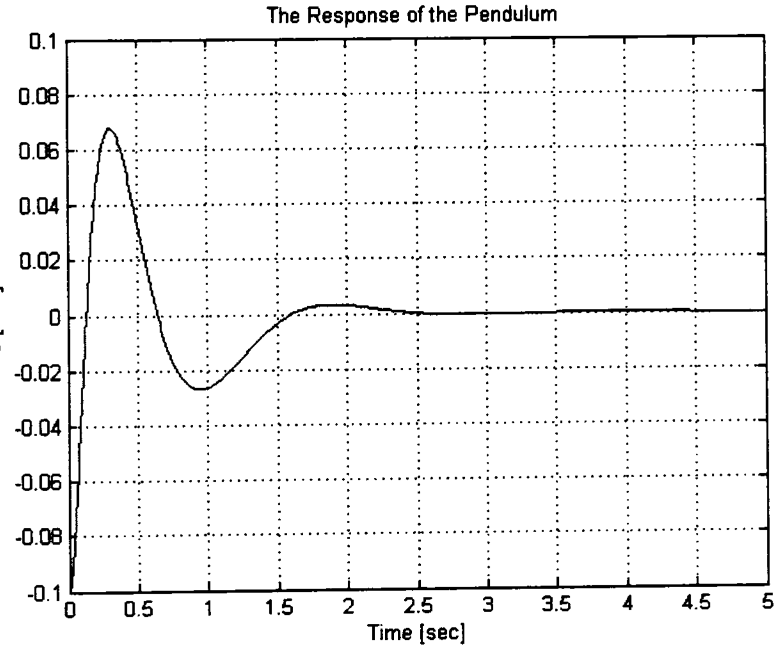

Figure 5.36: Pendulum response for PD-controller (nonlinearized model) [33]

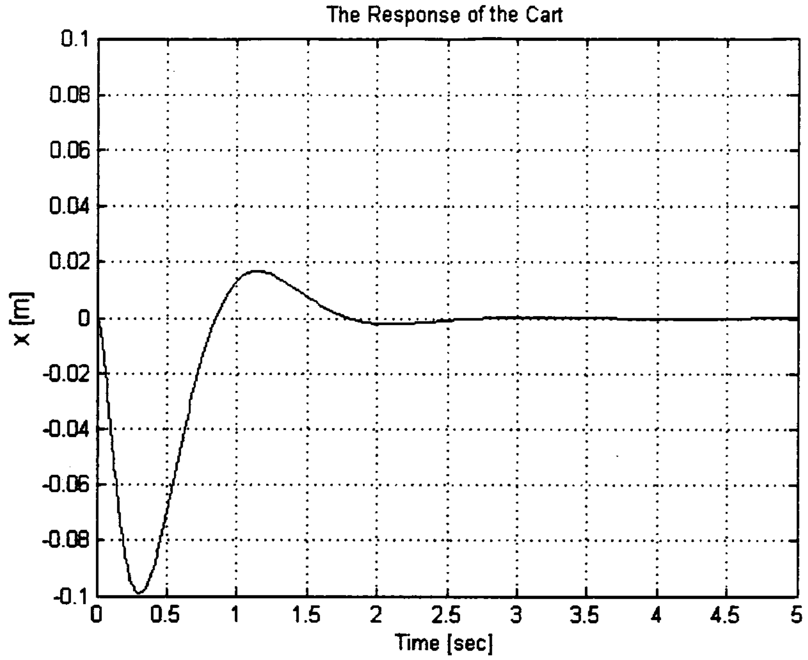

Figure 5.37: Cart response for PD-controller (nonlinearized model) [33]

5.7 Energy Based Design Procedure of SMCs

With reference to the SMC design for the DC motor carried out in Chapter 4 and the design for the inverted pendulum carried out in this chapter, the proposed SMC design procedure is summarized as follows:

1. Derive the full dynamic model of the plant that is required to be controlled.
2. For SISO systems only simple sliding surface (sliding line) is feasible. For SIMO systems two choices are available, namely; individual simple sliding surfaces between each system state and its derivative, or a hyper surface combining the system states. The choice is the designer prerogative.
3. Choose a suitable switching control law. A simple relay logic type switching controller suffices at this point.
4. Equation 4.20 establishes a relationship between the gain for a parameter and the slope of the sliding surface. Using the similarities between the parameters (inertial and potential

storage elements and dissipative elements) of the system dynamic equation(s) and Equation 4.20 calculate the relationship between k and λ.

5. Using the limiting power of the plant prime mover or power unit imposes additional constraints on the gains k of the controller.
6. For SIMO systems it may be necessary to use a sensitivity analysis to impose further constraints on the gains or the sliding surface(s) of the controller.
7. For practical applications where it is desired to reduce chattering due to the switching logic, a boundary layer straddling the sliding surface may be implemented. Alternatively, any appropriate technique for reducing chattering may be used.

Chapter 6

Tracked Autonomous Guided Vehicle Control and Simulation Results

6.1 Introduction

Accurate and fast navigational performance of a tracked autonomous guided vehicle system requires an effective control algorithm to generate the control signal. Such systems are highly nonlinear and generally include unmodeled terms due to track-ground interaction. Furthermore, they are often subjected to large disturbances especially when the vehicle crosses the boundary between different terrains while moving. However, using a SMC reduces the sensitivity of the vehicle to nonlinearities, disturbances, and unmodeled terms. The SMC design methodology derived in Chapter 4 is applied to the TAGV model here. The TAGV is a SIMO control system similar to the inverted pendulum control system explained in Chapter 5. Hence, the new extended SMC design methodology is applied to the TAGV system. The SMC is applied first when the sliding surfaces are independent and then when they are coupled together to form a hyper sliding surface.

In order to be able to apply a controller to drive the TAGV to the target pose, the vision-based navigational system explained in Chapter 3 is used. With reference to Figure 3.7, the vehicle navigational system is portrayed in Figure 6.1.

The chapter begins by an explanation of the overall control strategy used for the TAGV. This will be followed by the derivation of the SMC. The chapter will conclude by presenting simulation results of the TAGV system controlled using the SMC and comparisons of these with the cases when the SMC with hyper sliding surface and a proportional controller are used.

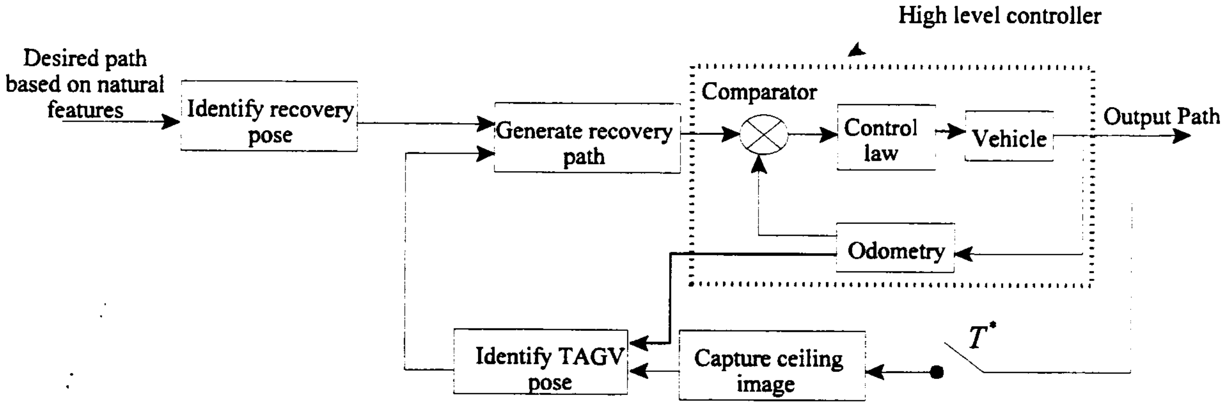

T^*: is the time generated by the system clock

Figure 6.1: TAGV navigational system block diagram

6.2 Camera/World Transformation and Pose Extraction

The knowledge of the mobile robot environment is provided in this work by a vision-based navigational system. The system is used to provide the required information about the path that the tracked vehicle should follow in real-time. The system is based on a commercial CCD camera mounted on the vehicle. The camera sends the frames sequence to an on board computer for processing. Salient information are extracted from the images to identify the vehicle pose with respect to natural markers in the environment.

Figure 6.2 shows a TAGV moving in world coordinates. To identify the desired path of the vehicle, it is proposed to make use of the ceiling features of a room or a corridor, for example, as natural landmarks as shown the figure. The presence of a drop-down ceiling tile grid structure makes it a good candidate for guidance landmarks [34]. The camera is assumed to have the same position as the center of the vehicle and has a fixed visual field. Figure 6.2 also shows the recovery path generated based on the vehicle current and target poses provided by the vehicle sensory system.

In order to be able to identify the vehicle pose, image analysis techniques are used to extract the required information from the image. Straight edges are extracted using Hough transformation as specific features since they can be used as clues to determine the location of the robot [7, 34]. In the specific setup used at the University of Ottawa, the ceiling tile grid contains two parallel dark lines that are used as a navigational guide. The predefined path of the vehicle is considered to be a hypothetical path lying at the center between those two lines. The extracted lines are then used to find the pose of the vehicle with respect to the world coordinate. One of the approaches that can be used to find the vehicle pose is the vanishing points approach [34] and the planar homography approach [34, 35].

Odometry information are obtained from optical encoders mounted on the DC drive motors of the mobile robot. The traveled distance of the vehicle with respect to the world coordinates is calculated from the odometry of the vehicle. The output pose of the vehicle is a future pose and is found based on transformation matrices from local coordinates of the vehicle with respect to the world coordinates. The pose is then used as the output reading of the vision-based navigational system. The total time for feedback from the vision system due to camera capture and image analysis is taken into consideration during simulations and is denoted by T^* as shown in Figure 6.1. This time delay is not a conventional control system time delay since the vehicle is expected to reach the target pose in a time longer than T^*. The time required to execute the recovery path by the vehicle is a function of the vehicle speed. If T^* is longer than the time required to execute the recovery path, then a control system time delay would exist which might cause instability to the system.

The dimensions of the field of view of the camera are assumed to be known and fixed. For stable navigation, the camera field of view must always contain the predefined path so as to be able to calculate the recovery pose. With reference to Figure 6.2, $a = (x_1, y_1)$ is a point at a given location in the field of view. The current pose of the TAGV at $c = (x_o, y_o)$ can be calculated from "*a*" and odometry. $b = (x_2, y_2)$ is a point on the navigational path. The recovery pose can be calculated from "*b*" and "*c*" and their tangents. The location of point *b* can be found by solving the resulting equation from the intersection of the line *ab* shown in the figure and the predefined path. The recovery path generated between the current vehicle pose and the recovery pose is described in the next section.

6.3 Polynomial Path Planning

The recovery path between the current and the recovery pose is generated subject to the nonholonomic constraints that have been outlined in Chapter 3.

With reference to Figure 6.2 given the initial pose of the vehicle at (x_o, y_o), the target pose at (x_2, y_2), the initial orientation θ_1, and the final orientation θ_2, a cubic polynomial is used to generate the recovery path as shown in the figure. The general form of a cubic polynomial is given by:

$$f(x) = a_o x^3 + a_1 x^2 + a_2 x + a_3 \tag{6.1}$$

Substituting the boundary conditions as obtained form the TAGV current and target poses shown in Figure 6.2 gives:

$$\begin{bmatrix} 3x_o^2 & 2x_o & 1 & 0 \\ 3x_1^2 & 2x_1 & 1 & 0 \\ x_o^3 & x_o^2 & x_o & 0 \end{bmatrix} \begin{Bmatrix} a_o \\ a_1 \\ a_2 \\ a_3 \end{Bmatrix} = \begin{bmatrix} \tan\theta_1 \\ \tan\theta_2 \\ y_0 \\ y_1 \end{bmatrix} \tag{6.2}$$

The parameters (a_o, a_1, a_2, a_3) are found by solving the set of Equations 6.2.

6.4 TAGV High Level Controller

In Chapter 5, the details of an extended SMC design were derived and the controller was applied to an inverted pendulum system. The inverted pendulum is a SIMO control system. If the translational velocity of the vehicle V is considered constant and fixed, the TAGV is also SIMO system. Hence, the extended SMC used for the inverted pendulum system can be applied to the TAGV model as the high level controller shown in Figure 3.7.

With reference to Figure 6.2, both the current and the target poses of the vehicle are gleaned from the vision system and are used to generate the controller signal. Given that the TAGV speed is fixed, the signal is in the form of the required rotational velocity of the vehicle as shown in Figure 6.3. From the translational and rotational velocities, the required angular speeds of the left and right tracks DC motors can be calculated from the vehicle kinematic equations derived in Chapter 3.

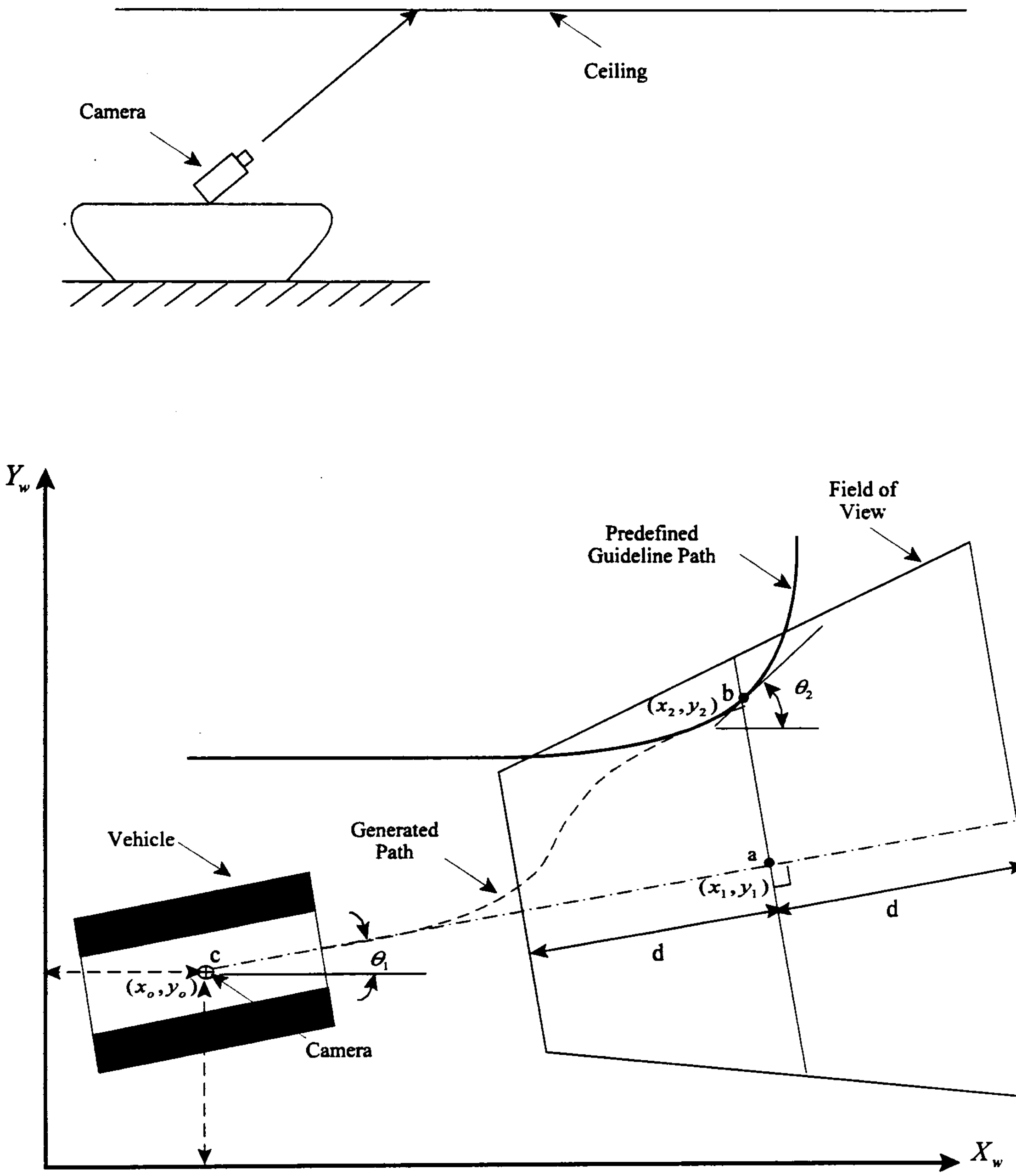

Figure 6.2: TAGV navigational system

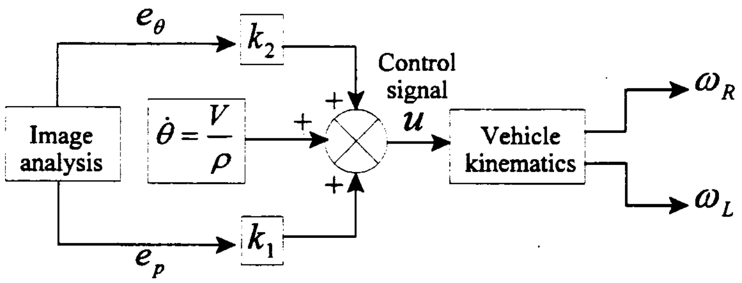

Figure 6.3: Control law block diagram

Similar to the case of the decoupled SMC used for the pendulum, two independent sliding surfaces related to the lateral position and the heading angle errors of the vehicle are used here. The lateral position error is calculated as the difference in the *y*-direction between the recovery path and the current location of the vehicle with respect to the local coordinates of the vehicle. The heading angle error is calculated as the difference between the angle found from the recovery path slope and the current direction of the vehicle with respect to the world coordinates. The sliding surfaces equations are formulated as follows:

$$s_1 = \lambda_1 e_p + \dot{e}_p \tag{6.3}$$

$$s_2 = \lambda_2 e_\theta + \dot{e}_\theta \tag{6.4}$$

where,

e_p, e_θ	are the lateral position and the heading angle errors of the vehicle respectively
$\dot{e}_p$, $\dot{e}_\theta$	are the rate of change of the vehicle lateral position and heading angle errors respectively
λ_1, λ_2	are the slopes of the sliding surfaces related to the vehicle position and heading angle respectively

The control signal depends on the vehicle errors mentioned earlier. However, if the errors are zeros, the control signal is also zero and as a result the vehicle stops moving. Since the purpose is to track a predefined path, a set point must be given to the controller to keep the vehicle moving and following the path even in the absence of errors. As mentioned earlier the drive motors rotational speeds are calculated from the vehicle rotational velocity $\dot{\theta}$ using Equation 3.5.

It should be noted that V is the vehicle translational velocity and is fixed. The radius of curvature ρ at any point along the recovery path is obtained from Equation 6.1 as follows:

$$\rho = \frac{\left[1 + \left(\frac{df(x)}{dx}\right)^2\right]^{3/2}}{\frac{d^2 f(x)}{dx^2}} \tag{6.5}$$

$\dot{\theta}$ is used as the set point of the controller. The control signal u is hence given by:

$$u = \frac{V}{\rho} + k_1 e_p + k_2 e_\theta \tag{6.6}$$

noting that

$$k_1 = \begin{cases} +\eta_1, & s_1 > 0 \\ -\eta_1, & s_1 < 0 \end{cases} \tag{6.7}$$

$$k_2 = \begin{cases} +\eta_2, & s_2 > 0 \\ -\eta_2, & s_2 < 0 \end{cases} \tag{6.8}$$

where,

k_1, k_2	are the controller gains for the vehicle position and heading angle errors respectively
η_1, η_2	are the magnitude of the controller gains corresponding to k_1 and k_2 respectively

Equation 4.20 provides the relationship between the sliding surface and the controller gain. For the case of the TAGV, the application of that equation provides two relationships as follows:

$$k_1 = \frac{1}{2}\beta_1\lambda_1^2 + \Gamma_1\lambda_1 + \frac{1}{2}\alpha_1 \tag{6.9}$$

$$k_2 = \frac{1}{2}\beta_1\lambda_2^2 + \Gamma_2\lambda_2 + \frac{1}{2}\alpha_2 \tag{6.10}$$

The methodology developed in Section 4.5 for finding the coefficients β, α, and Γ of Equations 6.10 and 6.9 is used here. It entails comparing these equations to Equations 3.12 and 3.13. The following similarities are obtained:

$$\begin{aligned} k_1 &= \frac{1}{2}\beta_1\lambda_1^2 + \Gamma_1\lambda_1 + \frac{1}{2}\alpha_1 \\ &= \frac{1}{2}m{\lambda_1}^2 \end{aligned} \tag{6.11}$$

$$\begin{aligned} k_2 &= \frac{1}{2}\beta_2\lambda_2^2 + \Gamma_2\lambda_2 + \frac{1}{2}\alpha_2 \\ &= \frac{1}{2}I_z{\lambda_2}^2 \end{aligned} \tag{6.12}$$

where I_z and m are the mass moment of inertia of the vehicle about the vertical axis passing through its center of mass, and the mass of the vehicle respectively.

For each of the two relationships one of the parameters, either λ_i or k_i, has to be chosen and the other calculated. Alternatively, additional constraints have to be found in order to guide the choice of the parameters. The system sensitivity analysis again is used here to find such constraints. With reference to Chapter 3, the rotational velocity of the vehicle is given by Equation 3.9. Equating Equation 6.6 to Equation 3.9 gives:

$$\frac{V}{\rho} + k_1 e_p + k_2 e_\theta = \frac{r}{B}(\omega_{R(out)} - \omega_{L(in)}) \tag{6.13}$$

Taking the partial derivative of the lateral position error e_p of the vehicle with respect to the DC motors angular speeds in Equation 6.13 results in:

$$\frac{\partial e_p}{\partial \omega_{R(out)}} = \frac{k_1 B}{r} \tag{6.14}$$

$$\frac{\partial e_p}{\partial \omega_{L(in)}} = -\frac{k_1 B}{r} \tag{6.15}$$

Taking the partial derivative of the direction error e_θ of the vehicle with respect to the DC motors angular speeds in Equation 6.13 gives:

$$\frac{\partial e_\theta}{\partial \omega_{R(out)}} = \frac{k_2 B}{r} \tag{6.16}$$

$$\frac{\partial e_\theta}{\partial \omega_{L(in)}} = -\frac{k_2 B}{r} \tag{6.17}$$

In order that the TAGV errors are rendered insensitive to the motors angular speed variations, the magnitude of the denominator of Equations 6.14-6.17 must be larger than that of the numerators, i.e.,

$$k_1 < B / r \tag{6.18}$$

$$k_2 < B / r \tag{6.19}$$

Equations 6.18 and 6.19 are used to guide the choice of the SMC gains of the TAGV.

6.5 Boundary Layer Technique

The control law of Equation 6.6 is discontinuous across the sliding surfaces s_1, s_2 and leads to perfect tracking. However, this is obtained at the cost of high controller activity, i.e, control chattering. In general chattering is undesirable and should be minimized or eliminated for practical controller implementations. As proposed by Utkin [27] and Slotine [17], this can be achieved by using a thin boundary layer on either sides of the sliding surfaces and using a saturation function instead of the sign function used in the previous SMC law.

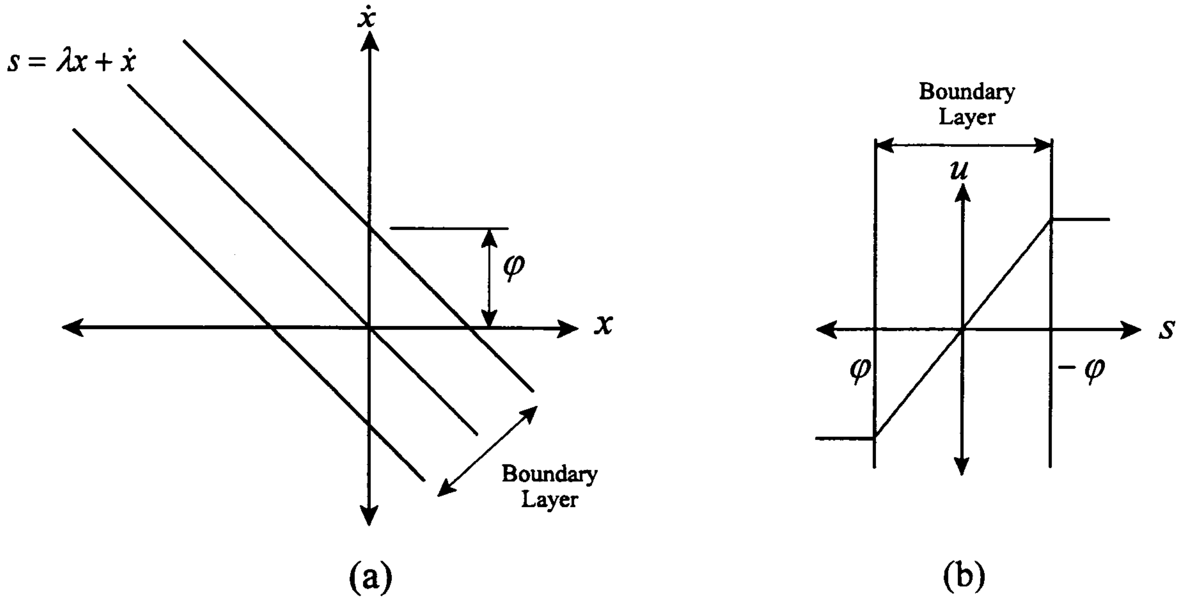

(a) (b)

Figure 6.4: The boundary layer

Figure 6.4 (a) shows a boundary layer neighboring the sliding surface *s=0*. If the state of the system is outside the boundary layer, the control law *u* is chosen as before to be a relay type controller. If the state of the system is inside the boundary layer, the control law *u* is interpolated by replacing the sign function in the expression of *u* by s / φ as illustrated in Figure 6.4 (b). In other words, the sign function of a regular rely type control law *u* is replaced by the following saturation function:

$$sat(s) = \begin{cases} \operatorname{sgn}(s), & |s| > \varphi \\ \dfrac{s}{\varphi}, & |s| \le \varphi \end{cases} \tag{6.20}$$

6.6 Simulation Results and Comparisons

In order to emphasize the significance of the slip on the vehicle motion, the TAGV is commanded to move along a circular path with the navigational system disconnected, i.e., in open-loop mode. Figure 6.5 shows this turning behavior for a turning radius of 3 meters, a translational velocity of 0.8 *m/sec*, and different slip values of the outer track with no slip of the inner track. Unequal track slip may result due to many factors, among them unsymmetrical loads distribution on the TAGV. This condition has been chosen since it is among those that produce the worst tracking error. A shift between the given input path and the output paths corresponding to the different slip values can be seen. As expected, larger errors correspond to higher slip. This shift, or error, should be detected and corrected by the vehicle navigational system.

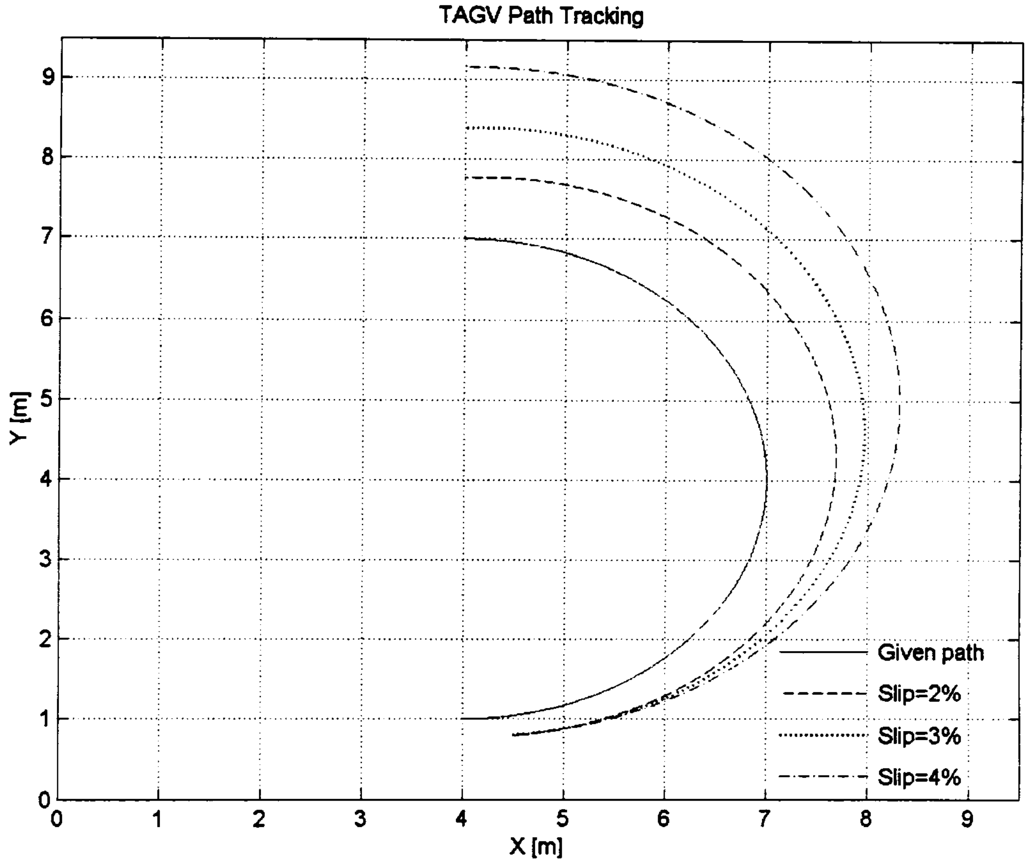

Figure 6.5: Open-loop TAGV path tracking

Substituting the vehicle parameters in Table 3.1 into Equations 6.11, 6.12, 6.18, and 6.19 results in the following relationships between k_1, λ_1, k_2, and λ_2:

$$k_1 = 26\lambda_1^2 \tag{6.21}$$

$$k_2 = 4.45\lambda_2^2 \tag{6.22}$$

$$k_1 << 8.6 \tag{6.23}$$

$$k_2 << 8.6 \tag{6.24}$$

Noting that Equations 6.21 and 6.22 give the lower power limit required to reach a target pose. Increasing the slopes of the sliding surfaces increases the system energy, and a faster response of the system is achieved.

Figure 6.6 shows comparative simulation results for three controllers. The first is the proportional controller of Equation 6.6 with the gains k_1 and k_2 being positive constants. The second is a SMC where the gains are selected to be $k_1 = \pm 5, k_2 = \pm 5$ based on the parameter limitations of Equations 6.23 and 6.24. The corresponding slopes of the selected gains are $\lambda_1 = 0.44\,\mathrm{sec}^{-1}$ and $\lambda_2 = 1.1\,\mathrm{sec}^{-1}$. The third controller is again a SMC with gains $k_1 = \pm 5, k_2 = \pm 5$ and slopes $\lambda_1 = 0.44\,\mathrm{sec}^{-1}, \lambda_2 = 10\,\mathrm{sec}^{-1}$. The translational velocity of the vehicle is set to 0.8 *m/sec*, the turning radius is 3 meters, and the tracks are assumed to experience no slip. With reference to the discussion of the time delay issue in Section 6.2, the total time delay due to the camera and image analysis is approximated to be 0.5 *sec* in the simulation, while the minimum time required to execute the recovery path is approximated to be 0.93 *sec* based on the vehicle speed limit. Consequently, the time of image acquisition and analysis cannot be considered as a time delay. The boundary layer is also used with $\varphi = 0.1$ for both sliding surfaces. Figures 6.7 and 6.8 are blow-ups of the regions (A) and (B) of Figure 6.6 respectively. Figure 6.7 shows that the proportional controller is by far the most aggressive in guiding the TAGV between the current and the target poses. However, it overshoots the path required to be tracked, and it moves along the inside of the curvature with a steady state error of *16 mm* as can be seen in Figure 6.8. The proportional controller is unable to return the vehicle back after it overshoots since the target pose is a pose in the future and is changing continuously while the vehicle is moving and hence this results in a steady state error. The response due to the SMC with the smaller sliding surfaces slopes ($\lambda_1 = 0.44\,\text{sec}^{-1}$, $\lambda_2 = 1.1\,\text{sec}^{-1}$) is the slowest. It seems to diverge initially and then recovers and tracks the curved path on its outside. This controller exhibits the worst steady state error (*24 mm*). The response due to the SMC with $\lambda_1 = 0.44\,\text{sec}^{-1}$ and $\lambda_2 = 10\,\text{sec}^{-1}$ is the best as far as tracking. Its steady state error is *2.8 mm*. Its progression towards the required curved path is marginally slower than that due to the proportional controller.

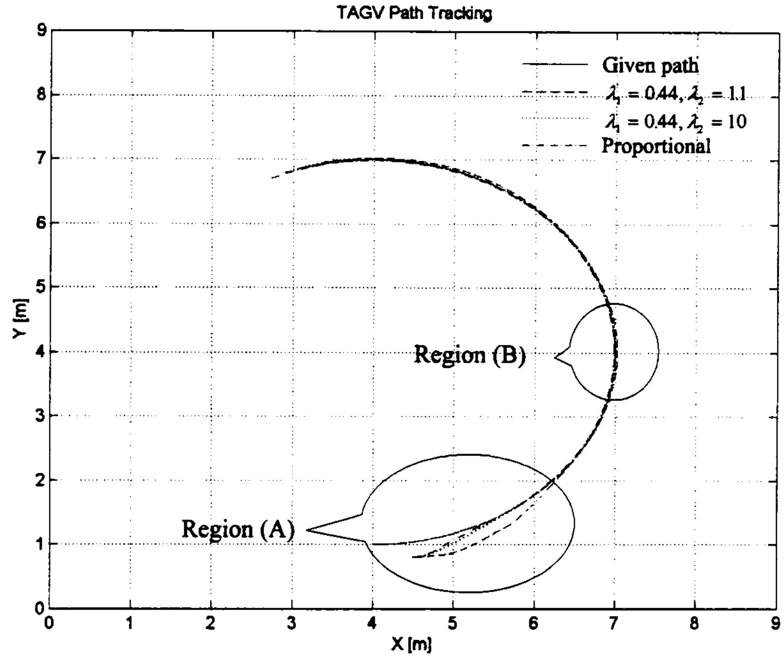

Figure 6.6: Comparison of P-controller and Decoupled SMC for the TAGV with 0% slip

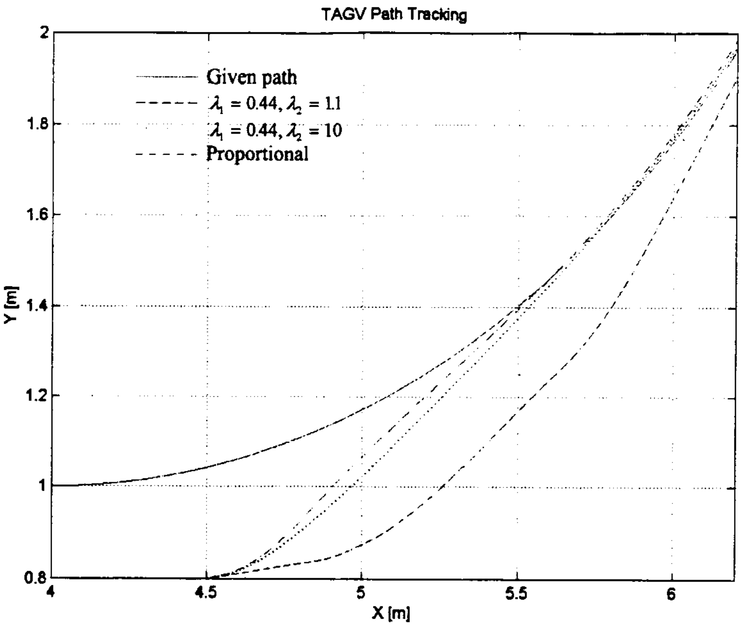

Figure 6.7: Comparison of P-controller and Decoupled SMC for the TAGV with 0% slip. Region (A) of Figure 6.6

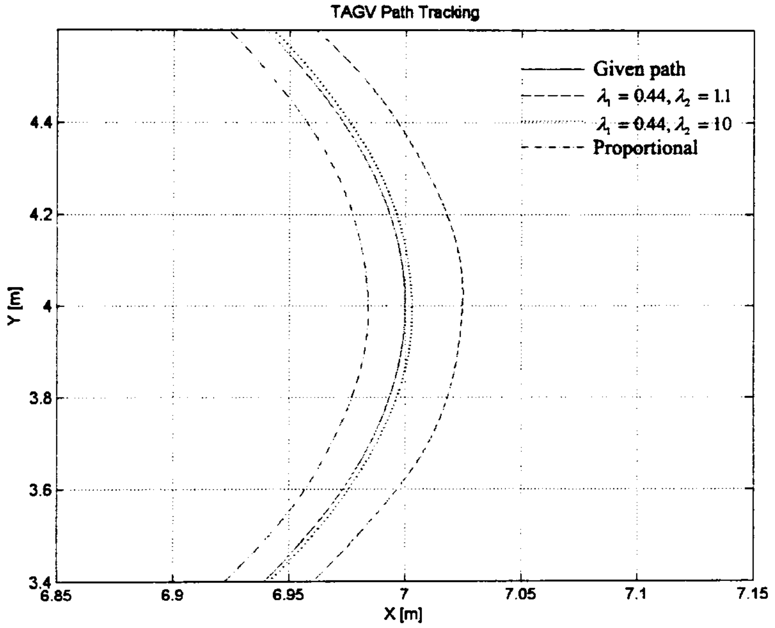

Figure 6.8: Comparison of P-controller and Decoupled SMC for the TAGV with 0% slip. Region (B) of Figure 6.6

When a 2% outer track slip is introduced, the resulting tracking performance is shown in Figure 6.9 for the same proportional controller gains used before, i.e., $k_1 = k_2 = 5$, and the better of the two SMCs from the previous simulation with $\lambda_1 = 0.44$ and $\lambda_2 = 10$. Results due to the use of an additional SMC with $\lambda_1 = 2$ and $\lambda_2 = 20$ are also shown in the figure. Figures 6.10 and 6.11 show blow-ups of the regions (A) and (B) of Figure 6.9 respectively. Again, the results in this case mirror those of the previous simulations. The TAGV with the proportional controller is the fastest to converge, but overshoots the target circular path and then tracks the path at a constant offset to its inside. The results due to the two SMCs produce similar performances, be it the one with the higher sliding surfaces converges faster and results in less steady state error. The steady state errors for the proportional controller, the lower and higher heading angle sliding surface slopes are *13 mm*, *7.5 mm*, and *3 mm* respectively.

As track slip increases the error between the given path and the output path increases as shown in Figures 6.12- 6.17. The responses is for slip values of the outer track of 3% and 4% respectively. The controllers used here are the same ones of the previous case of 2% slip. Figures 6.13-6.14 and 6.16-6.17 show blow-ups of the regions (A) and (B) of Figures 6.12 and 6.15 respectively. A similar trend to that of the case of the 2% outer track slip is observed in these figures. The TAGV with the proportional controller is the fastest to converge, but overshoots the target circular path and remains at an offset to its inside. The TAGV with the higher SMC slopes converges towards the target circular path faster than the one with the low slopes, and a smaller steady state error is produced. The steady state error due to the proportional controller, the lower and higher heading angle sliding surface slopes for the 3% case are *11 mm*, *9 mm*, and *5 mm* respectively. The 4% track slip case produces the worst steady state errors. The steady state errors for the proportional controller, the lower and higher heading angle sliding surface slopes are *9 mm*, *11 mm*, and *8.5 mm* respectively.

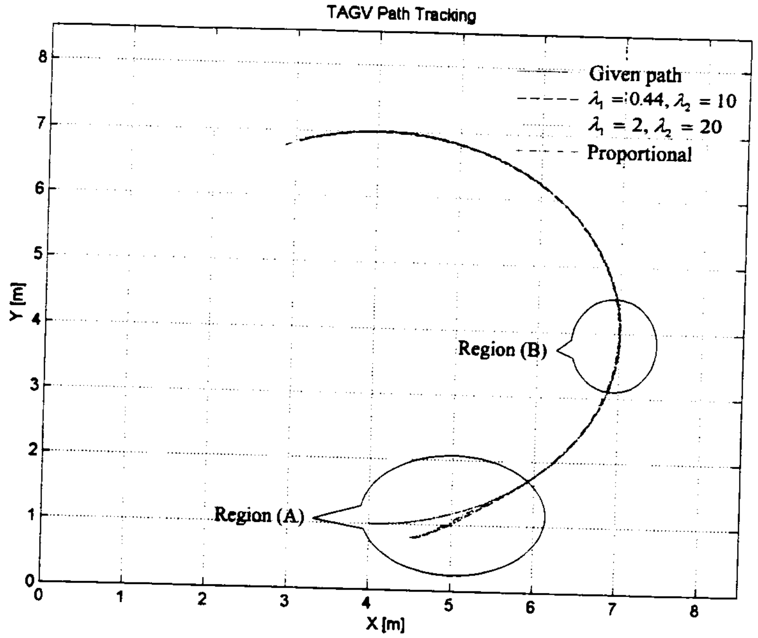

Figure 6.9: Comparison of P-controller and Decoupled SMC for the TAGV with 2% slip

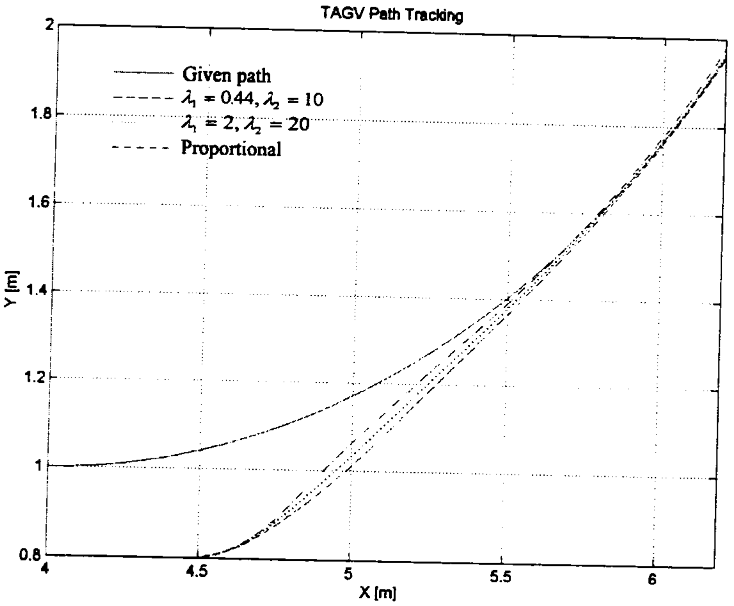

Figure 6.10: Comparison of P-controller and Decoupled SMC for the TAGV with 2% slip. Region (A) of Figure 6.9

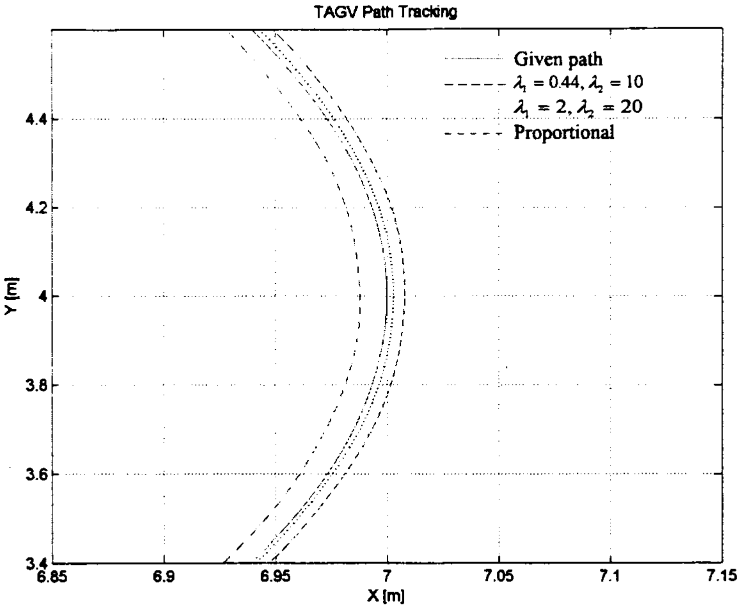

Figure 6.11: Comparison of P-controller and Decoupled SMC for the TAGV with 2% slip. Region (B) of Figure 6.9

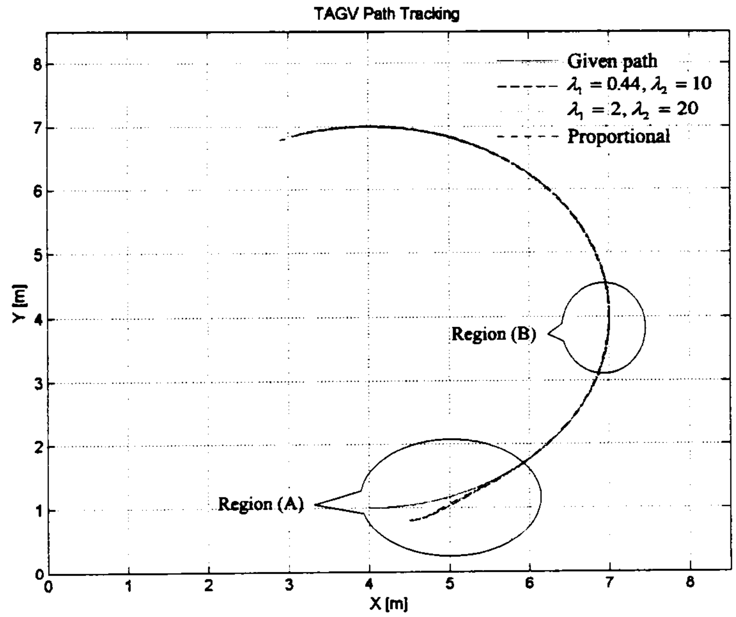

Figure 6.12: Comparison of P-controller and Decoupled SMC for the TAGV with 3% slip

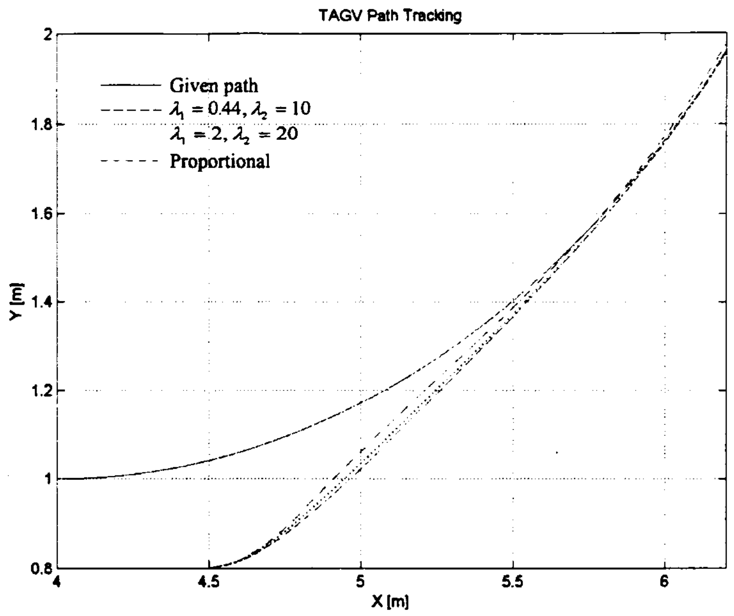

Figure 6.13: Comparison of P-controller and Decoupled SMC for the TAGV with 3% slip. Region (A) of Figure 6.12

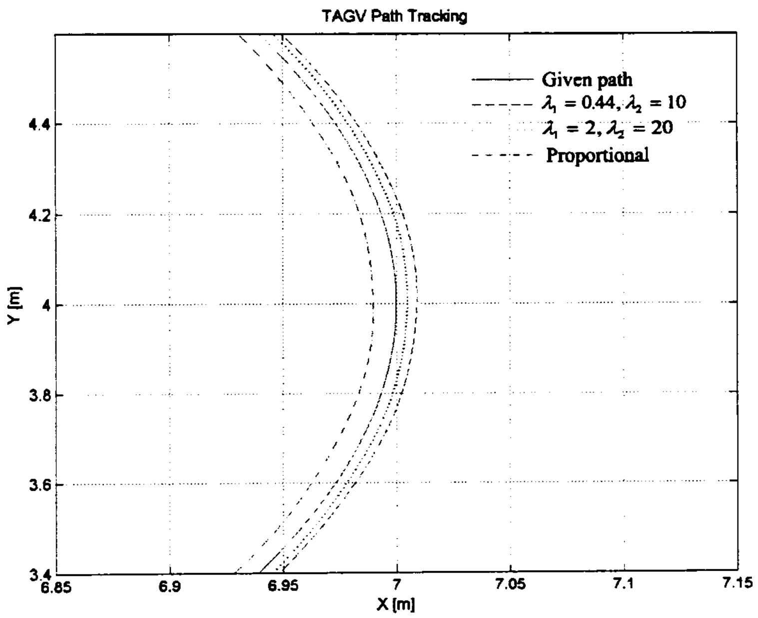

Figure 6.14: Comparison of P-controller and Decoupled SMC for the TAGV with 3% slip. Region (B) of Figure 6.12

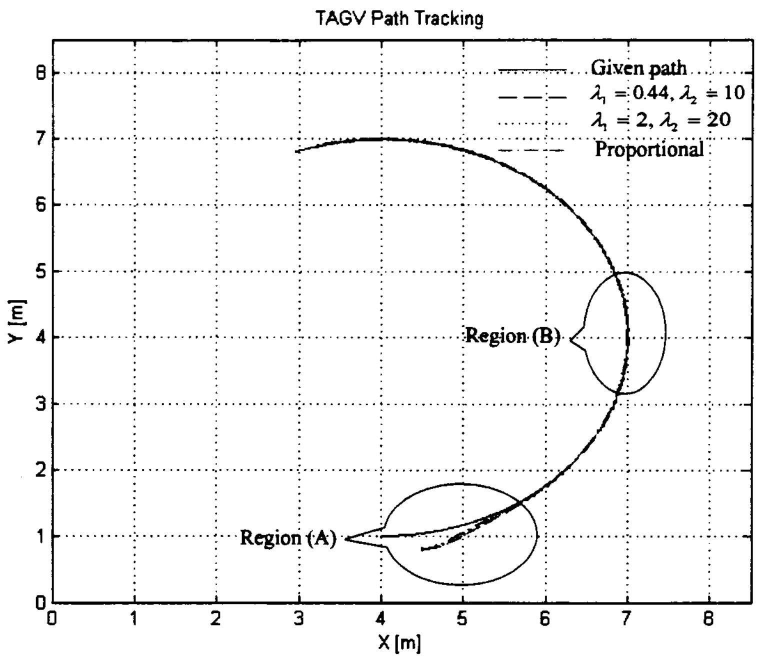

Figure 6.15: Comparison of P-controller and Decoupled SMC for the TAGV with 4% slip

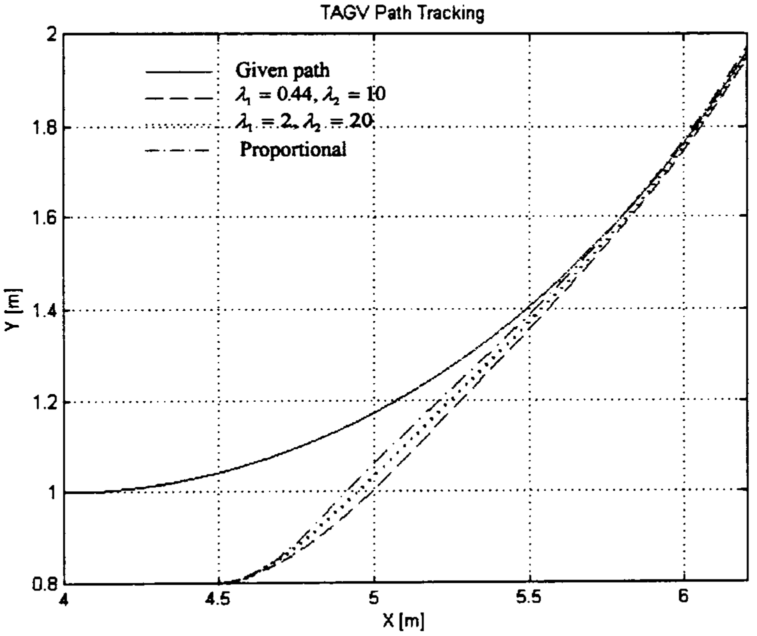

Figure 6.16: Comparison of P-controller and Decoupled SMC for the TAGV with 4% slip. Region (A) of Figure 6.15

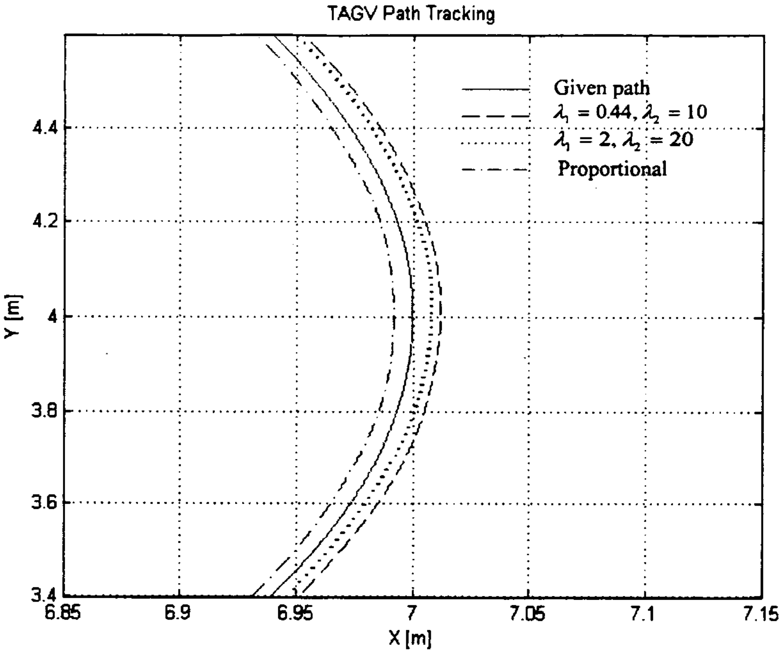

Figure 6.17: Comparison of P-controller and Decoupled SMC for the TAGV with 4% slip. Region (B) of Figure 6.15

6.7 SMC Using Hyper Sliding Surface

6.7.1 Controller Design

In this section, the sliding mode controller is designed such that the independent decoupled sliding surfaces of the position and the direction errors of the TAGV are coupled together to form a hyper sliding surface s. The hyper sliding surface has the following form:

$$s = s_1 + s_2 \tag{6.25}$$

where s_1 and s_2 are the sliding surfaces of the TAGV SMC used before.

Substituting Equations 6.3 and 6.4 for s_1 and s_2 into Equation 6.25 gives:

$$s = \lambda_1 x + \dot{x} + \lambda_2 \theta + \dot{\theta} \tag{6.26}$$

The control law of the SMC with the hyper surface is similar to that developed in Section 6.4 given by Equation 6.6. The controller gains are given as follows:

$$k_1 = \begin{cases} +\eta_1, & s > 0 \\ -\eta_1, & s < 0 \end{cases} \tag{6.27}$$

$$k_2 = \begin{cases} +\eta_2, & s > 0 \\ -\eta_2, & s < 0 \end{cases} \tag{6.28}$$

where,

k_1, k_2	are the controller gains for the vehicle position and heading angle errors respectively
η_1, η_2	are the magnitude of the controller gains corresponding to k_1 and k_2 respectively

The controller gains k_1 and k_2 are selected as before based on Equations 6.23 and 6.24 respectively.

6.7.2 Simulation Results and Comparisons

Figure 6.18 shows the path tracking performance of the TAGV when controlled using three types of controllers; the SMC with decoupled sliding surfaces, the SMC with hyper sliding surface, and the proportional controller. For comparison purposes, the SMC with the higher sliding surfaces slopes $\lambda_1 = 2$, $\lambda_2 = 20$, and the proportional controller with controller gains $k_1 = 5$ and $k_2 = 5$ are again used here. The SMC gains are the same ones used earlier ($k_1 = \pm 5$, $k_2 = \pm 5$). The figure is for a slip of 2% of the outer track of the vehicle. Figures 6.19 and 6.20 show blow-ups of regions (A) and (B) of Figure 6.18. The tracking performance for the cases of 3% and 4% slip values are shown in Figures 6.21 and 6.24 respectively. The corresponding Figures 6.22-6.23 and 6.25-6.26 are the blow-ups of regions (A) and (B) for both cases respectively. The figures clearly show that the SMC with the hyper surface has a better performance than that of the SMC with decoupled surfaces and that of the proportional controller. The response of the SMC with the hyper surface is faster to converge towards the target circular path than that of the SMC with decoupled surfaces. Its progression is marginally slower than that of the proportional controller. The steady state error for the 2% case using the proportional controller, the decoupled sliding surfaces, and the hyper sliding surface are *13mm*, *3mm*, and *0.7mm* respectively whereas the error corresponding to the 3% case for the same controllers are *11mm*, *5mm*, and *2mm* respectively. The 4% case errors for same controllers are *9mm*, *8.5mm*, and *4mm* respectively.

Table 6.1 shows a summary of the steady state tracking errors of the TAGV while controlled by the proportional controller, the SMC controller with decoupled surfaces, and the SMC with the hyper sliding surface. A negative error indicates that the vehicle tracks the target circular path on its inner side whereas a positive error indicates that the vehicle tracks the path on its outer side. The error is measured in *mm*. The table shows that the results due to the SMC with higher sliding surfaces are better than those of the proportional controller. The results due to the SMC with the hyper sliding surface show the superiority of that controller when compared to those of the proportional controller and the decoupled SMCs.

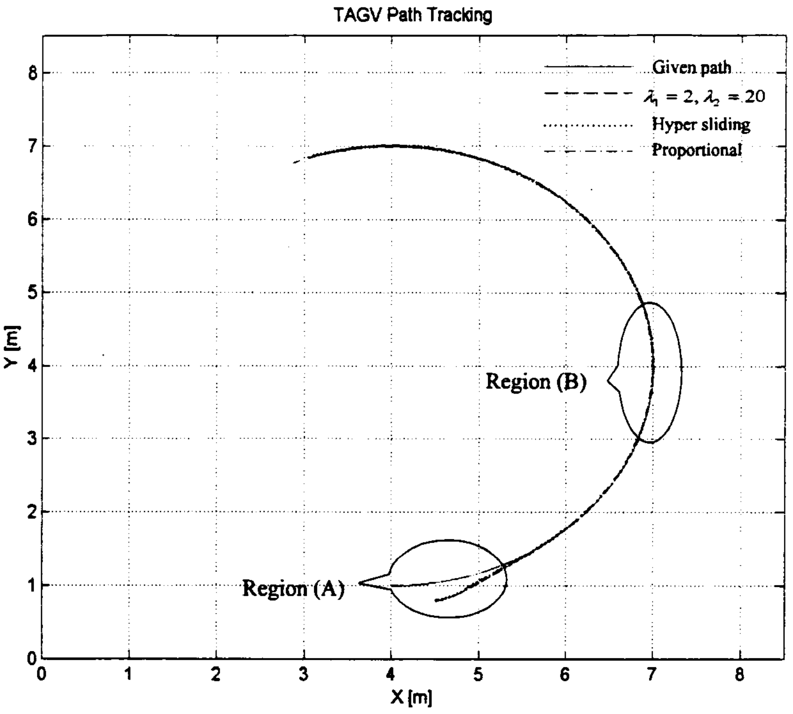

Figure 6.18: Comparison of P-controller and Hyper SMC for the TAGV with 2% slip

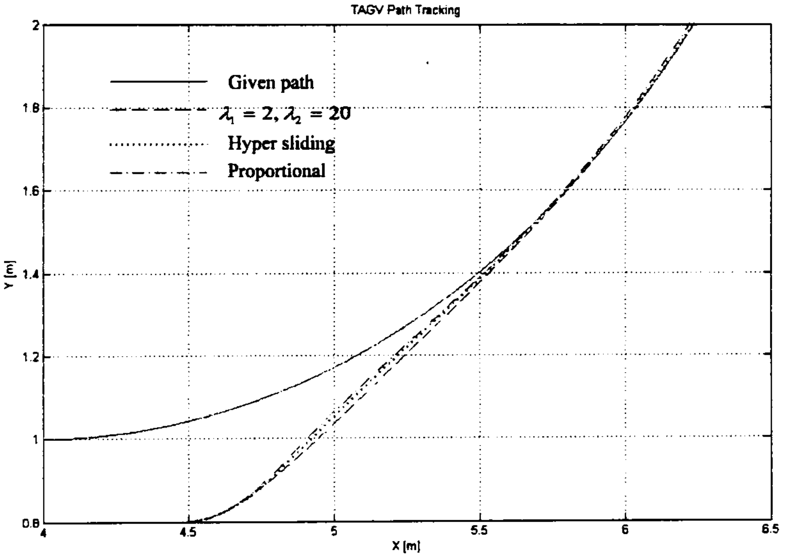

Figure 6.19: Comparison of P-controller and Hyper SMC for the TAGV with 2% slip. Region (A) of Figure 6.18

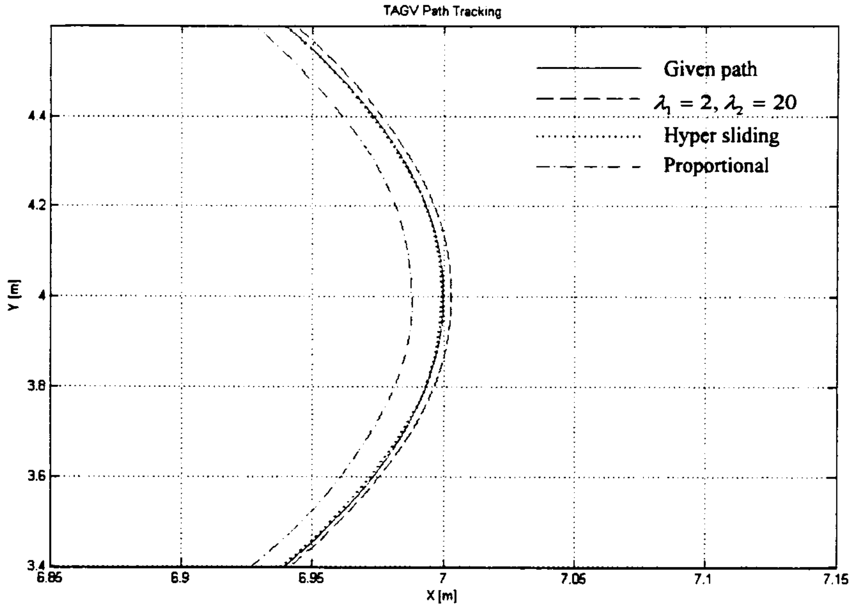

Figure 6.20: Comparison of P-controller and Hyper SMC for the TAGV with 2% slip. Region (B) of Figure 6.18

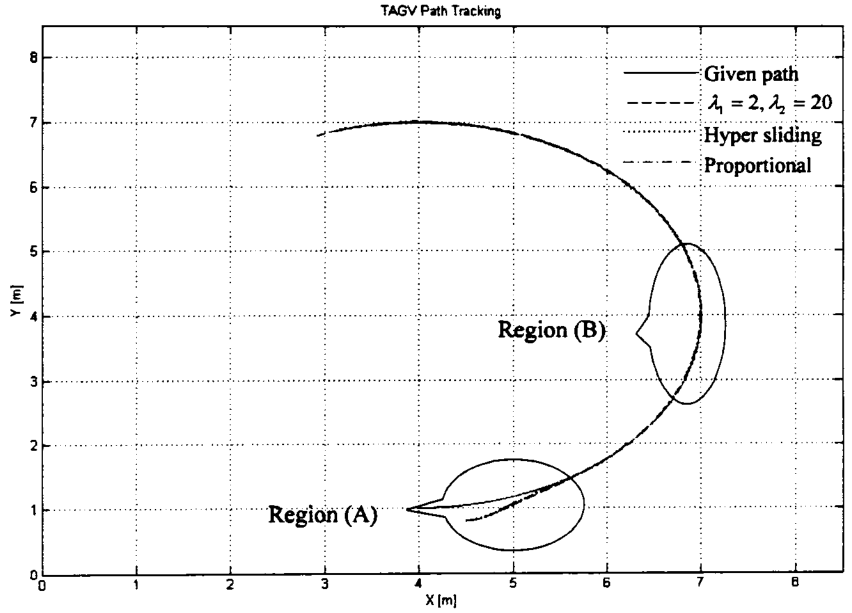

Figure 6.21: Comparison of P-controller and Hyper SMC for the TAGV with 3% slip

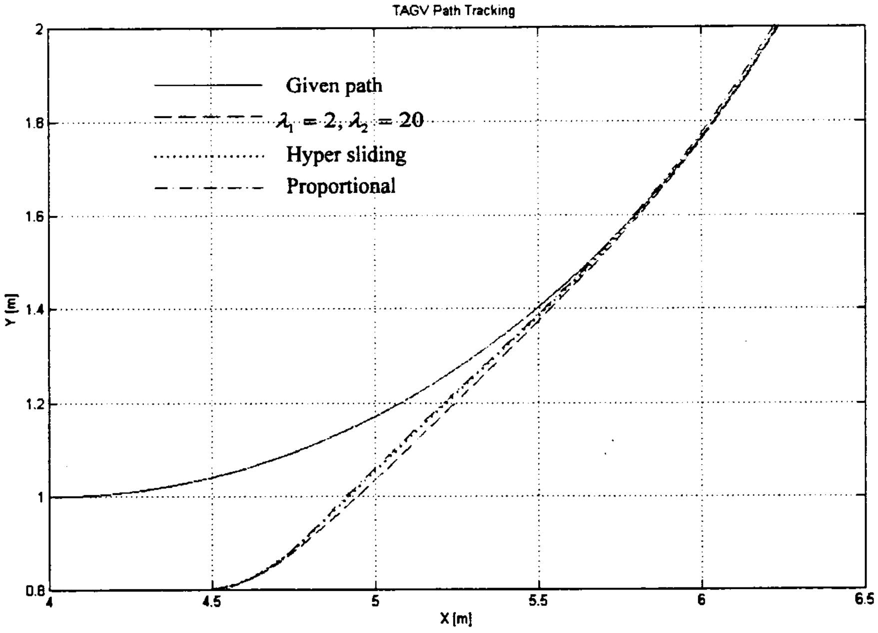

Figure 6.22: Comparison of P-controller and Hyper SMC for the TAGV with 3% slip. Region (A) of Figure 6.21

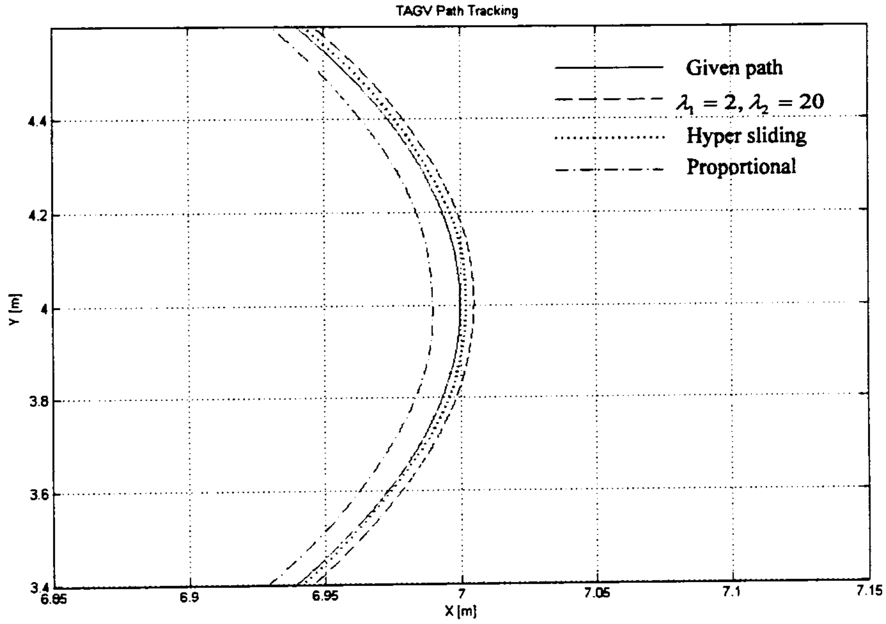

Figure 6.23: Comparison of P-controller and Hyper SMC for the TAGV with 3% slip. Region (B) of Figure 6.21

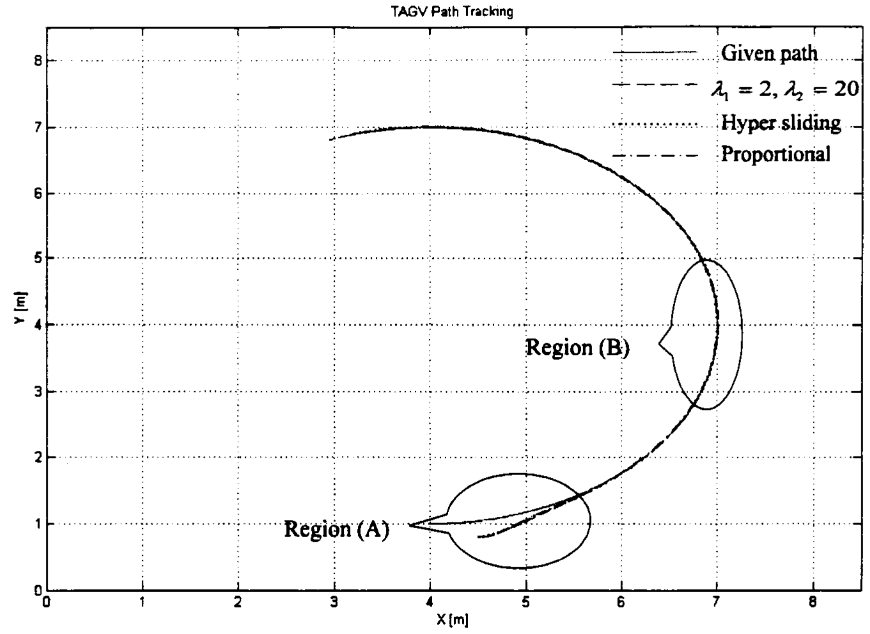

Figure 6.24: Comparison of P-controller and Hyper SMC for the TAGV with 4% slip

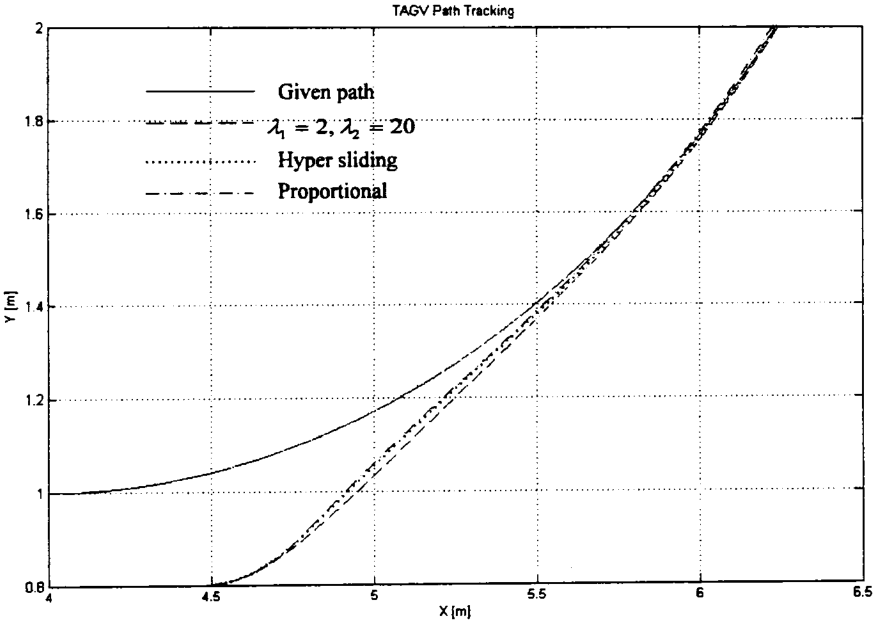

Figure 6.25: Comparison of P-controller and Hyper SMC for the TAGV with 4% slip. Region (A) of Figure 6.24

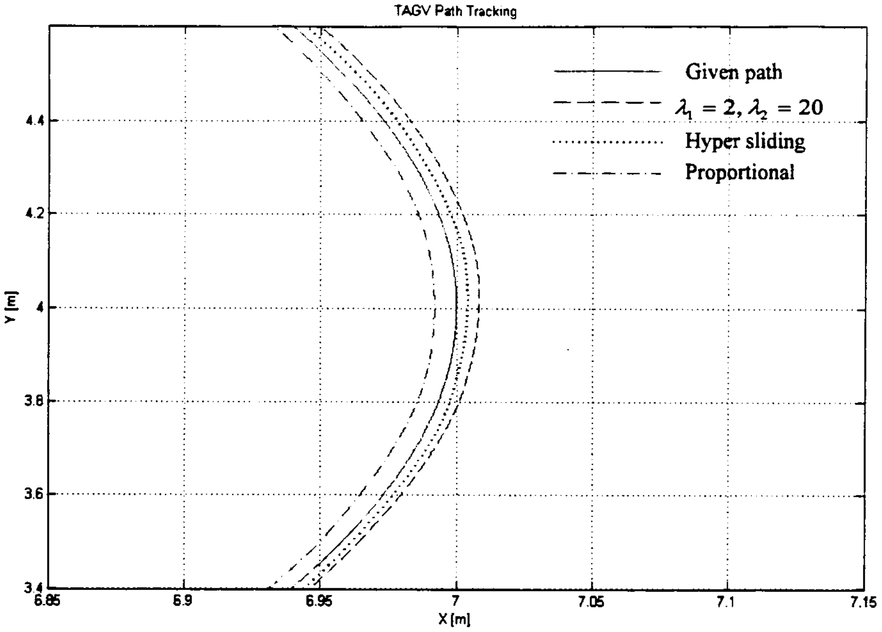

Figure 6.26: Comparison of P-controller and Hyper SMC for the TAGV with 4% slip. Region (B) of Figure 6.24

Table 6.1: Summary of the TAGV position error results

Vehicle position error *(mm)*

Slip Control law		0%	2%	3%	4%
SMC	$\lambda_1 = 0.44$ $\lambda_2 = 1.1$	+24.0	N/A	N/A	N/A
	$\lambda_1 = 0.44$ $\lambda_2 = 10$	+2.8	+7.5	+9.0	+11.0
	$\lambda_1 = 2$ $\lambda_2 = 20$	N/A	+3.0	+5.0	+8.5
	Hyper sliding surface	N/A	-0.7	+2.0	+4.0
Proportional		-16.0	-13.0	-11.0	-9.0

6.8 Effect of Changes in the Operating Conditions on the Performance of the TAGV

In the previous section, the performance of the TAGV when controlled by the hyper surface SMC was shown to be consistently better than all the cases where other controllers were used. The results however were for a specific set of operating conditions (radius of curvature and vehicle speed). In this section, the performance is assessed for different operating conditions, and compared to a traditional proportional controller with comparable gain. The simulations are carried out for different values of the radius of curvature and the translational velocity of the vehicle. Figure 6.27 shows the path tracking performance of the TAGV when controlled using the hyper surface SMC and the proportional controller used earlier. The hyper surface SMC has sliding surface slopes of $\lambda_1 = 2, \lambda_2 = 20$ and gains of $k_1 = \pm 5$, $k_2 = \pm 5$. The proportional controller is used with controller gains of $k_1 = 5$ and $k_2 = 5$. The figure is for a slip of 4% of the outer track of the vehicle. The translational velocity of the vehicle is 0.8 *m/sec*, and the turning radius is 4 meters. Figures 6.28 and 6.29 show blow-ups of regions (A) and (B) of Figure 6.27. The steady state error using the hyper surface SMC and the proportional controller are 3 *mm* and 11 *mm* respectively. The proportional controller shows similar behavior to the case of the 3 meters turning radius. Since the radius is increased to 4 meters, less centrifugal force occurs for the same translational velocity. This results in less slippage of the vehicle. With both controllers, the same trend exhibited in the previous section is again seen here. The proportional controller aggressively compensates for the slippage and is faster in correction than the hyper surface SMC (as can be seen in Figure 6.28) but overshoots the curve and tracks the desired curve on its inside at a larger error as can be seen in Figure 6.29.

The results in Figure 6.30 are for the case when the radius of curvature is reduced to 2 meters while the translational velocity is kept at 0.8 *m/sec*. Figures 6.31 and 6.32 are blow-ups of regions (A) and (B) of Figure 6.30. The steady state error using the hyper SMC and the proportional controller are 5 *mm* and 14 *mm* respectively. Reducing the turning radius to 2 meters for the same translational velocity increases the centrifugal force and hence increases the slippage of the vehicle. This increase in the centrifugal force proves to be larger than what the proportional controller can cope with, and for the first time it tracks the desired curve on the outside. The hyper surface SMC performance also deteriorates slightly due to that increase in the centrifugal force.

Figure 6.33 shows the path tracking performance of the TAGV with the same two controllers but with a TAGV translational velocity of 1.3 *m/sec.* The slip of the outer track is again set to 4% and the turning radius is set to 3 meters. Figure 6.34 and 6.35 are blow-ups of regions (A) and (B) of Figure 6.33. The steady state error using the hyper surface SMC and the proportional controller are 18 *mm* and 34 *mm* respectively. At that translational velocity, the centrifugal force reaches a sufficiently high magnitude such that the performance of the two controllers deteriorates considerably. It is noteworthy however that the error of the hyper surface SMC is almost half that of the proportional controller. Again here it can be seen that the high magnitude of the centrifugal force causes the proportional controller to track on the outside of the desired path.

Table 6.2 summarizes the results of these simulations and is augmented with some salient results from the previous section. The table shows clearly that for the reasonable translational velocity for cornering, 0.8 *m/sec*, the proportional controller error swings from -11 *mm* at a radius of curvature of 4 meters to +14 *mm* at the radius of curvature of 2 meters. The swing of the hyper surface SMC for the same conditions is from +3 *mm* to +5 *mm*.

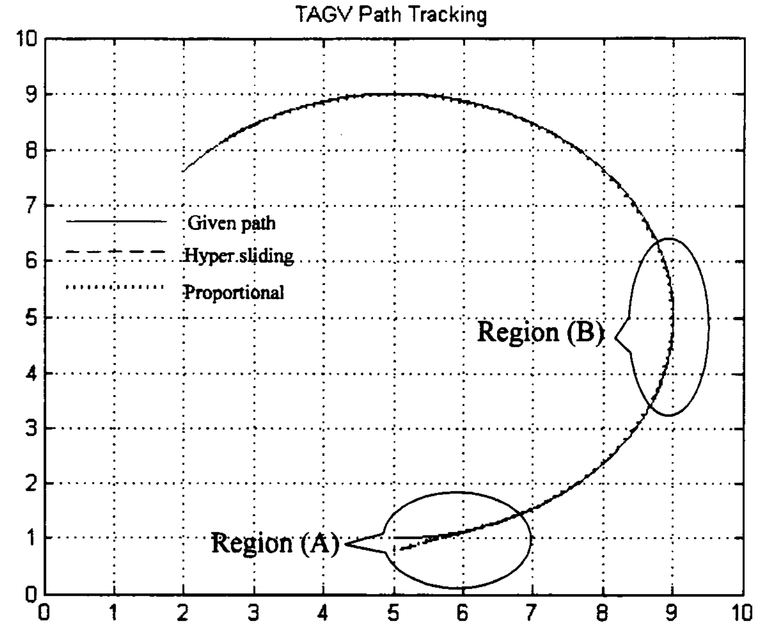

Figure 6.27: Comparison of P-controller and Hyper SMC with turning radius of *4m*

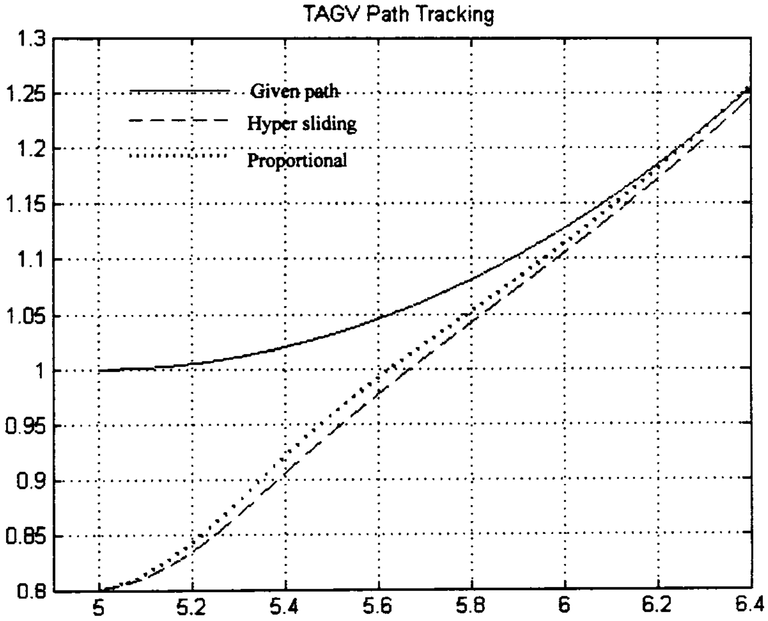

Figure 6.28: Comparison of P-controller and Hyper SMC with turning radius of *4m*. Region (A) of Figure 6.27

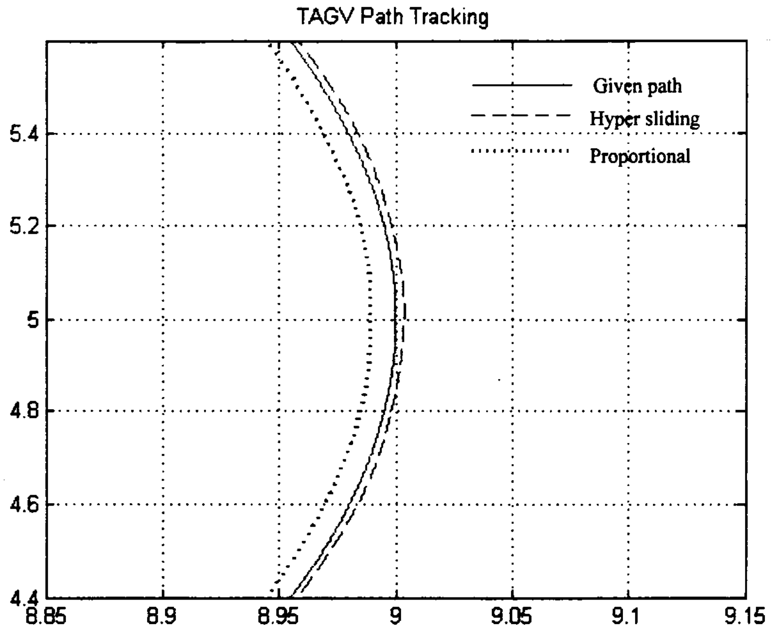

Figure 6.29: Comparison of P-controller and Hyper SMC with turning radius of *4m*. Region (B) of Figure 6.27

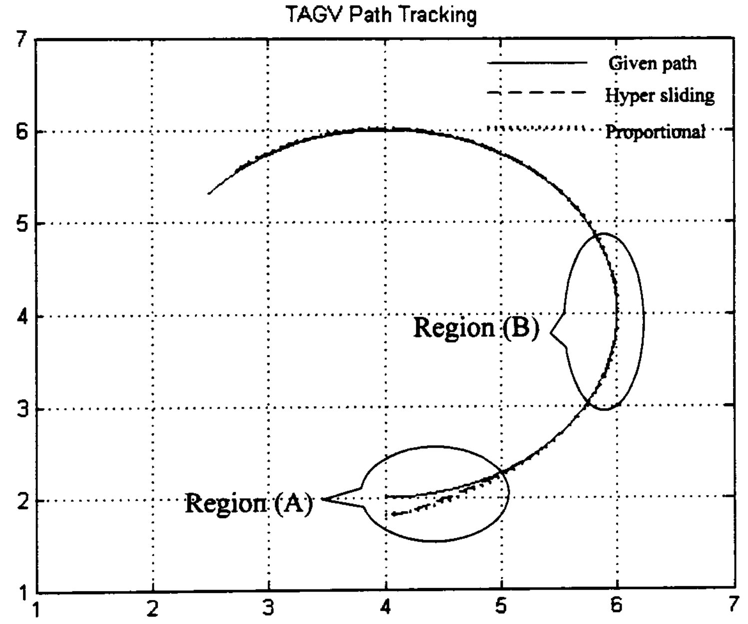

Figure 6.30: Comparison of P-controller and Hyper SMC with turning radius of *2m*

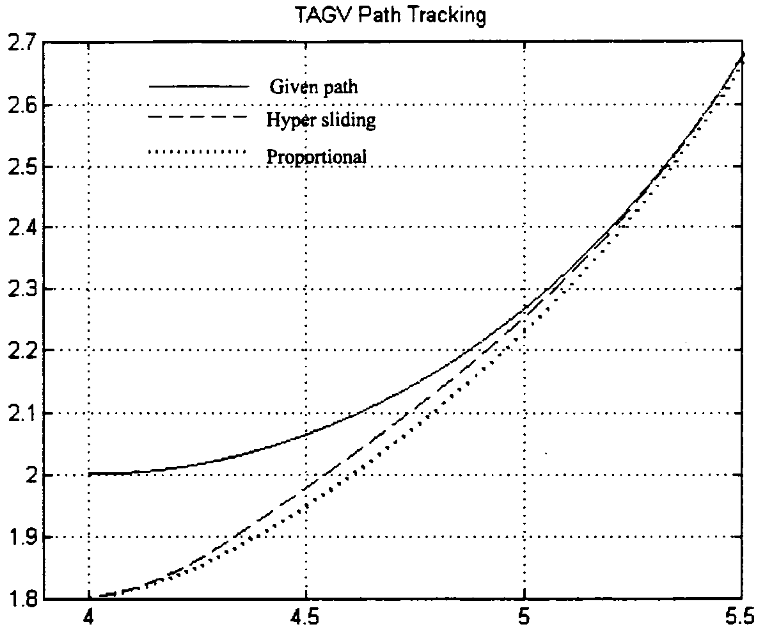

Figure 6.31: Comparison of P-controller and Hyper SMC with turning radius of *2m*. Region (A) of Figure 6.30

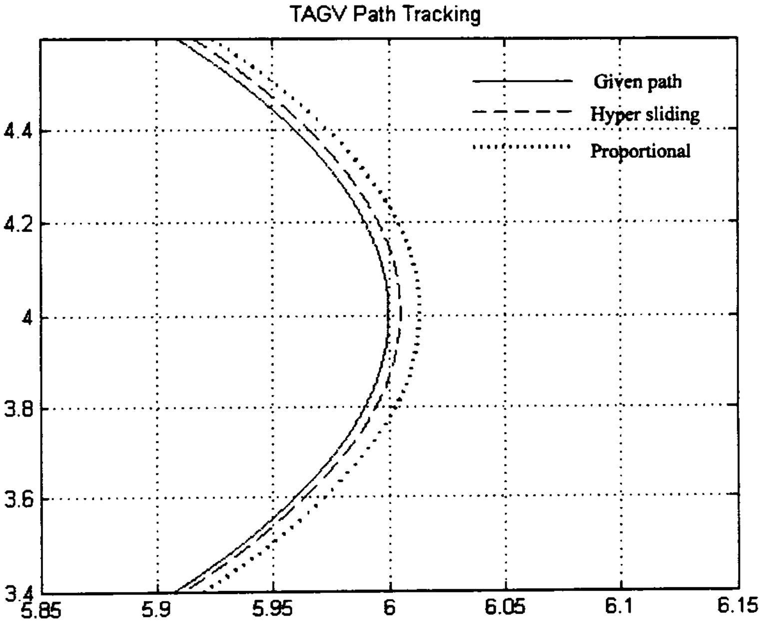

Figure 6.32: Comparison of P-controller and Hyper SMC with turning radius of *2m*. Region (B) of Figure 6.30

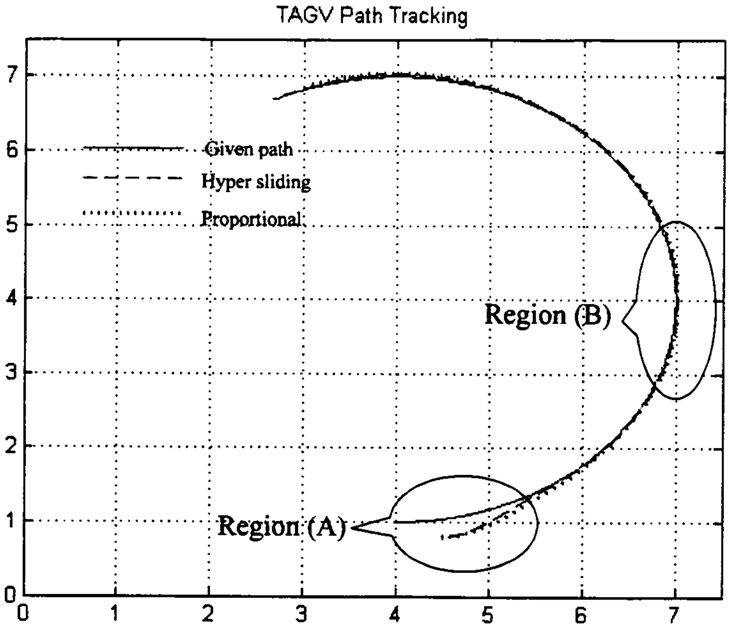

Figure 6.33: Comparison of P-controller and Hyper SMC with translational velocity of *1.3 m/sec*

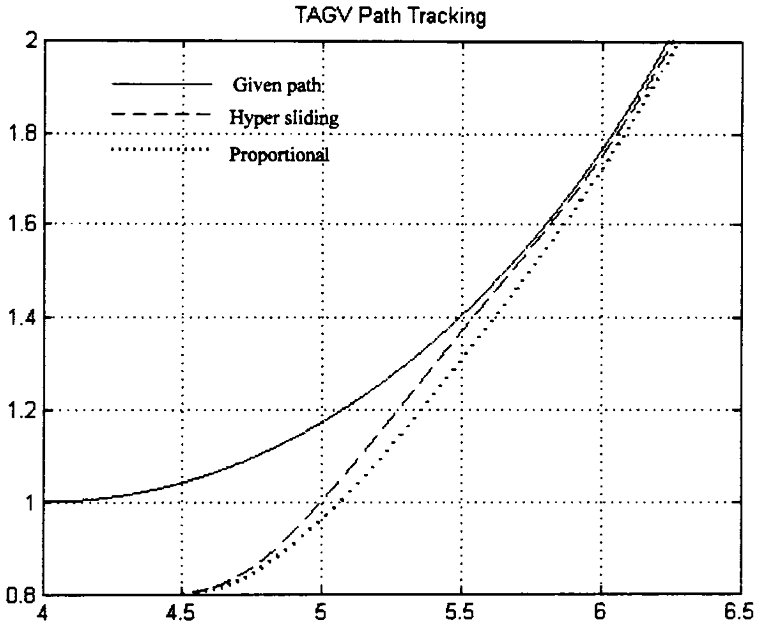

Figure 6.34: Comparison of P-controller and Hyper SMC with translational velocity of *1.3 m/sec*. Region (A) of Figure 6.33

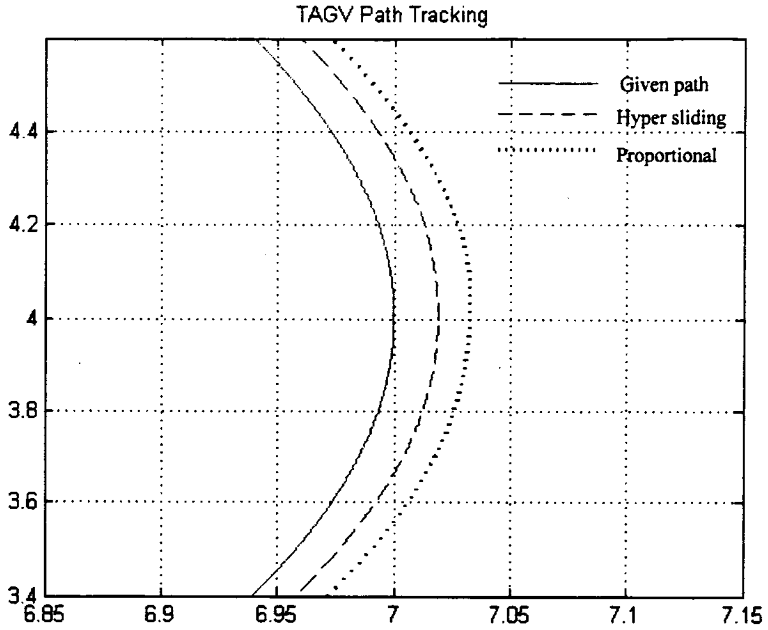

Figure 6.35: Comparison of P-controller and Hyper SMC with translational velocity of *1.3 m/sec*. Region (B) of Figure 6.33

Table 6.2: TAGV position error for different operating conditions

Vehicle position error (mm)

Velocity (*m/s*)	*V=0.8*			*V=1.3*
Radius (*m*)	*R=2*	*R=3*	*R=4*	*R=3*
Hyper SMC	+5.0	+4.0	+3.0	+18.5
P-controller	+14.0	-9.0	-11.0	+34.0

Chapter 7

Conclusion and Future Work

7.1 Highlights of the Work

The ultimate goal of this research is to improve the path tracking of a TAGV. The vehicle is steered using skid steering where skidding and slipping between the tracks and the ground exists. This renders the system nonlinear and increases the difficulty of path control of the system. In order to design a controller for the TAGV, modeling the vehicle was carried out such that the nonlinearities are included. Lateral and longitudinal load transfer, skid steering dynamics, and tracks slip are included in this model. Furthermore, the model includes the effect of the vehicle actuators and the gear boxes. The simulation results show the effect of the slip on the vehicle behavior. A navigational system was used to drive the vehicle to the target pose autonomously. The navigational system uses a CCD camera to feedback the controller with the necessary information about the vehicle. The controller sends the required signal to the vehicle actuators to reduce the error between the given path and the output path of the vehicle. Since the motion of the TAGV is accomplished subject to different constraints, like the tracks-terrain interaction, a suitable path planning algorithm was applied to drive the vehicle to the final pose.

Due to the system nonlinearities, improving the path tracking of the TAGV requires designing a robust controller. Most of the control strategies used in the past are based on the kinematics of the vehicle. Very few of these deal with controlling the motion of a TAGV. Furthermore, most of the reported works on vehicle control and dynamics utilize linearized dynamic models for control purposes. However, for a TAGV navigating on terrain with different characteristics, the skid and slip result in unpredicted kinematics such that the control task is difficult to accomplish. Since SMCs are insensitive to system nonlinearities, disturbances and unmodeled terms, a SMC was used to control the path tracking function of the vehicle. The vehicle is powered by DC motors and hence two levels of the SMC were applied. The low level is used to control the vehicle DC motors and the high level is used to control the vehicle navigational system. A novel design methodology of SMCs was developed based on the system energy. This new methodology was tested on the vehicle DC motor model and was shown to result in a controller with very good performance. The performance of the SMC new design was compared to that of a proportional controller and was shown to be superior. To examine the robustness of the SMC to uncertainties in the DC motor model, the motor parameters were varied. The simulation results show that the SMC system is insensitive to such variations, unlike the case of the proportionally controlled system.

The DC motor is a SISO control system whereas the TAGV is a SIMO control system. This is a special case of MIMO control systems. Hence, extension of the new design methodology of the SMC was developed for SIMO control systems. The inverted pendulum system is a SIMO system similar to the TAGV, and was selected to exemplify and test the new approach. The ranges of the choice of the SMC new design parameters are unlimited such that more constraints had to be found and imposed. A sensitivity analysis of the system to parameter variation was used to find such constraints. Good results were obtained using this approach. Simulation results of the pendulum show very good performance of the SMC designed using the proposed approach. A comparison between the performance of the SMC and a proportional and a proportional-derivative controller was carried out. Results show the superiority of the SMC system.

The motor has a dissipative element to absorb energy whereas the pendulum is a pure inertial system. Hence, the control law of the proposed SMC design was improved upon by including dissipative components. Also, the independent sliding surfaces of the SMC were coupled together to create a hyper sliding surface. The simulation results of the improved SMC and of the SMC with a hyper surface were compared to the ones of the controllers used before.

The same SMC used for the pendulum system was applied to the TAGV. Since the controller was designed to be applied to a real tracked vehicle, the SMC was modified by introducing a thin boundary layer to the sliding surface to eliminate chattering. The TAGV is not a pure inertial system like the inverted pendulum system; hence, no dissipative components where introduced in the SMC law. However, the SMC with a hyper surface was introduced. The simulation results of the vehicle contain three comparisons for three different control laws. The first control law is a direct implementation of the proposed SMC design, the second is a proportional controller, and the third is the same SMC but with a hyper sliding surface. For different slips of the outer track, the proposed SMC effectively suppressed the system physical parameter variation. The simulation results of the three types of control laws prove that the SMC is generally superior and that the one with the hyper sliding surface is by far the best. The proposed SMCs are not complicated and are suitable for real time computer control.

7.2 Contributions

The major contribution of this research are summarized below:

1. A proof has been carried out to link the principle of work and energy of a system to the design of a SMC. The sliding mode controlled system was shown to have a faster response than a proportionally controlled one.

2. An energy based new design methodology for SMCs was developed. A relationship between the slope of the linear sliding surface and the controller gains was obtained for the first time in the literature. The design was tested on a DC motor model where good results were achieved. The SMC performance is better and more robust than that of proportional controllers, and PD-controllers where the gains were tuned using Ziegler-Nichols method of tuning and MATLAB Control System Toolbox.

3. An extended design of the SMC new design methodology was carried out for SIMO control systems. This design was examined on an inverted pendulum control system. Sensitivity analysis of the system to parameter variation was applied to impose more constraints to guide the choice of the controller parameters. A comparison between the performance of the proposed SMC, proportional controllers, and PD-controllers was carried out. The PD-controllers were tuned using Ziegler-Nichols method and MATLAB Control System Toolbox.

4. The inverted pendulum system is a pure inertial system without any dissipative elements. Improvement was made to the SMC to include damping components in its definition. The ranges of the controller parameters are guided by employing a sensitivity analysis of the system.

5. The structure of the TAGV control system is similar to that of the inverted pendulum control system since both are SIMO control systems. Hence, the extended design of the SMC was applied to the vehicle. Sensitivity analysis was also carried out in the TAGV system case to determine the controller parameters range. A comparison has been made between the performance of the SMC and the proportional controller.

7.3 Future Work

The work of this dissertation can be extended in different directions. A few important proposals and recommendations for future work are as follows:

1. The translational velocity of the TAGV was selected to be fixed. Designing a SMC for trajectory tracking with varying the translational velocity of the TAGV can be carried out for future work.

2. The sliding surface of the SMC was chosen to be linear in this work. A study of the efficiency of nonlinear sliding surfaces should be carried out.

3. The sign switching function of the SMC was exchanged with a saturation switching function in order to eliminate chattering. This function employs the boundary layer technique. Other techniques to deal with chattering exist and should be investigated.

4. In order to assess the performance of the proposed controller, experimental verification should be carried out.

5. The total time delay due to the camera and image analysis was assumed to be 0.5 second. This delay reflects negatively on the performance of the controller. The extent of the effect of time delay on the performance, and a quantification of that effect is of practical importance and should be studied.

6. The proposed control law design methodology of this work can be used for other applications. It would be interesting and valuable to comparatively evaluate the results of this design approach to other approaches of controllers in other applications.

References

[1] J.L. Martinez, A. Mandow, J. Morales, S. Pedraza, A. Gracia-Cerezo, "Approximating Kinematics for Tracked Mobile Robots", The international Journal of Robotics Research, Vol. 24, pp. 867-878, 2005.

[2] J. Y. Wong, "Theory of Ground Vehicles", 3rd Edition, John Wiley & Sons Inc., New York, 2001.

[3] A. T. Le, D. Rye, H. Whyte, "Estimation of Track-Soil Interactions for Autonomous Tracked Vehicle", IEEE International Conference on Robotics and Automation, Vol.2, pp. 1388-1393, 1997.

[4] G. Ferretti, R. Girelli, "Modeling and Simulation of an Agricultural Tracked Vehicle", Journal of Terramechanics, Vol. 36, pp 139-158, 1999.

[5] Th. Fraichard, R. Mermond, "Path Planning with Uncertainty for Car-Like Robots" , IEEE International Conference on Robotics and Automation, Vol.1, pp. 27-32, 1998.

[6] A. Razavian, J. Sun, "Cognitive Based Adaptive Path Planning Algorithm for Autonomous Robotic Vehicles", Proceedings of the IEEE Southeastern Conference, pp. 153-160, 2005.

[7] R. Siegwart, I. R. Nourthbakhash, "Introduction to Autonomous Mobile Robots", The MIT Press, Massachusetts, 2004.

[8] C. Louste, A. Liegeois, "Path Planning for Non-Holonomic Vehicles: A Potential Viscous Fluid Method", Robotica, Vol.20, pp.291-298, 2002.

[9] Y. Wang, "Nonholonomic Motion Planning: A Polynomial Fitting Approach", IEEE International Conference on Robotics and Automation, Vol.4, pp. 2956-2961, 1996.

[10] P. Saeedi, P. D. Lawrence, "An Autonomous Excavator with Vision-Based Track-Slippage Control", IEEE Transactions on Control Systems Technology, Vol. 13, Issue 1, pp. 67-84, 2005.

[11] M. Ahmadi, V. Polotski, R. Hurteau, "Path Tracking Control of Tracked Vehicles", IEEE Transactions on Robotics and Automation, Vol. 3, pp. 2938-2943, 2000.

[12] G. G. Wang, S. H. Wang, C. W. Chen, "Design of Turning Control for a Tracked Vehicle", IEEE Control Systems Magazine, Vol. 10, Issue 3, pp. 122-125, 1990.

[13] Z. Fan, Y. Koren, D. Wehe, "Tracked Mobile Robot Control: Hybrid Approach", Journal of Control Engineering Practice, Vol. 3, Issue 3, pp. 329-336, 1995.

[14] J. Yang and J. Kim, "Sliding Mode Control for Trajectory Tracking of Nonholonomic Wheeled Mobile Robots", IEEE Transactions on Robotics and Automation, Vol. 15, Issue 3, pp. 578-587, 1999.

[15] Yu-Fing Li, "High Precision Motion Control Based on Discrete-Time Sliding Mode Approach", Doctoral Thesis, Royal Institute of Technology, Stockholm, Sweden, 2001.

[16] V. Utkin, " Variable Structures Systems with Sliding modes", IEEE Transactions on Automatic Control, Vol. 22, Issue 2, pp. 212-222, 1977.

[17] J. Slotine, W. Li, " Applied Nonlinear Control", Prentice Hall Englewood Cliffs, New Jersey, 1992.

[18] J. Y. Hung, W. Gao, J. C. Hung, " Variable Structure Control: A Survey", IEEE Transactions on Industrial Electronics, Vol. 60, Issue 1, pp. 2-22, 1993.

[19] Y. Pan, S. Suzuki, S. Hatakeyama, "Design of Variable Structure Controller", IEEE Proceedings of the 39th Conference on Decision and Control, 2000.

[20] J. Ackermann, V. Utkin, "Sliding Mode Control Design Based on Ackermann's Formula", IEEE Transactions on Automatic Control, Vol. 43, Issue 2, pp. 234-237, Feb. 1998.

[21] K. Young, V. Utkin, U. Ozguner, "A Control Engineer's Guide to Sliding Mode Control", IEEE Transactions on Control Systems Technology, Vol. 7, Issue 3, pp. 328-342, 1999.

[22] R. Decarlo, S. Zak, G. Matthews, " Variable Structure Control of Nonlinear Multivariable Systems: A Tutorial", Proceedings of the IEEE, Vol. 67, Issue 3, pp. 212-232, 1988.

[23] J. Wang, A. B. Rad, P. T. Chan, "Indirect Adaptive Fuzzy Sliding Mode Control: Part I: Fuzzy Switching", Journal of Fuzzy Sets and Systems, Vol. 122, Issue 1, pp.21-30, 2001.

[24] S. Lin, Y. Chen, "Design of Self-Learning Fuzzy Sliding Mode Controllers Based on Genetic Algorithm", Journal of Fuzzy Sets and Systems, Vol. 86, pp.139-153, 1997.

[25] M. Ghalia, A. Alouani, "Knowledge-Based Robust Control of Complex Systems", IEEE International Conference on Intelligent Systems of the 21st Century, Vol. 2, pp. 977-982, 1995.

[26] K. Jezernik, M. Rodic, R. Safaric, B. Curk, "Neural Network Sliding Mode Robot Control", Robotica, Vol. 15, pp. 23-30, 1997.

[27] V. Utkin, J. Guldner, J. Shi, "Sliding Mode Control in Electromechanical Systems", Taylor & Francis Inc., Philadelphia, 1999.

[28] N. Sadati, A. Talasaz, "Chattering-Free Adaptive Fuzzy Sliding Mode Control", IEEE International Conference on Cybernetics and Intelligent Systems, Vol. 1, pp. 29-34, 2004.

[29] M. Chen, Y. Hwang, M. Tomizuka, "Sliding Mode Control Reduced Chattering for Systems with Dependant Uncertainties", IEEE International Conference on Network, Sensing and Control, Vol. 2, pp. 967-971, 2004.

[30] L. Iannelli, K. Johansson, U. Jonsson, F. Vasca, "Dither Shape in the Averaging of Switched Systems", IEEE Proceedings of the American Control Conference, Vol. 6, pp. 5812-5817, 2004.

[31] E. Doskoscz, Y. Shtessel, "MIMO Sliding Mode Control of a Robotic 'Pick and Place' System Modeled as an Inverted Pendulum on a Moving Cart", IEEE Proceedings of the Southeastern Symposium on System Theory, 1998.

[32] R. C. Drof, "Modern Control Systems", 5th Edition, Addison-Wesley, New York, 1989.

[33] K. Ogata, "Modern Control Engineering", 2nd Edition, Prince Hall, New Jersey, 1990.

[34] D. G. Roussel, "Vision-Based Navigation and Control of a Robotic Vehicle", Master of Applied Science Thesis, University of Ottawa, Ottawa, Canada, 2006.

[35] A. Agarwal, C. V. Jawhar, P. J. Narayanan, "A survey of Planar Homography Estimation Techniques", Technical Report, Center of Visual Information Technology, International Institute of Information Technology, Hyderabad, 500019, India, 2005.

Appendix A

DC Motor Model

A.1 Introduction

The motive power for the tracked autonomous guided vehicle under consideration is provided by DC motors. DC motor are often used in control systems because of their control ability and attributes. In the following sub-section the DC motor model will be derived in details.

A.2 Theoretical Aspects of the DC Motor

The DC motor has both electrical and mechanical constrains as explained by Ogata [33]. Figure A.1 is a schematic diagram showing both the electrical circuit components and a typical mechanical system driven by a DC motor. The figure shows how the rotating part of the motor is connected to the output shaft that couples it to the mechanical load through a gear ratio.

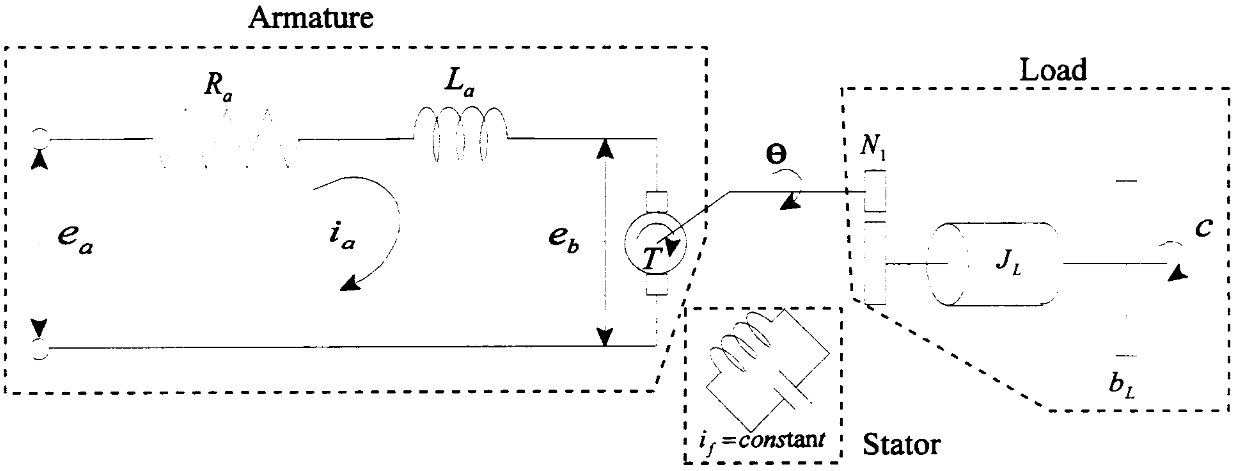

Figure A.1: Armature-controlled DC motor

With reference to Figure A.1, the differential equation that describes the dynamics of the armature circuit EMF is given by:

$$L_a \frac{di_a}{dt} + R_a i_a + K_b \frac{d\theta}{dt} = e_a \tag{A.1}$$

where, R_a and L_a are the armature resistance and inductance respectively, i_a and e_a are the armature current and voltage respectively, and K_b is the back EMF

The third term in the left hand side of Equation A.1 is a back EMF induced in the armature and is proportional to the motor angular velocity. This induced voltage opposes and reduces the supply voltage as can be seen in Figure A.1.

For a DC motor with constant armature current, the torque *T* developed by the motor is directly proportional to the armature current i_a and is given by:

$$T = K_T i_a \tag{A.2}$$

where K_T is the motor torque constant. It should be noted that in the SI unit system $K_b = K_T$.

The load on the motor is assumed here to be inertia and viscous. The equivalent moment of inertia *J* and equivalent viscous friction coefficient *b* of the motor and load together referred to the motor shaft are given respectively by:

$$\begin{aligned} J &= J_m + n^2 J_L \\ b &= b_m + n^2 b_L \end{aligned} \tag{A.3}$$

where J_m and b_m the motor moment of inertia and viscous friction coefficient, J_L and b_L are the external load moment of inertia and viscous friction, and *n* is the gear box ratio N_1 / N_2

Hence, the dynamic equation of the motor load system is given by:

$$\begin{aligned} J\frac{d^2\theta}{dt^2} + b\frac{d\theta}{dt} &= T \\ &= K_T i_a \end{aligned} \tag{A.4}$$

Usually, the value of the armature inductance is very small in comparison to its resistance and can be ignored. Hence, Equation A.1 reduces to the following:

$$R_a i_a + K_b \frac{d\theta}{dt} = e_a \tag{A.5}$$

Substituting Equation A.2 into Equation A.5 for i_a and rearranging gives:

$$\dot{\theta} = \frac{1}{K_b} e_a - \frac{R_a}{K_b K_T} T \tag{A.6}$$

Appendix B

Sliding Mode Controller Design

B.1 Introduction

Usually the design of SMC consists of two steps: defining the sliding surface, and defining the switching feedback control law. The sliding surface is usually of a lower order than the given system model and must be designed such that the system behavior during sliding satisfies the design objectives in terms of stability and performance. The switching feedback control law is designed such that it satisfies the reaching condition and thus drives the system state trajectory to the sliding surface and maintains it thereafter. The main SMC design methods are reviewed briefly in the following sections.

B.2 Sliding Surface Design

The sliding surface can be either linear or nonlinear. For simplicity, this thesis focuses only on linear sliding surfaces. Moreover, it is sufficient to consider only systems without uncertainties and disturbances for surface design. Some common methods for defining the differential equation of sliding mode are summarized below.

Consider the following system;

$$\dot{X} = A(X) + B(X)u \tag{B.1}$$

with a sliding surface given by:

$$s(X) = 0 \tag{B.2}$$

where $A(X)$ and $B(X)$ are general nonlinear functions of the state vector X, and $X \in R^n$, $u \in R^m$.

1. ***Equivalent control approach*** [22]

The equivalent control is found by recognizing that $\dot{s}(X) = 0$ is a necessary condition for the system state trajectory to stay on the sliding surface $s(X) = 0$. Therefore, setting $\dot{s}(X) = 0$ results in the following relationship:

$$\begin{aligned} \dot{s}(X) &= \left(\frac{\partial s}{\partial X}\right)\dot{X} \\ &= 0 \end{aligned} \tag{B.3}$$

by substituting for $\dot{X}$ from Equation B.1 into Equation B.3 gives:

$$\begin{aligned} \dot{s}(X) &= \frac{\partial s}{\partial X}A(X) + \frac{\partial s}{\partial X}B(X)u_{eq} \\ &= 0 \end{aligned} \tag{B.4}$$

where u_{eq} is the equivalent control function. The equivalent control function, u_{eq}, can be factored out from Equation B.4 and is given by:

$$u_{eq} = -\left(\frac{\partial s}{\partial X}B(X)\right)^{-1}\frac{\partial s}{\partial X}A(X) \tag{B.5}$$

where $\frac{\partial s}{\partial X}B(X)$ is nonsingular.

Substituting Equation B.5 into Equation B.1, the dynamics of the system on the switching surface is governed by:

$$\dot{X} = \left(I - B(X)\left(\frac{\partial s}{\partial X}B(X)\right)^{-1}\frac{\partial s}{\partial X}\right)A(X) \tag{B.6}$$

If the system given by Equation B.1 is linear, time invariant and described by:

$$\dot{X} = AX + Bu \tag{B.7}$$

where A and B are properly dimensioned constant matrices, the switching surface can be defined as:

$$\begin{aligned} s(X) &= \Lambda X(t) \\ &= 0 \end{aligned} \tag{B.8}$$

where $\Lambda = [\lambda_1 \dots, \lambda_m]^T$ is a $m \times n$ matrix and $\frac{\partial s}{\partial X} = \Lambda$.

Then, the equivalent control law of Equation B.5 can be rewritten as:

$$u_{eq} = -(\Lambda B)^{-1} \Lambda A X \tag{B.9}$$

and Equation B.6 becomes:

$$\begin{aligned} \dot{X} &= (I - B(\Lambda B)^{-1} \Lambda) A X \\ &= (A - BK) X \end{aligned} \tag{B.10}$$

where $K = (\Lambda B)^{-1} \Lambda A$.

Equation B.10 describes the behavior of the system given by Equation B.7 in the sliding mode. For linear systems, the desired system performance can be achieved by a suitable choice of the matrix K. The elements of K can be found by applying one of the classical control feedback design methods, such as the pole placement or linear quadratic approaches.

2. *Canonic form approach* [16]

For a linear time invariant single input system, if the system model can be transformed to the following controllable canonic form:

$$\begin{aligned} \dot{x}_i &= x_{i+1}, \quad i = 1, \dots\dots, n-1 \\ \dot{x}_n &= \sum_{i=1}^{n} -a_i x_i + bu \end{aligned} \tag{B.11}$$

then, a sliding surface can be defined by:

$$\begin{aligned} s(X) &= \lambda_1 x_1 + \lambda_2 x_2 + \lambda_3 x_3 + \dots + x_n \\ &= 0 \end{aligned} \tag{B.12}$$

By solving Equation B.12 for x_n and then substituting the result in Equation B.11, the differential equation of the sliding mode is found to be:

$$\dot{x}_{n-1} = -\lambda_1 x_1 - \lambda_2 x_2 - \dots - \lambda_{n-1} x_{n-1} \tag{B.13}$$

The coefficients of the switching surface in Equation B.12 define the desired characteristics of the sliding mode if the system model is described in canonic form, i.e., the characteristics of the closed loop system after the reaching phase. These coefficients can be chosen by applying one of the classical control feedback design methods.

3. Coordinate transformation approach [18]

Consider the system given by Equation B.7 Suppose that the system model can be transformed to the following nonsingular transformation:

$$\begin{aligned} \dot{X}_1 &= A_{11} X_1 + A_{12} X_2 \\ \dot{X}_2 &= A_{21} X_1 + A_{22} X_2 + B_2 u \end{aligned} \tag{B.14}$$

where B_2 is nonsingular $m \times m$ matrix and $X_1 \in R^{n-m}$, $X_2 \in R^m$.

And the switching surface is given by:

$$\begin{aligned} s(X) &= \Lambda_1 X_1 + \Lambda_2 X_2 \\ &= 0 \end{aligned} \tag{B.15}$$

From Equation B.15, X_2 is related linearly to X_1 and hence the following equation is valid:

$$\begin{aligned} \dot{X}_1 &= A_{11} X_1 + A_{12} X_2 \\ X_2 &= -K X_1 \end{aligned} \tag{B.16}$$

where $K = \Lambda_2^{-1}\Lambda_1$ and Λ_2 is nonsingular.

Equation B.16 represents *n-m* order system in which X_2 can be considered as the control input to the system. Hence, the dynamics behavior of the sliding mode can be determined by:

$$\dot{X}_1 = (A_{11} - A_{12}K)X_1 \tag{B.17}$$

The design of an appropriate sliding surface can be achieved by using one of the classical control feedback design methods to compute *K* such that $A_{11} - A_{12}K$ has the desired characteristics. Once *K* is found, the desired switching surface can be designed as:

$$\begin{aligned} s(X) &= \Lambda X \\ &= \Lambda_2[K, I]X \end{aligned} \tag{B.18}$$

where Λ_2 is arbitrarily selected. A simple selection is to let $\Lambda_2 = I$.

B.3 Control Law Design

Once the sliding surface is obtained, attention must be turned to design the switching feedback control law. Designing the control law also entails solving the reachability problem. This involves the selection of a feedback control function *u* which can drive the state vector *x* towards the sliding surface and maintain it on the surface. The condition under which the state will move towards and reach a sliding surface is called the reaching condition.

The first step of designing the sliding mode control law is defining a suitable reaching condition which is used to find the control law parameters. Then a suitable control law has to be defined. According to Hung et al [18] and DeCarlo et al [22], the control law could be prespecified. The following approaches were proposed where the control law is prespecified:

1. ***Relay control approach*** [15, 18, 22]

The classic sufficient condition for a sliding mode to ensue involves satisfying the following reaching condition:

$$s_i \dot{s}_i < 0, \quad i = 1, \ldots, m \tag{B.19}$$

This reaching condition can be considered as a special case of the time derivative of the following Lyapunov function candidate:

$$V(X,t) = s^T s \tag{B.20}$$

Hence, the reaching condition is given by:

$$\dot{V}(X,t) < 0 \tag{B.21}$$

Substituting Equation B.20 into Equation B.21 results in:

$$\begin{aligned} \dot{V}(X,t) &= \frac{d}{dt}(s^T s) \\ &= 2s^T \dot{s} < 0 \end{aligned} \tag{B.22}$$

Finite reaching time is guaranteed if Equation B.21 is modified to be:

$$\dot{V}(X,t) < -\varepsilon \tag{B.23}$$

where ε is strictly positive.

The variable structure control for each element of the control vector u might take the form of a relay switching as follows:

$$u_i(X) = \begin{cases} +k_i, & s_i(X) > 0 \\ -k_i, & s_i(X) < 0, \quad i = 1, \ldots, m \end{cases} \tag{B.24}$$

where the values of $+k_i$ and $-k_i$ are chosen to satisfy the desired reaching condition.

The relay gain might be either fixed or state dependent. Consider the linear time invariant system given by Equation B.7 as an example and the reaching condition given by Equation B.19, the relay gain can be found by satisfying the following condition:

$$s_i \frac{\partial s_i}{\partial X} \frac{\partial X}{\partial t} < 0 \tag{B.25}$$

Substituting Equation B.7 into Equation B.25 results in:

$$s_i \frac{\partial s_i}{\partial X}(AX + Bk_i) < 0 \tag{B.26}$$

2. ***Linear feedback with switched gains approach*** [15, 18, 22]

Here, the control law structure is given by:

$$u(X) = \psi X \tag{B.27}$$

where $\psi = [\psi_{ij}(X)]$ is a $m \times n$ matrix of state-dependent gains.

A popular structure of the gains is given as follows:

$$\psi_{ij}(X) = \begin{cases} \alpha_{ij}, & s_i(X)x_j > 0 \\ \beta_{ij}, & s_i(X)x_j < 0\ , \quad for \begin{cases} i = 1, \ldots m \\ j = 1, \ldots n. \end{cases} \end{cases} \tag{B.28}$$

where the parameters α_{ij} and β_{ij} are chosen to satisfy the following reaching condition:

$$s_i(\psi_{i1}x_1 + \psi_{i2}x_2 + \ldots.. + \psi_{in}x_n) < 0 \tag{B.29}$$

3. ***Augmentation of the equivalent control law approach*** [15, 18, 22]

Recall that the equivalent control law u_{eq} can be computed as shown in Equation B.5. Using u_{eq} alone can not drive the system state towards the sliding surface if the initial conditions of the system are far away from the sliding surface. One popular design approach involves augmenting u_{eq} with another component such that the control law takes the following form:

$$u = u_{eq} + \Delta u \tag{B.30}$$

where Δu is added to satisfy the reaching condition. A common form of Δu is that of a switching relay.

Y. Li [15] Hung et al [18] and DeCarlo et al [22] proposed the control hierarchy method to design the control law where the law is not prespecified as in the above mentioned methods. The hierarchical control method uses the classical sufficient reaching condition mentioned earlier (Equation B.19). This method aims to establish a control scheme such that the sliding modes takes place in a preassigned order, i.e., the system state starts from the initial condition x_o, moves progressively onto a lower dimensional switching surfaces, and eventually reaches the final sliding surface s_E according to the following scheme:

$$x_o \rightarrow s_1 \rightarrow (s_1 \cap s_2) \rightarrow (s_1 \cap s_2 \cap s_3) \rightarrow \ldots \rightarrow s_E \tag{B.31}$$

The determination of the control law involves the solution of a set of complicated inequalities. For the system given by Equation B.7, the control law *u* is determined from the solution of the following *m* pairs of inequalities given by:

$$\begin{aligned} \dot{s}_i &= \frac{\partial s_i}{\partial X}(AX + Bu) \\ &= \begin{cases} > 0, & s_i < 0 \\ < 0, & s_i > 0 \end{cases}, \quad i = 1, \ldots, m. \end{aligned} \tag{B.32}$$

Solving Equation B.32 is a difficult task. Consequently, this approach is primarily of theoretical value and is seldom used in practice.

Appendix C

Inverted Pendulum Model

With reference to Figure 5.1, x_G and y_G are the coordinates of the center of gravity of the mass *m*. Applying Newton's second law to the *x* direction of motion of the system results in:

$$M\frac{d^2x}{dt^2} + m\frac{d^2x_G}{dt^2} = u \tag{C.1}$$

With reference to the figure, substituting for x_G by $x + l\sin\theta$ gives:

$$M\frac{d^2x}{dt^2} + m\frac{d^2}{dt^2}(x + l\sin\theta) = u \tag{C.2}$$

noting that

$$\begin{aligned} \frac{d^2}{dt^2}\sin\theta &= -(\sin\theta)\dot{\theta}^2 + (\cos\theta)\ddot{\theta} \\ \frac{d^2}{dt^2}\cos\theta &= -(\cos\theta)\dot{\theta}^2 - (\sin\theta)\ddot{\theta} \end{aligned} \tag{C.3}$$

Hence, Equation C.2 can be rewritten as follows:

$$(M + m)\ddot{x} - ml(\sin\theta)\dot{\theta}^2 + ml(\cos\theta)\ddot{\theta} = u \tag{C.4}$$

The motion in the *y* direction provides no significant information about the dynamics of the system. Applying Newton's second law to the rotational motion of the mass *m* around point *P* results in the following:

$$m\frac{d^2x_G}{dt^2}l\cos\theta - m\frac{d^2y_G}{dt^2}l\sin\theta = mgl\sin\theta \tag{C.5}$$

With reference to the figure, substituting for x_G and y_G in Equation C.5 gives:

$$\left[m\frac{d^2}{dt^2}(x + l\sin\theta)\right]l\cos\theta - \left[m\frac{d^2}{dt^2}(l\cos\theta)\right]l\sin\theta = mgl\sin\theta \tag{C.6}$$

Substituting from Equation C.3 into Equation C.6 and simplifying, yields:

$$m\ddot{x}\cos\theta + ml\ddot{\theta} = mg\sin\theta \tag{C.7}$$

Both Equations C.4 and C.7 are nonlinear. Since it is required to keep the pendulum upright, $\theta(t)$ and $\dot{\theta}(t)$ can be assumed small quantities such that $\sin\theta \approx \theta$, $\cos\theta \approx 1$, and $\theta\dot{\theta}^2 \approx 0$. Then Equations C.4 and C.7 can be linearized as follows:

$$(M + m)\ddot{x} + ml\ddot{\theta} = u \tag{C.8}$$

$$m\ddot{x} + ml\ddot{\theta} = mg\theta \tag{C.9}$$

Subtracting Equation C.9 from Equation C.8 gives:

$$M\ddot{x} + mg\theta = u \tag{C.10}$$

Solving Equations C.8 and C.10 simultaneously to eliminate $\ddot{x}$ results in the following:

$$Ml\ddot{\theta} - (M + m)g\theta = -u \tag{C.11}$$

Equations C.10 and C.11 represents the system dynamics.